Development of Multisensing Imaging Probes Using Carbon Dots

Jun-Ray Macairan

A Thesis
In the Department
of
Chemistry and Biochemistry

Presented in Partial Fulfillment of the Requirements
for the Degree of Doctor of Philosophy (Chemistry) at
Concordia University
Montréal, Québec, Canada

February 2021

CONCORDIA UNIVERSITY

School of Graduate Studies

This is to certify that the thesis prepared

By: Jun-Ray Macairan

Entitled: Development of Multisensing Imaging Probes Using Carbon Dots

and submitted in partial fulfillment of the requirements for the degree of

Doctor of Philosophy (Chemistry)

complies with the regulations of the University and meets the accepted standards with respect to originality and quality.

Signed by the final examining committee:

_____ Chair
Dr. Patrick Gulick

_____ External Examiner
Dr. Mohamed Siaj

_____ External to Program
Dr. David Kwan

_____ Examiner
Dr. Louis Cuccia

_____ Examiner
Dr. John Oh

_____ Supervisor
Dr. Rafik Naccache

Approved by _____
Dr. Yves Gélinas, Graduate Program Director

_____
Pascale Sicotte, Dean of Faculty

Date: Friday April 23, 2021

ABSTRACT

Development of Multisensing Imaging Probes Using Carbon Dots

Jun-Ray Macairan, Ph. D.

Concordia University, 2021

Imaging probes serve as unique diagnostic tools in biomedical applications offering high sensitivity particularly in their ability to image cells and tissues. These tools are crucial for early detection and disease diagnostics especially with an increase in numbers of an aging population and the requirement for more efficient health care. Recent advancements in the field of nanomaterials have propelled research groups into investigating these nanoparticles for various biological applications including drug delivery, biosensing and bioimaging, among others. Recently, carbon dots have garnered significant attention because they can be prepared from simple synthetic routes using inexpensive precursors, offering tunable optical properties, low cytotoxicity and good biocompatibility. Their inherent fluorescent nature not only allows for fluorescence imaging, but also for sensing environmental changes, which can provide additional insights for the development of novel diagnostic applications.

Herein, carbon dots are synthesized using a one-step microwave- and solvothermal-assisted reaction. The prepared dots fluoresce simultaneously in both the blue and the red regions of the electromagnetic spectrum. The dots' physico-optical properties are thoroughly studied to shed light on their fluorescence mechanism, which remains of topic of debate in the literature. It is demonstrated that the fluorescence of the nanoparticles is tailored through manipulation of key synthesis parameters to determine the underlying effect on the observed optical signature. The dots' unique optical properties are believed to derive from the carbon core- and molecular-states fluorescence mechanism. In brief, the blue fluorescence stems from the core, while the red counterpart originates from the molecular states that are typically localized on the surface of the dot.

With their unique fluorescence properties and our understanding of this phenomenon, these dots offer the possibility of sensing changes in temperature and pH, using ratiometric approaches. Both

temperature- and pH-sensing measurements translate well from the cuvette to the cellular model. The change in physiological parameters are in agreement with the change in emission using epifluorescence and confocal microscopy. The ability to glean such information renders these nanoparticles into versatile diagnostic nanotools with the ability to shed new insights on disease mechanisms and can be foreseen as future tools for *in vivo* sensing applications.

ACKNOWLEDGEMENTS

Dr. Naccache, I couldn't have asked for a better supervisor. I didn't know what I was getting into at first. I'm glad it turned out the way it did because I got to work with a fantastic supervisor and great person. Your guidance and your dedication to help your students are deserving of all the fancy meat cuts out there. You make research fun. You take your time with your students. You helped me become the scientist that I am today. In addition to reminding me where the lab is located every other day, you inspire me to achieve greatness. To make you proud, one of these days, the student will surpass the master. Maybe not now. So, watch your back, there will be a new Dr. Nano in town. "WBTY?" Well… it's still you – for now. I'll settle for being the better guitarist.

I would like to thank my committee members, Dr. John Oh and Dr. Louis Cuccia for their continuous guidance throughout my degree. I am glad I had opportunity to work in Dr. Oh's lab during my undergrad. Had he not given me that chance, I probably wouldn't be writing this thesis. Dr. Cuccia has always been very supportive. You always had kind things to say, which helped boost morale. Alumni can still have a sip of coffee at Café Cuccia, yes?

To Dr. John Manioudakis, I am forever in your debt. You have helped me become a stronger person and a better scientist with your guidance and friendship. I'll never forget our lunchtimes and your smoke breaks – that's when true wisdom is bestowed by you. To Peter Liu, you stuck by me for my whole degree. You are an excellent scientist always willing to help in times of need and you are an even better friend.

To my other friends, thank you for keeping me sane. I can always count on you guys to keep me going even when times are rough. Thank you for giving me lifts when I didn't have a car. Thank you for being my cheerleaders.

To my parents and to my Ate Jen, you have helped me grow and provided me with everything so that I can become the man I am today. Your unconditional love and support make me very fortunate. I am blessed to have such parents and sister who helped pave the way for my successes in life. I have and I will always look up to you. As I look back, I realize how much you have all sacrificed for me and how much you have done for me to make my life less stressful. I'll never

take any of that for granted. Our family times were much needed throughout this whole degree. I love you all so much. I only wish to make you proud. This is for you.

To FN, this acknowledgement wouldn't be complete without including my whole family. You're part of my family now. Your friendship, your love and your support have had some of the biggest impacts in my life – let alone my grad studies. Our inside jokes and our morning small talks always brighten up my day. I am so glad to have you in my life. I'll always be there for you. RayJay and $oule$$. Ride or Die.

Contribution of Authors

Manuscripts (Included in the Thesis)

Manuscript 1 – Elucidating the Mechanism of Dual-Fluorescence in Carbon Dots

(Ref: Macairan, J.-R.; de Medeiros, T.; Gazzetto, M.; Yarur, F.; Cannizzo, A.; Naccache, R., Elucidating the Mechanism of Dual-Fluorescence in Carbon Dots. *Submitted*)

Jun-Ray Macairan: The author prepared and purified the different CDs *via* solvothermal-mediated reaction. Comprehensive characterization efforts were carried out following modification to each reaction condition in order to assess its impact on the properties of the CDs: (i) TEM for size and morphology, (ii) XRD for crystallinity and phase, (iii) Raman spectroscopy to verify the order/disorder states in the structure dots, (vi) zeta potential measurements to evaluate its colloidal stability, (v) FT-IR and XPS spectroscopies to study surface composition and (vi) UV-Vis absorption and fluorescence spectroscopies to glean information regarding their steady-state optical properties. Although some experiments were carried out by the collaborators (i.e. electrochemical and transient absorption spectroscopy studies), the author was involved in the analyses of the data. The author wrote the majority of the manuscript.

Tayline de Medeiros: Carried out the characterization of physical properties

Michela Gazzetto: Performed transient absorption spectroscopy experiments

Francisco Yarur: Performed electrochemical experiments

Andrea Cannizzo: Research supervision, manuscript writing and editing

Rafik Naccache: Research supervision, manuscript writing and editing

Manuscript 2 – Intracellular Ratiometric Temperature Sensing Using Fluorescent Carbon Dots

(Ref: Macairan, J.-R.; Jaunky, D. B.; Piekny, A.; Naccache, R., Intracellular ratiometric temperature sensing using fluorescent carbon dots. *Nanoscale Advances* **2019,** *1* (1), 105-113)

Jun-Ray Macairan: The author prepared and purified the CDs *via* microwave-mediated reaction. The author characterized the material using (i) TEM, (ii) FTIR, (iii) XPS, (iv) UV-Vis and

fluorescence spectroscopy. The author studied the effects of temperature on the fluorescence signature of the dots in a cuvette model. The author also carried out in vitro viability and localization experiments upon receiving training on cell work. This was then followed by intracellular temperature sensing experiments. The author wrote most of the manuscript.

Dilan Jaunky: Provided cell work training and performed preliminary cell work data acquisition, manuscript writing

Alisa Piekny: Research supervision, manuscript writing and editing

Rafik Naccache: Research supervision, manuscript writing and editing

Manuscript 3 – Ratiometric pH Sensing in Living Cells Using Carbon Dots

(Ref: Macairan, J.-R.; Zhang, I.; Clermont-Paquette, A.; Naccache, R.; Maysinger, D., Ratiometric pH Sensing in Living Cells Using Carbon Dots. *Part. Part. Syst. Charact.* **2020,** *37* (1), 1900430)

Jun-Ray Macairan: The author prepared and purified the CDs *via* microwave-mediated reaction. The author characterized the material using (i) TEM, (ii) FTIR, (iii) XPS, (iv) UV-Vis and fluorescence spectroscopy. The author also carried out pH experiments in a cuvette model and analysed the cell work data gathered by the collaborators. The author co-wrote most of the manuscript.

Issan Zhang: Led cell work experiments (viability and imaging), manuscript writing

Adryanne Clermont-Paquette: Carried out initial pH studies in cuvette model

Dusica Maysinger: Research supervision, manuscript writing and editing

Rafik Naccache: Research supervision, manuscript writing and editing

Additional Manuscripts (Not Included in the Thesis)

Manuscript 4 – Effects of Polydopamine-Passivation on the Optical Properties of Carbon Dots and its Potential use in vivo

(**Ref:** Pappalardo, J. S.; Macairan, J.-R.; Macina, A.; Poulhazan, A.; Quattrocchi, V.; Marcotte, I.; Naccache, R., Effects of polydopamine-passivation on the optical properties of carbon dots and its potential use in vivo. *Phys. Chem. Chem. Phys.* **2020,** *22* (29), 16595-16605)

Jun-Ray Macairan: The author prepared and purified the CDs *via* microwave-mediated reaction. The author characterized the material using (i) TEM, (ii) FTIR, (iii) XPS, (iv) UV-Vis and fluorescence spectroscopy. The author co-wrote most of the manuscript.
Sebastian Pappalardo: Executed *in vitro* and *in vivo* experiments
Alexia Macina: Carried out additional synthesis and characterization of the contr
Alexandre Poulhazan: Performed ^{1}H NMR studies
Valeria Quattrochi: Assisted with *in vitro* and *in vivo* experiments
Isabelle Marcotte: Research supervision, manuscript writing and editing
Rafik Naccache: Research supervision, manuscript writing and editing

Manuscript 5 – Ratiometric Detection of Heavy Metal Ions Using Fluorescent Carbon Dots

(**Ref:** Yarur, F.; Macairan, J.-R.; Naccache, R., Ratiometric detection of heavy metal ions using fluorescent carbon dots. *Environ. Sci.: Nano* **2019,** *6* (4), 1121-1130)

Francisco Yarur: Performed metal detection experiments with CDs using fluorescence and UV-Vis absorbance spectroscopy; wrote most of the manuscript
Jun-Ray Macairan: The author prepared and purified the CDs *via* microwave-mediated reaction. The author characterized the material using (i) TEM, (ii) FTIR, (iii) XPS, (iv) UV-Vis and fluorescence spectroscopy. The author contributed in the writing of the manuscript.
Rafik Naccache: Research supervision, manuscript writing and editing

Manuscript 6 – Microwave-Assisted Synthesis of Carbon Dots and Their Applications

(**Ref:** de Medeiros, T. V.; Manioudakis, J.; Noun, F.; Macairan, J.-R.; Victoria, F.; Naccache, R., Microwave-assisted synthesis of carbon dots and their applications. *J. Mater. Chem. C* **2019,** *7* (24), 7175-7195)

Tayline de Medeiros: Manuscript writing and formatting
John Manioudakis: Manuscript writing
Farah Noun: Manuscript writing
Jun-Ray Macairan: Manuscript writing
Florence Victoria: Manuscript writing
Rafik Naccache: Research supervision, manuscript writing and editing

Manuscript 7 – Facile Aqueous-Phase Synthesis of an Ultrasmall Bismuth Nanocatalyst for the Reduction of 4-Nitrophenol

(**Ref:** Liang, Y.; Manioudakis, J.; Macairan, J.-R.; Askari, M. S.; Forgione, P.; Naccache, R., Facile Aqueous-Phase Synthesis of an Ultrasmall Bismuth Nanocatalyst for the Reduction of 4-Nitrophenol. *ACS Omega* **2019,** *4* (12), 14955-14961)

Yanjie Liang: Synthesis and the characterization of the NPs; initiate catalysis experiment; manuscript writing
John Manioudakis: Carried out the synthesis and the characterization of the NPs
Jun-Ray Macairan: The author characterized the NPs (TEM, SEM and FTIR) and studied the catalytic efficiency of the NPs; manuscript writing
Mohammad S. Askari: Synthesis and characterization; manuscript writing
Pat Forgione: Research supervision, manuscript writing and editing
Rafik Naccache: Research supervision, manuscript writing and editing

Table of Contents

List of Figures

List of Supplementary Figures

List of Abbreviations

CDs	Carbon Dots
DMEM	Dulbecco's Modified Eagle Medium
DTPA	Diethylenetriaminepentaacetic acid
ICP	Inductively Coupled Plasma
MRI	Magnetic resonance imaging
MWCO	Molecular weight cut-off
NIR	Near-infrared
^{1}H NMR	Proton Nuclear Magnetic Resonance
NP	Nanoparticle
PBS	Phosphate buffered saline
QDs	Quantum dots
QCE	Quantum confinement effect
QY	Quantum yield
TAS	Transient absorption spectroscopy
TEM	Transmission electron microscopy
UCNP	Upconverting nanoparticle
XPS	X-ray photoelectron spectroscopy
XRD	X-ray diffraction

Chapter 1. Introduction and Background

1.1. Bioimaging – A Necessity to Modern Medicine

Bioimaging aims to visualize biological activity in real time. With today's computer technology, imaging techniques offer complete visualization from subcellular resolution all the way to a whole organism. Non-invasively visualizing a biological system was not available until 1895, when Wilhelm Rontgen, a German physicist and engineer, initially discovered how to generate and detect X-ray radiation.[4] After learning that X-rays can penetrate through objects, he then developed the use of X-rays as an imaging tool for medicine. This has led to the development of mammography, angiography and computed tomography, making it a widely used imaging technique to this day. Bioimaging has become an essential tool in modern medicine as it provides physiological and pathological information without the need for dissection, or other invasive procedures. In response to the very growing need for novel diagnostic tools, an arsenal of probes dedicated to imaging has emerged over the last decade offering the ability to study structural and functional images of living systems and which include computed tomography (CT),[5, 6] ultrasound,[7] fluorescence imaging[8, 9] and magnetic resonance imaging (MRI),[10] among others.

1.2. Fluorescence Imaging

Fluorescence imaging is a technique that utilizes a molecular system capable of absorbing and emitting light. Upon irradiation with light, the absorption of energy excites the system, which promotes the electrons from the ground state to an excited state. The electrons relax back to the ground state resulting in the emission of a photon. This imaging technique has become an asset in bioscience as it allows for the study of biological systems (i.e. from subcellular to animal[11]) with relatively minimal perturbation. For this imaging technique, organic dyes have been widely used and developed by researchers as fluorescent probes. Their widespread usage stems from the fact that they can be tailored according to the desired chemical and optical properties with relative ease, and their commercial abundance.[12]

Despite their extensive use in bioimaging, organic dyes do have their limitations. These organic molecules suffer from poor solubility in aqueous media largely due to their aromatic structure, which is responsible for the molecule's hydrophobicity. However, to mitigate this drawback,

chemical modifications using sulfonate, saccharides, carboxylates and glycol have been proposed and reported.[13] Dyes emitting at longer wavelength (i.e. NIR) such as Atto 740 and Alexa 750 typically possess a relatively low QY,[14] which impacts their overall brightness for imaging. This is attributed to the presence of a larger π-conjugated system that induces more vibrations, which in turn result in an increase of non-radiative pathways. In addition, the size of these fluorophores can refrain scientist from using them as an *in vivo* imaging tool. *In vivo*, owing to their small size, these organic molecules will undergo a relatively fast clearance by the kidneys followed by urinary excretion, or through liver excretion depending on the polarity of the compound.[4] This is detrimental to the temporal imaging window, thus rendering them less ideal for *in vivo* imaging. While these fluorescent dyes have been synonymous with fluorescence imaging, there remains a growing demand for novel non-invasive and more efficient probes. With the advancements of developing tools and materials at the nanoscale, the scientific community has explored the use of nanoparticles in various applications, including bioimaging.

1.3. The Emergence of Nanoparticles

Nanomaterials are defined as materials that are ~1 to 100 nanometers in size (or one billionth of a meter) in at least one dimension. The rise of nanomaterials extends over several decades. The first breakthrough in nanotechnology can be traced all the way back to the beginning of the 20th century. In 1914, Richard Adolf Zsigomondy published his work on ultramicroscopy where he was able to properly visualize gold sols and other nanomaterials at the nanoscale.[15] Although the unit of measurement down to the nanoscale had already been introduced, it was much later that scientists thought about using "very small" particles in the development of novel technologies. It was in 1959, at the annual meeting of the American Society at Caltech, that Richard Feyman's famous lecture entitled "There's Plenty of Room at the Bottom" propelled scientists into investigating the potential of nanomaterials and nanotechnology.[16] In this talk, he inspired the idea of the ability to manipulate individual atoms and molecules. Later, the term "nanotechnology" was first coined by Professor Norio in 1974 in what he described as "the production of technology to get extra high accuracy and ultra-fine dimensions".[6, 17]

Since then, our appreciation and understanding of nanomaterials have considerably grown with the established knowledge at the atomic, molecular, and supramolecular levels. Materials at the nanoscale bridge the gap between bulk and molecular levels leading to many unique properties,

which are otherwise non-existent. With decreasing particle size, the surface area to volume ratio significantly increases. In addition, the high specific surface area introduces enhancements in physicochemical, electrical, optical, magnetic and quantum properties. For instance, super paramagnetic iron oxide nanoparticles (SPIONs) exhibit superparamagnetism, meaning that they are magnetized when an external magnetic field is turned on and do not retain any net magnetization once it is turned off. This property is size-dependent and generally arises in SPIONs with sizes ranging from 10 to 20 nm.[18-21] This unique magnetic property renders them attractive nanotools for efficient localized drug delivery systems, or as imaging probes for magnetic resonance imaging (MRI).[19, 22] In the field of nanomaterials, the aim is to not only develop novel materials and tools, but also to enhance and improve already existing ones. With this in mind, industries have embraced the importance of nanomaterials and have since then shifted their strategies to integrating nanoparticles in their products with the intent of improving current technologies. As a result, NPs have become ubiquitous in many applications in fields such as the automotive industry, aerospace, environmental science, electronics, and catalysis.[23] These materials have also shown great promise in biological applications owing to their small size, which enables the possibility of harvesting information at subcellular resolutions. Indeed, nanotools have are being developed with the aim of pushing the boundaries of the bio- and nanomedical sciences.

1.4. Bioimaging at the Nanoscale

Researchers have sought to engineer nanotools with improved performance over current established imaging probes. For this, the design of an imaging probe should meet the following criteria: (i) The size of the probe should be small enough for cellular uptake and large enough to avoid excretion through the filtration processes in the body; (ii) it should have good colloidal stability; (iii) it should have good biocompatibility, meaning that it should not disturb any biological processes; (iv) it should be bright and have resistance to photobleaching and/or an adequate imaging window time.[24] Numerous nanoparticle-based bioimaging tools have been developed including mesoporous silica nanoparticles, quantum dots and upconverting nanoparticles, among others. These systems offer several advantages over conventional fluorescence imaging dyes including better photostability, resistance to degradation and longer circulation times.

1.4.1. Mesoporous Silica Nanoparticles

Mesoporous silica nanoparticles (MSNs) possess unique features that renders them suitable for many applications such as bioimaging. These NPs possess good biocompatibility, controllable size, and easy surface modifications.[24] In addition, MSNs have a high surface area to volume ratio and pore volume that makes them versatile nanocarriers. To endow fluorescence properties that can be used for bioimaging, organic fluorescent dyes are encapsulated in the pores. This method mitigates the aforementioned limitations of the dyes. MSNs can protect the dye from the surrounding environmental factors that can result in degradation of the optical probe. Results have shown that the dyes have much better photostability when loaded into these NPs and stability is better controlled through surface modifications of the MSNs.[24] In general, the formation of MSNs is based on a sol-gel process that consists of the hydrolysis of tetraethyl orthosilicate and the polymerization to form Si-O-Si bonds around the surfactant. The porosity of the materials arises from the removal of the surfactant template using calcination or chemical extraction.[25] Subsequently, fluorophores are then encapsulated into the pores through electro-static interactions, or *via* covalent bonds. Although these NPs have their advantages over conventional simple imaging dyes, they are severely limited by the low fluorophore concentration (loading capacity) and the possibility of having the dye leach into the environment. In addition, several reports suggest that there is notable toxicity associated with the silanol groups that can interact with the cell membrane.[25]

1.4.2. Quantum Dots

Quantum dots (QDs) are fluorescent semiconductor nanocrystals. These particles possess unique optoelectronic properties that are due to their physical dimensions (typically 2-10 nm in size and approximately 200 to 10 000 atoms).[26] When exposed to a light source, electrons are excited from the valence band to the conduction band (a higher excited energy state). Following this, the excited electron undergoes a relaxation process from the excited state down to the ground state, which brings forth a photon of a frequency equal to the band gap of the two states. These semiconductor-based nanoparticles are capable of absorbing and emitting light at different regions of the spectrum depending on the particle size due to the quantum confinement effect. This effect explains how changes in the particle size directly influence the gap of the valence and conduction bands and the

size-dependent fluorescence.[27] It also dictates how much energy is required to excite an electron from the valence band to the conductance band, as demonstrated in **Figure 1.1**.[28]

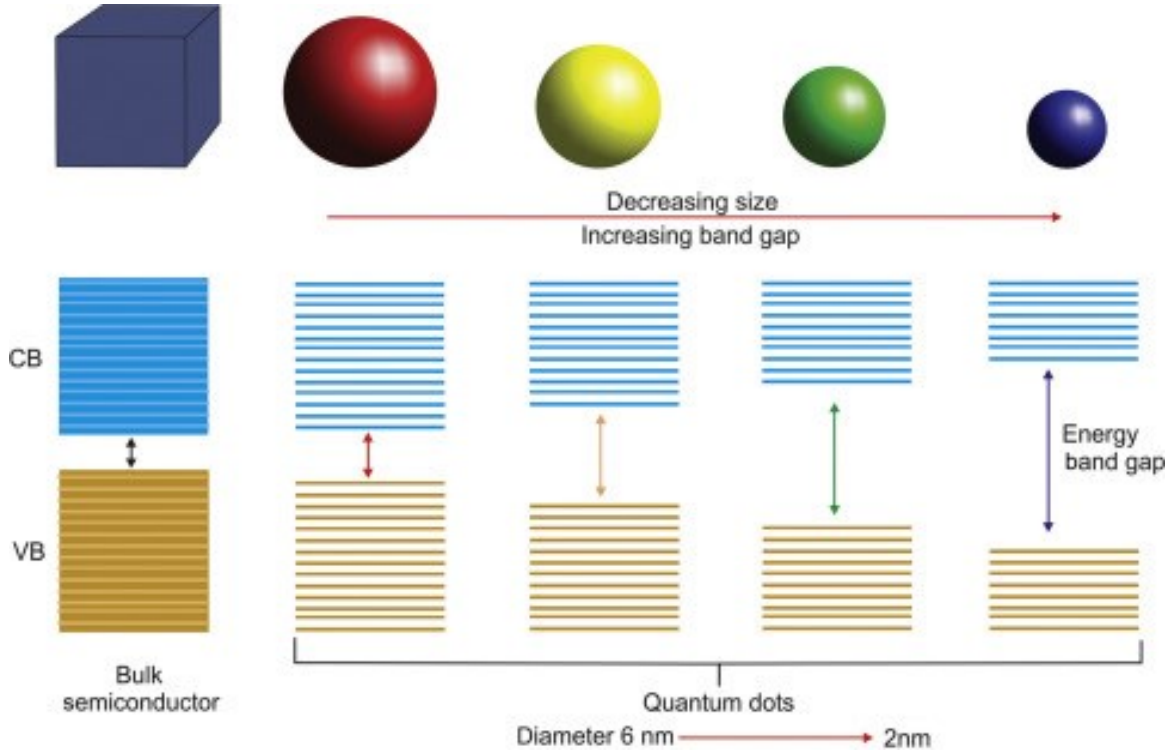

Figure 1.1 Graphical presentation of quantum confinement effect in QDs; the energy band gap decreases as the size of the particle decreases. Image source: Kumar *et al*.[3]

Smaller QDs will undergo greater quantum confinement. As such, it takes more energy to excite an electron with higher energy of the photon emitted, resulting in a more blue-shifted fluorescence. Conversely, larger QDs will require less energy to excite an electron, resulting in a lower energy of the photon emitted and a red-shifted fluorescence. Due to the myriad of interesting optical properties (resistance to photobleaching, high QY and tunable fluorescence), QDs have been extensively studied with particular emphasis on biological applications. However, several concerns arise due to their inherent chemical (generally comprised of cadmium and lead) and cytotoxicity. Reports have shown that QDs can have nefarious side effects *in vivo*, such as influencing lipid metabolism in certain organs or accumulation of toxic metal ions (e.g. Cd, Te, Se, and Pb) in tissues.[27, 29]

1.4.3. Upconverting Nanoparticles

Upconverting nanoparticles (UCNP) comprise trivalent lanthanide ions embedded inside an inorganic host lattice. These nanoparticles have evoked a lot of interest in biological applications as they can be tailored to emit from the UV to the IR depending on the dopant ion and concentration. UCNPs possess an interesting property in that they can upconvert light, meaning that they are capable of absorbing light at longer wavelengths (i.e. NIR) and emitting photons with high energy (i.e. shorter wavelengths). This upconversion process occurs because of the absorption of multiple photons of low energy along with energy transfer processes, allowing for emission of photons of higher energy.[30] This anti-Stokes behavior has garnered interest for bioimaging for many reasons. First, these UCNPs are capable of emitting light in the NIR region located in the second optical biological window. As such, it is possible to exploit low energy light for deep tissue penetration and to mitigate autofluorescence of biological systems.[31] Hence, the possibility of NIR excitation to NIR emission is particularly interesting for *in vivo* bioimaging due to the deep tissue penetration, low absorption and scattering in tissues and organs. In addition, biological materials are generally incapable of upconverting. As a result, the signal-to-noise ratio for two-photon excitation imaging is high. Second, these NPs possess excellent photostability, which has been aptly demonstrated. For instance, *Yu et al*. highlighted the difference in degree of photobleaching between UCNP and two organic labelling dyes, DAPI and Dil. In their photobleaching experiment, they demonstrate that under exposure of a high powered laser at 405, 543 and 980 nm for 400 s, the fluorescence intensity of DAPI and Dil decreased to 2.5% and 1%, while the fluorescence intensity of the UCNP remained at 96%. While many of these properties are desired for biological applications, questions are being raised regarding the safety of these probes: aggregation of the NPs in cells and tissues, chemical decomposition of UCNPs, lanthanide ion leaching, etc.[32] In addition, although these NPs are capable of fluorescing in the NIR using a NIR source through upconversion, the process is relatively inefficient resulting in a low fluorescence QY.

The shortcomings of many of these nanosystems have propelled researchers to discover novel nanoparticles that can offer exceptional performance, stability and low cytotoxicity while offering good biocompatibility. Carbon-based nanomaterials are among the front runners in satisfying these

stringent criteria particularly in regards to biological applications. More recently, one of the newer members of the carbon nanomaterials family, namely carbon dots, have come to light.

1.5. Introduction to Carbon Dots

Since their discovery in 2004 by Xu et al,[33] carbon dots have garnered significant attention over the years for applications in a number of applications owing to their versatile physico-chemical and optical properties.[34] CDs are carbon-based nanoparticles that possess a quasi-spherical structure with a mean particle size of 10-15 nm. They are predominantly amorphous with a mixture of sp^2/sp^3 carbons. CDs are typically composed of carbon, oxygen, hydrogen and nitrogen.[35] The growing interest in these dots stems from the fact that they can be prepared from wide range of carbon containing compounds. CDs can be prepared from heterogeneous compounds (e.g. orange juice[36], candle soot,[37] milk[38-40], etc.) to simple molecules (citric acid,[41] sugars,[42, 43] amino acids[44], etc.). Due to the complex composition of heterogeneous compounds, CDs generally show a broad distribution of properties. Thus, in order to synthesize CDs with uniform properties and high batch-to-batch reproducibility, it is preferable to work with well defined and simple precursors as they play a key role in the dots' properties. For instance, they dictate functional groups on the surface of the dot, which in turn influences hydrophilicity and colloidal dispersibility. The CD surface chemistry is versatile and can be tailored for a desired functionality *via* careful selection of the precursors or through post-synthesis modifications.[45]

One of the most interesting properties of CDs is their tunable fluorescence signature. These dots can be prepared to fluoresce in the UV, visible or near infrared regions of the spectrum. They offer high fluorescence QYs often ranging from 10-80%.[46] Several works have shown that these dots can be resistant to photobleaching and photoblinking, which may point to their advantage relative to dye molecules.[47] Moreover, the literature seems to support the fact that they possess low cytotoxicity and good biocompatibility.[35, 48] It is no surprise that they have been investigated for bioimaging applications.

1.6. Synthesis

To date, several synthetic methods that have been reported for the preparation of carbon dots. These strategies are divided into two categories namely top-down and bottom-up syntheses. In a

top-down approach, CDs are derived from the breakdown of bulk materials, whereas in a bottom-up approach, the CDs are synthesized from molecular precursors.

1.6.1. Top-down Synthesis

Early CD preparation methods typically consisted of top-down approaches relying on the breakdown of larger carbonaceous structures (*e.g.*, graphite) into smaller nano-sized dots.[49] In fact, CDs were accidently discovered in the arc-discharge of candle soot intended for the preparation of carbon nanotubes.[33, 34] Other examples of top-down syntheses of carbon dots consists of breaking down carbon nanotubes and graphene oxide *via* arc discharge,[33] laser ablation[50] and electrochemical oxidation.[51] While these synthesis methods result in a high yield of material, a common characteristic for top-down synthesized CDs is the low fluorescence quantum yields (1.1-1.5%)[52] requiring further passivation to enhance their optical properties.[34, 50, 53, 54] For instance, Dang *et al*.[55] designed a protocol for a large scale preparation of white fluorescent carbon dots through a one-step ultrasonic treatment of polyamide resin. Although they reported that the technique can be easily used for large-scale synthesis, they noted that the CDs required a silane coupling co-passivating agent (KH570) to significantly improve the QY (~28%).

1.6.2. Bottom-up Synthesis

Bottom-up routes include hydrothermal,[56] microwave[57, 58] and thermal oxidation syntheses[59, 60], which potentially allow for control and tunability of the physical and optical properties of the sample. In this approach, the formation of CDs stems from the condensation, polymerization, carbonization and passivation of organic molecules containing -OH, -COOH, -C=O and NH_2 groups which act as both precursors and surface passivation agents. The synthesis typically requires moderately high temperatures (160-240 °C) and usually results in highly fluorescent CDs, which do not require further passivation.[61] The interest in bottom up methods arises from the easy setups, low cost and convenience of using generally non/low-toxic precursors. However, the main challenge with these techniques is the synthesis scale, typically milligrams to grams, and production yields as low as 1%.[62, 63]

1.7. Fluorescence Mechanisms

The optical properties of CDs are heavily influenced by the surface composition, which plays a major role in dictating the fluorescence signature. Passivating the surface can enhance the optical

properties more specifically the QY of fluorescence.[47, 60, 64] While the mechanism of surface passivation remains unclear, it is generally accepted that it involves the introduction of functional groups containing electron-rich heteroatoms. These act as good electron donors, which decreases the contribution of non-radiative processes that quench the carbon dot fluorescence.

CDs can exhibit excitation-dependent or -independent fluorescence. The former implies that variation of the excitation wavelength will result in a blue or red shift of the fluorescence band.[48, 65] In this case, a single system can generate fluorescence in multiple regions of the spectrum. On the other hand, excitation-independent fluorescence refers to fluorescence that is independent of the excitation wavelength. This is believed to be dictated by the energy states at the surface.[35, 48, 66] Passivating the carbon dots often results in excitation independent fluorescence. Although there have been numerous studies on CDs with intriguing optical properties and an optical signature from the UV to the NIR range,[67-72] its fluorescence mechanism remains a topic of debate. Shedding light on the fluorescence mechanism of CDs, has been of great interest for many research groups as it provides insights on how the dots' emission color can be tailored for target applications.[60]

1.7.1. Surface Functional Groups

CD fluorescence is largely controlled by the surface states, where fluorescence centers are formed by the synergy of the sp^2 and sp^3 carbon backbone with functional groups. Dong *et al*.[73] studied the steady-state optical properties of their CD system prepared from citric acid and cysteine. They noted the presence of three prominent absorbance bands centered around 230, 242 and 345 nm; the first band was assigned to citric acid and cysteine, the second to the aromatic sp^2 domains and the last was attributed to the trapping of excited-state energy by the surface states. They argued that the fluorescence is non-existent at the sp^2 aromatic domain and that it was primarily due to the surface states. They concluded in their work that introducing additional functional groups to their CD system (citric acid alone vs. citric acid and cysteine) also imparted surface states that facilitated high yield of radiative recombination that decreased the required energy to promote an electron to the excited state. The presence of certain functional groups can influence the energy levels of the CDs, as was shown by Zhang *et al*. and *Chen et al.*[2, 74] In their work, they prepared CDs with ammonium citrate, EDTA and DMF. Depending on the ratio of each ingredient, they were able to synthesize CDs fluorescing in different regions of the spectrum. They highlighted that

the color shifts were due to the energy levels and electron transitions of the C=O and C=N surface functional groups. In essence, the abundant surface functional groups generated additional energy levels (referred to as HOMO-1 and HOMO) that allowed for efficient electron transitions to the LUMO (**Figure 1.2**).

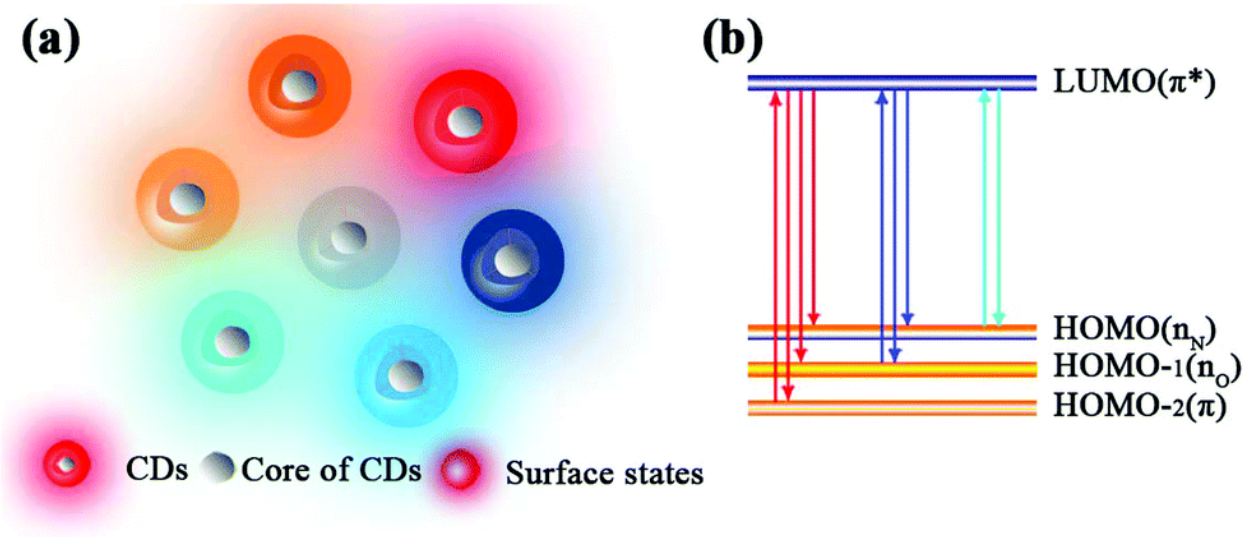

Figure 1.2 (a) Structure of multicolor CDs; (b) Schematic illustration of the proposed energy level and electron transition diagrams of the CDs. Image source: Zhang *et al*.[2]

1.7.2. Surface Oxidation

In the same vein, it has been demonstrated that fluorescence of CDs can be tailored *via* surface oxidation. The higher the degree of surface oxidation, the more red-shifted the fluorescence. This is due to the formation of greater surface defects that decreases the bandgap, resulting in a red-shifted emission.[52] Liu *et al*. demonstrated that two CD-systems of the same size distribution possessed similar chemical groups. However, they noted a difference in the degree of surface oxidation. Consequently, this resulted in a red-shifted fluorescence from 518 nm to 543 nm and attributed to the decrease of the band gap of the HOMO and LUMO.[75] This trend was also observed by Ding *et al*. as shown in **Figure 1.3**. They separated various CD samples based on their polarities using silica column chromatography, which coincided with their degree of oxidation. The synthesized CDs possessed fluorescence maxima ranging between 440 nm to 625 nm. Similar

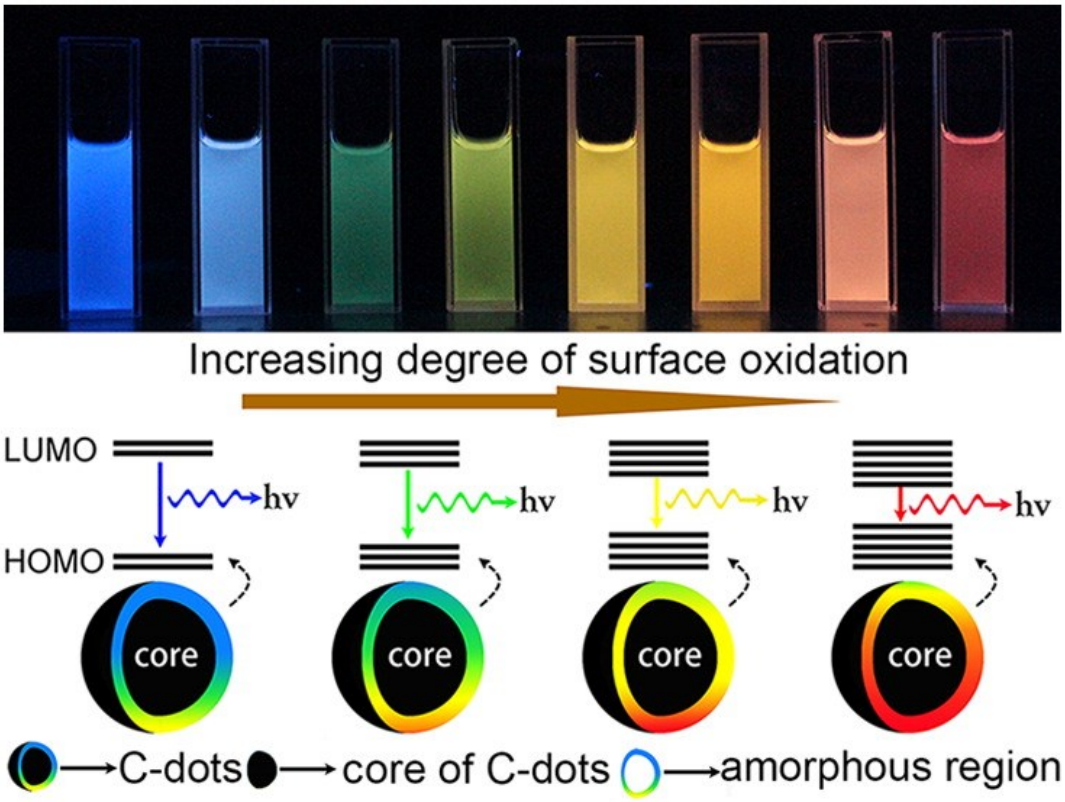

Figure 1.3 Eight CD samples under 365 nm UV light. The corresponding emission of each samples (left to right) is 440, 458, 517, 553, 566, 580, 594 and 625 nm. The observed red-shift in fluorescence signatures stems from the increase in degree of oxidation that result in a decrease in bandgap. Image source: Ding *et al*.[1]

observations were also noted by Jiang *et al*.[76] They prepared CDs that fluoresce in different colors (blue, green, yellow, and red emissive dots) and stipulated that the increase in fluorescence wavelength was due to the increase in C=O content in the CD system.

1.7.3. Quantum Confinement Effect

Quantum confinement effects (QCE) have been reported in carbon dots, where the photoluminescence is dictated by the size of the NPs as shown in **Figure 1.4**.[54, 77] This phenomenon arises when the size of a NP approaches the De Broglie wavelength, which produces quantum effects not observed in the bulk material. Electrons will behave like a particle in a box where the size of the box (in this case, the diameter of the CDs) dictates the size of the nanoparticles' band gap, which in turn is responsible for the wavelength of the emitted photons. As the size of the particle decreases, the bandgap size increases, resulting in a red-shifted fluorescence (low energy). Conversely, as the particle size increases, the bandgap size decreases,

and a red-shifted fluorescence is observed.[60, 78] Although not as common as the other mechanisms, in the case of CDs, the fluorescence is influenced by the QCE of conjugated π electrons; these electrons are located at the carbon core-states of the dots. The larger the aromatic network (or the sp^2-domain), the smaller the bandgap, and the more red-shifted the fluorescence will be.[79] The size of the conjugated network can be tuned to modulate the fluorescence of the CDs as demonstrated by Tian *et al*.[80] They prepared CDs with citric acid, urea and three different solvents (water, glycerol and dimethyl formamide) *via* a solvothermal treatment. They reported that the different solvents resulted in the formation of dots with carbon cores of different sp^2-domain sizes, which in turn led to fluorescence in blue to red fluorescence. Li *et al*. highlighted the optical properties of their system were primarily influenced by the size of their CD systems (and the size of the aromatic core). They noted that removing surface oxidation by hydrogen plasma did not affect the fluorescence and concluded that the fluorescence arose from the quantum confinement effect and the size-dependent properties of the dots.[81]

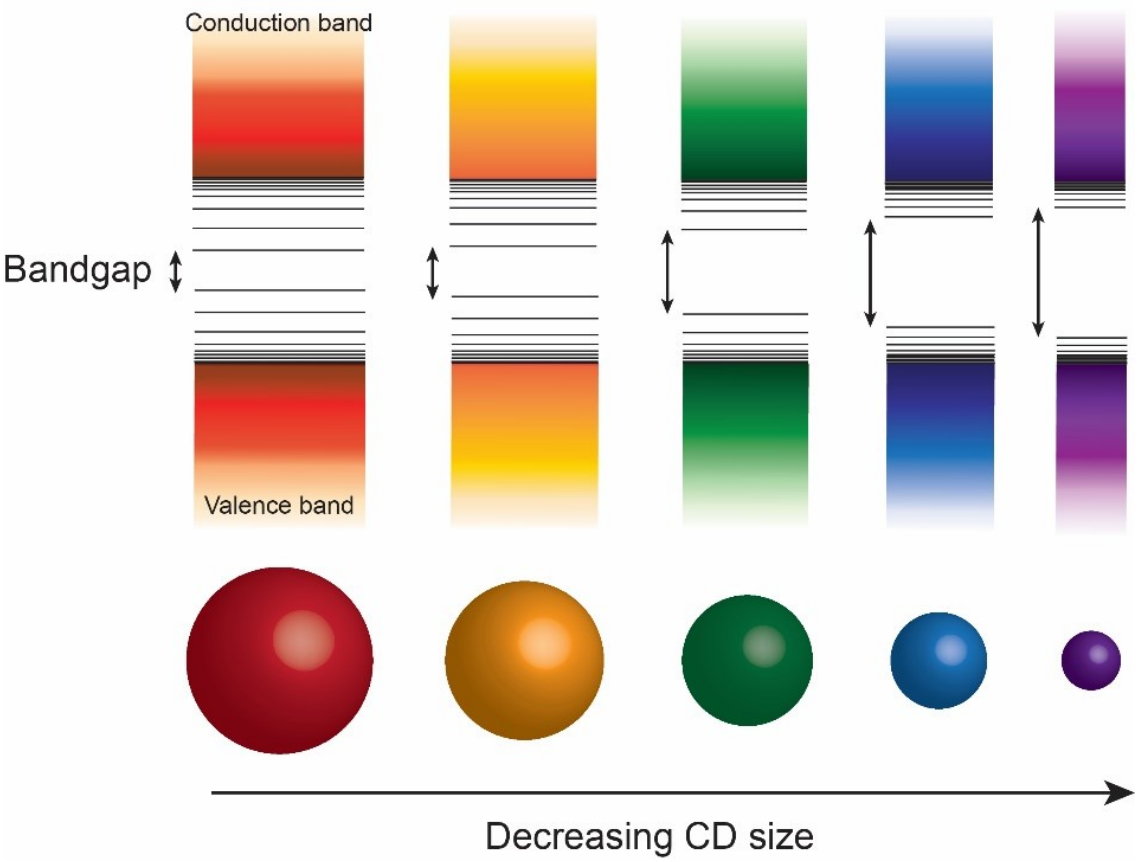

Figure 1.4 Graphical presentation of the quantum confinement effect.

1.7.4. Core- and Surface-States / Core- and Molecular-States

Numerous findings have suggested that multiple emissive states are responsible for the fluorescence for CDs.[2, 82] For example, a combination of both the core and surface states have also been suggested. Overall, the fluorescence stemming from the surface states has a much higher QY and is considered to be the main contributor to the observed optical properties. On the other hand, the core is responsible for the fluorescence that is more photostable. Miao *et al*.[83] highlighted the presence of both states in their temperature studies. They noted that CDs can be treated as a conjugated graphite core with functional groups on the surface. As such, the bandgap of the nanoparticle is dependent on both the sp^2-network size and the presence of functional groups. By adjusting the extent of graphitization (i.e. core size) and the amount of functional groups, they were able to tune the emission of the CDs from 430 to 630 nm. Also, Nie *et al*. demonstrated the possibility of multiple photoluminescence centers in their CDs. They assigned the blue

fluorescence to the core state and the red-shifted fluorescence, to the surface groups.[84] They demonstrated that addition of C=O and C=N surface functional groups introduced new electronic transitions resulting in changes to the observed fluorescence spectrum. Studies on CD systems with fluorescence stemming from the core- and surface-states highlight that the emission arises from direct excitation of the surface-states or *via* energy transfer from the core-states.[60] As a result, the fluorescence of these nanoparticles can be tuned by either controlling the sp^2-network size (core-states) or by modifying the chemical groups formed on the surface (surface-states).

Similarly, supporting evidence also shows a multi-state fluorescence mechanism known as the carbon core and molecular state mechanism.[60, 85, 86] Reports have suggested the possibility of the presence of organic molecules or chromophores (similar to dye molecules) present in the CD. These fluorophores are present throughout the CD structure, both on the surface and inside the carbon backbone. This typically occurs with CDs prepared using a bottom-up approach. For this mechanism, it is believed that fluorophores are formed by the precursors followed by the nucleation of the carbon core, which continues to grow through the consumption of the fluorophores (**Figure 1.5**). The fluorophores are situated at the surface and/or interior of the carbon backbone of the CDs. In such a case, fluorescence exists in both the molecular- and the carbon core-states. Groups such as Krysmann *et al*.[87] have demonstrated the presence of these multiple states. In their work, they prepared CDs using citric acid and ethanolamine at different temperatures. Through mass spectrometry and ^{1}H NMR analyses, they were able to suggest the formation of a molecular precursor (fluorophore) formed during pyrolysis. This intermediate strongly fluoresced and was the primary contributor to the CDs' optical properties. Lu *et al*.[88] investigated the synergistic effect of the molecular- and core-states of their CD system that was used for NIR bioimaging. They noted that at a low reaction temperature (150 °C), large molecules or crosslinked molecules were formed rather than a carbonized structure for dots prepared from dopamine and o-phenylenediamine. These molecules strongly fluoresced in the red region of the spectrum and were postulated to be the main contributor to the overall fluorescence. At a higher temperature (200 °C), a carbon core is formed, with the aforementioned molecules linked to the core. At elevated temperatures (250 °C), the dot was completely carbonized with the fluorescence mostly arising from the carbon core evidenced by the blue emission. Similar to the core-and surface-states, this mechanism showcases the possibility of energy transfer between different states in addition to direct excitation of the fluorescence centers.[60]

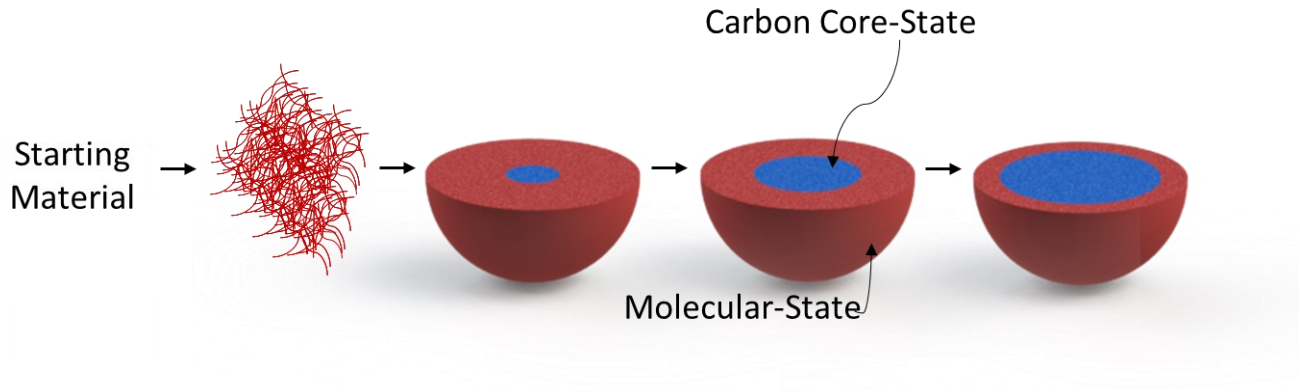

Figure 1.5 Graphical representation of the carbon core- and molecular-state fluorescence mechanism. At carbonizing reaction conditions, fluorophores are formed by consuming the starting material, followed by the formation of the carbon core. The latter increases in size through fluorophore consumption as the reaction progresses.

1.8. Development of Carbon Dot-Based Bioimaging Nanotools

Due to their versatile optical properties, CDs have gained a lot of traction in biologically oriented applications, most notably bioimaging. For such applications, another crucial prerequisite is having good biocompatibility and low cytotoxicity. Numerous *in vitro* studies have reported low cytotoxicity at concentrations well above working concentrations (as high as 5 mg/mL).[8, 35], [89] Exploiting the excitation dependent fluorescence of CDs can also allow for the development of multicolour imaging probes for membrane studies and cell imaging. For instance, Pan *et al*. reported a one-step microwave synthesis of CDs obtained from citric acid and formamide at 160 °C for 1 hour as shown in **Figure 1.6**.[65] The resulting CDs were approximately 7 nm in size and presented a full color excitation-dependent emission that can almost span the entire visible spectrum when excited from 300-600 nm. The emission maxima were noted at 466, 550 and 637 nm following excitation at 360, 450 and 540 nm, respectively. A broad absorbance band was noted, indicating the presence of multiple electronic states that are responsible for the excitation-dependent fluorescence behaviour. The blue fluorescence was postulated to stem from the aromatic structures, while fluorescence at longer wavelengths was ascribed to the presence of C=N, C=O and C-N bonds. They determined that the cytotoxicity of the dots was low, with over 85% cell viability observed after 24 hours of incubation with MCF-7 cells at concentrations ranging from 10 to 50 μg/mL. Interestingly, confocal fluorescence images of the CD-treated MCF-7 cells

revealed fluorescence throughout the entire cell; this signified that the dots not only passed through the membrane, but also the cell nuclei. These results were interesting as the majority of CD bioimaging publications report localization in the cytoplasm and accumulation just outside the nucleus,[90, 91] while few report entry into the nucleus.[92] Each CD system behaves differently depending on the biological system. As such, there may be circumstances where researchers are interested in studying a specific organelle in a cell. Systems absorbing and fluorescing at lower energy light (red-shifted wavelength) are sought after due to their biological advantages namely minimal autofluorescence in the biological matrix and reduced photodamage in comparison to UV and visible light.[70, 93-95] Only a few such systems have been reported as CDs typically emit in the blue or green regions of the spectrum.[60]

A study by Lin's research group described the development of NIR emitting CDs synthesized using glutathione and formamide for two-photon fluorescence imaging.[70] The synthesized CDs exhibited a maximum fluorescence at 683 nm when excited at 420 and 850 nm (NIR femtosecond pulse laser) with a QY of 16.8%. The fluorescence was believed to have originated from the surface states, where the aromatic structures containing C=O, C=N and C=S bonds are responsible for the low energy emission. The cytotoxicity study revealed over 80% cell viability for MCF-7 cells after 24 hours of incubation at concentrations up to 500 μg/mL. Finally, they demonstrated that the dots can enter in the cells and that can be used as bioimaging probes under a one- or two-photon excitation regime. Ding *et al*. pushed the capabilities of red emissive CDs beyond *in vitro* cell imaging. In their work, they developed red-emissive CDs (627 nm) that were effectively used for both *in vitro* and *in vivo* imaging.[93] The red emission was believed to stem from both the nitrogen- and oxygen-related surface states and nitrogen-derived structures in the carbon core. Strong red fluorescence signals were observed at the injection site in a nude mouse model since the red fluorescence readily penetrates through skin and tissues.

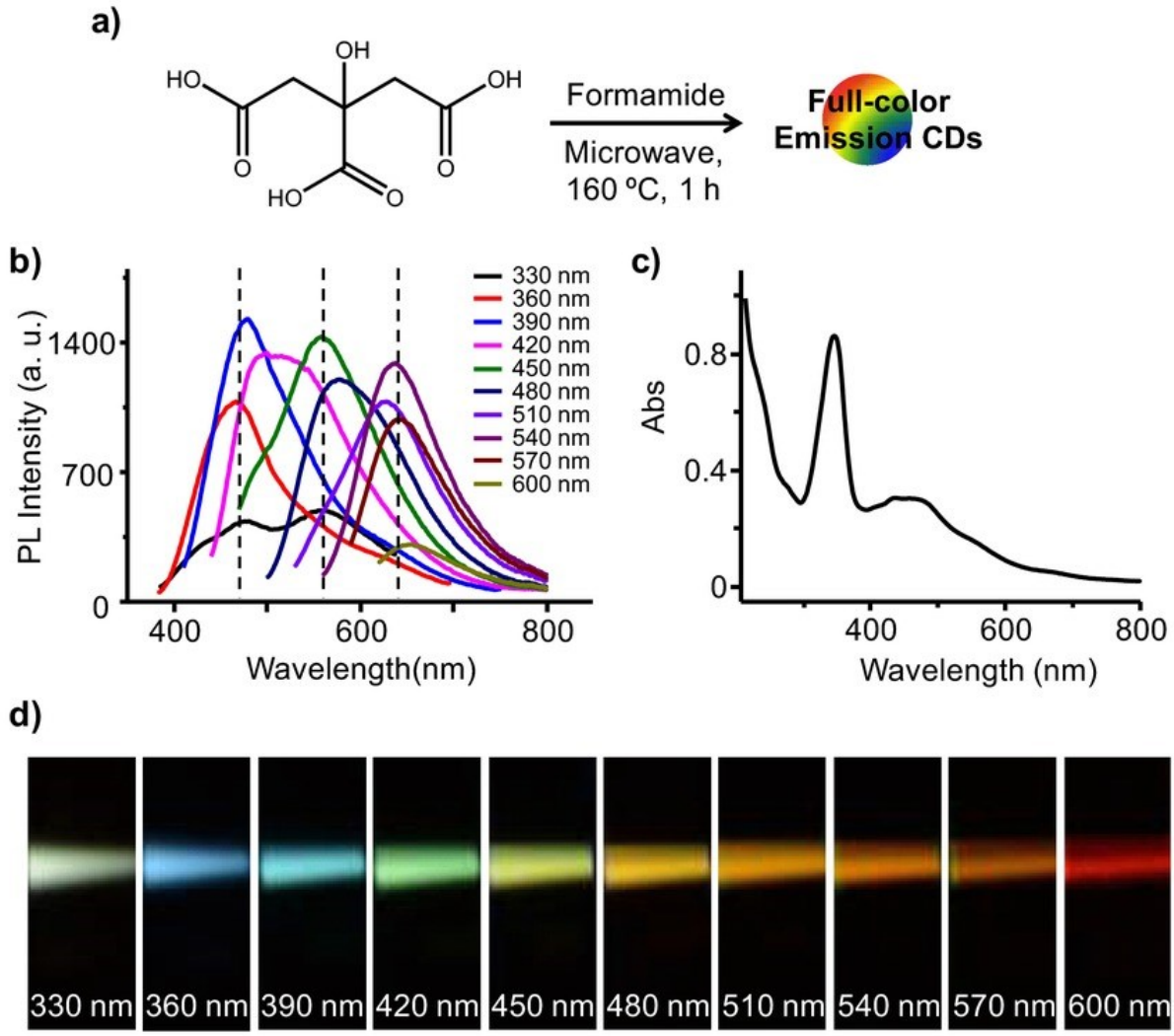

Figure 1.6 (a) Reaction scheme of the excitation-dependent fluorescent CDs; (b) excitation-dependent fluorescence profile of the CDs; (c) broad absorbance spectrum of the CDs, indicating the presence of multiple electronic states; (d) fluorescence emission of the CDs in aqueous solution upon irradiation from 330 to 600 nm. Image source: Pan *et al*.[65]

1.9. Statement of the Problem

Bioimaging has become the springboard for the advancement of modern nanomedicine. The anatomical, physiological, and molecular information acquired in real time allows us to further our understanding of biology, which in turn enables researchers to develop better theranostic techniques. With a growing demand for non-invasive novel diagnostic tools to quickly and precisely harvest additional information relative to conventional imaging methods, the potential for nanomaterials continues to be touted owing to their unique physical, chemical and optical properties. Numerous nanoparticle-based bioimaging tools have already been developed as

previously mentioned; however, while they do offer certain advantages, they also possess numerous drawbacks. Carbon dots have recently come to light as a potential and suitable alternative that can address many of these drawbacks owing to their unique and attractive properties. Yet despite this, there remains a significant knowledge gap in our understanding of their fluorescence mechanism(s). As such, many CD publications overlook or provide no compelling evidence on the origins of the fluorescence, which is crucial to develop sensitive and effective bioimaging and sensing applications.

Furthermore, the majority of studies relating to CD-based imaging probes are limited to solely demonstrating the localization of the NPs in various cellular organelles. This is unfortunate as CDs possess many interesting fluorescent properties and surface functionalities that can be exploited. In order to push the envelope of diagnostics, imaging probes should provide more than anatomical information. In fact, utilizing a fluorescence probe with sensing capabilities would allow for harvesting a multitude of information otherwise inaccessible using a single diagnostic tool. Currently, there exists reports of systems capable of providing real-time intracellular information on pH and/or temperature using CDs.[96] However, the majority of these probes utilize fluorescence intensity-based measurements, a method that is limited by sample concentration-dependence and heavily influenced by external factors. These measurements can be useful in a closed system (i.e. a cuvette model). However, in a more complex environment like cells, many elements such as changes in the matrix, cellular uptake and detection efficiency can hinder the overall signal measured using a fluorescence microscope. This translates to a lack of precision or simply the inability to perform the measurements. Therefore, intensity-based measurements are not ideal in a biological system. Taking this into account, utilizing a system with two distinct fluorescence bands would be an attractive alternative as it would allow for ratiometric measurements that are independent of the concentration of the probe or environmental factors.

1.10. Project Objectives

This work focuses on the synthesis of dual fluorescent carbon dots for the development of multi-sensing ratiometric imaging probes using fluorescent carbon dots. The CDs are prepared *via* both microwave- and solvothermal-mediated approaches and we systematically investigate the effect of the reaction conditions on the resultant optical and physical properties of the dots. Comprehensive characterization is carried out to assess the changes in the physical properties of the CDs using: (i) TEM, for size and morphology, (ii) XRD for phase and crystallinity, (iii) Raman spectroscopy to verify the order/disorder states in the structure of the dots, (iv) FT-IR and (v) XPS spectroscopies to study the surface composition. Moreover, in order to glean insights in to the mechanism of fluorescence, we rely on steady state and ultrafast dynamic spectroscopic techniques including: (vi) UV-Vis absorbance and (vii) fluorescence spectroscopies along with (viii) transient absorption spectroscopy and (ix) picosecond (ps) timescale lifetime measurements.

Following an intimate understanding of our CD system and through additional characterization, we target the development of precise temperature and pH sensors for biological systems. In both cases, the goal was to develop a reliable, reproducible and precise ratiometric approach exploiting the dual fluorescence signals (blue and red bands) of the dots. Both temperature and pH sensing were investigated in the cuvette model as a function of the relevant biological media and conditions (e.g. DMEM buffer, pH, temperature).

The work was extended beyond the cuvette system and into model cell lines namely live HeLa and Glioblastoma. We assess the cytotoxicity of the CDs to validate their use in our model systems. Subsequently, *in vitro* thermal sensing is performed by monitoring the changes in the optical properties *via* fluorescence microscopy, following heating and cooling of the cells. Similarly, *in vitro* pH sensing is performed by inducing pH changes (using lysosomal-pH change-inducing drugs such as metformin and diclofenac) into CD-treated glioblastoma.

1.11. Thesis Organization

The first chapter of this thesis is an introduction to bioimaging and the use of nanoparticles as an alternative to organic fluorophores. This introductory chapter also provides a literature review on various types of nanoparticle systems with a focus on carbon dots and their potential to address drawbacks highlighted for other nanomaterials. The aim of this chapter is to deliver background information complementary to the introduction sections found in the subsequent chapters of the thesis.

Chapter 2 describes the synthesis and the characterization of dual-emissive carbon dots. This work sheds light on the fluorescence mechanism. This idea was developed based on an observation made by the author during the synthesis of the nanoparticles. The author performed most of the experimental work with the assistance of Tayline De Medeiros except for the electrochemical analyses (Francisco Yarur) and the transient absorption spectroscopy data acquisition (Dr. Michela Gazzetto). *The manuscript was submitted.*

Chapter 3 extends the work on the carbon dots as a nanothermometer. The idea was developed based on the dual emission of the carbon dots that could potentially be exploited for sensing applications. The author aimed to investigate the effects of temperature on the fluorescence signature of the nanoparticle. The work was published in Nanoscale Advances. Dr. Dilan Jaunky provided training and assisted in the cell viability and cell imaging experiments. *This work was published as a cover article in Nanoscale Advances (Nanoscale Adv. 2019, **1**, 105-113).*

Chapter 4 presents the use of carbon dots to monitor intracellular pH in live Glioblastoma. This idea was developed with the observation made by the author where it was noted that varying the pH of the environment impacted the shape of the red fluorescence band. *This work was published as a cover article in Particle & Particle Systems Characterization (Part. Part. Syst. Charact. 2019, **37** (1), 1900430).*

Chapter 5 presents concluding remarks encompassing the research presented in the previous sections.

Chapter 6 focuses on future research directions aimed at furthering our understanding of the cell-CD interactions and the cellular entry mechanism(s). Another work proposed, which has been

initiated by the author, is on the development of bimodal imaging probes for fluorescence and magnetic resonance imaging using these dual fluorescent carbon dots.

Chapter 2. Elucidating the Mechanism of Dual-Fluorescence in Carbon Dots

2.1. Abstract

Carbon dots have garnered significant attention owing to their versatile and highly tunable optical properties. Of interest are dual fluorescent dots that can exhibit multiple fluorescence bands following excitation with an appropriate wavelength of light; however, the origins of their fluorescence and the underlying mechanism remains a subject of debate. Here, we have prepared dual-fluorescent carbon dots from glutathione and formamide precursors *via* a one-pot solvothermal synthesis. Following comprehensive characterization efforts using steady state and dynamic techniques, our findings indicate that these dots possess two distinct emissive states, a carbon-core and a molecular state, which are respectively responsible for the blue and the red optical signatures. We demonstrate that the coexistence of these states is dependent on the synthesis conditions, especially time, which can be used to tune the optical properties. To further glean information into the fluorescence mechanism, electrochemical analysis was used to measure the bandgaps for the two states while femtosecond transient absorption spectroscopy experiments supported the two-state model based on the observed heterogeneity and spectral bimodal distribution. Our findings provide novel information on the fluorescence mechanism of dual fluorescent dots and can be extended to other carbon dot systems. A fundamental understanding of the optical properties at the nanoscale can translate to more effective and targeted application development particularly in bioimaging, multiplexed sensing and photocatalysis.

2.2. Introduction

Carbon dots (CDs) are luminescent carbon-based nanoparticles that are predominantly amorphous with an sp^2/sp^3 carbon network. These quasi-spherical carbonaceous material are typically 10-15 nm in size and can be prepared from a variety of bottom-up (pyrolysis,[57] hydrothermal,[56] *etc.*) and top-down (arc-discharge,[33] laser ablation,[50] *etc.*) approaches. They are primarily comprised of carbon, oxygen, hydrogen and nitrogen with the overall composition heavily dependent on the precursors used and reaction conditions. CDs stand out relative to other luminescent nanomaterials such as quantum dots and upconverting nanoparticles due to their facile and scalable synthesis from cheap and abundant precursors such as amino acids and sugars.[42-44, 97-100]. Carbon dots have

gained considerable attention since their accidental discovery in 2004 by Xu *et al.*[33] This is due to the myriad of attractive electronic and optical properties, tunable features (size and surface chemistry), low toxicity and high chemical stability.[47, 101, 102] These properties can be advantageous for many applications such as catalysis, bioimaging, sensing and drug delivery, among others.[8, 34, 35, 46, 103]

The CDs' tunable optical properties are some of their most interesting features as they are capable of fluorescing throughout the UV to near-infrared (NIR) regions of the spectrum with low photobleaching and photoblinking.[47, 104] However, the challenge persists with respect to understanding the fundamentals in the underlying mechanisms of formation and fluorescence. There are several well-founded hypotheses relating to the fluorescence mechanism of these nanoparticles.[85, 86, 105, 106] Unlike quantum dots, CDs do not necessarily exhibit a correlation between size and emission wavelength. Instead, the optical properties are influenced by the composition of the surface and the core.[107-109] For instance, Sciortino *et al*. noted that CDs of varying sizes did not display a consistent blue shift with decreasing particle size and described that quantum confinement effect is not present in this system.[110] CDs are conventionally considered to possess multiple emission centers, namely core and molecular states;[60, 70, 111] the former is dependent on the π-conjugated network at the carbogenic-core of the system, while the latter is dictated by the presence of fluorescent molecules primarily attached to the surface of the CDs. Song *et al*. demonstrated that fluorescence originated from both molecular states and carbon-core states with a CD-system based on citric acid and ethanolamine.[112] Through systematic studies, they determined the formation of a highly fluorescent intermediate fluorophore, IPCA, and of the carbon core. While the fluorescence core produced weak excitation-dependent fluorescence, the bound fluorophores are characterized by strong excitation independent fluorescence. This knowledge has led to the study of CDs for sensing applications. For instance, Yarur *et al.*[113] demonstrated with their metal quenching experiments that one of two fluorescence centers was quenched upon interaction with an analyte suggesting the presence of core and molecular states. The latter is primarily located at the surface and interacting with the CD environment.[111] However, there are other studies, which point to the fact that the fluorescence is dramatically influenced by the degree of crystallinity of the core,[109, 114] or by the adsorbed molecules and impurities on the surface.[115] The existence of many of these hypotheses and mechanistic theories

speaks to the need for extensive studies that will better allow for an understanding of the synergy of the surface and the core in a CD and how this can influence the optical properties.

Herein, we aim to further our fundamental understanding of the fluorescence mechanism of CDs. To achieve this, we extensively investigated the physico-chemical and optical properties of CDs prepared from glutathione and formamide. The CDs were prepared at different reaction times to study the evolution of their physical and optical properties, with careful purification to avoid any signal contribution from impurities or reaction intermediates. We rely on characterization techniques such as TEM, X-Ray and Raman spectroscopy to study the physical properties, which can be associated to the observed changes in the optical properties. As shown in previous works,[46, 70, 116] these nanoparticles possess unique optical properties with two distinct fluorescence signatures in different regions of the spectrum (blue and red), which are believed to originate from different emissive states: the molecular and carbon-core states. Steady state optical characterization highlights this unique property and evidences correlation between the length of the reaction time and the optical signature. To shed light on the fluorescence mechanism of the CDs and probe the various emissive states, electrochemical and ultrafast femtosecond transient absorption spectroscopic investigations were carried out enabling the study of the dynamics of the photoexcited system. Here it is revealed that both techniques emphasize not only the presence of two prominent states responsible for the blue and red fluorescence, but also suggest an interplay between the core and molecular states.

2.3. Results and Discussion

2.3.1. Physical Properties Characterization

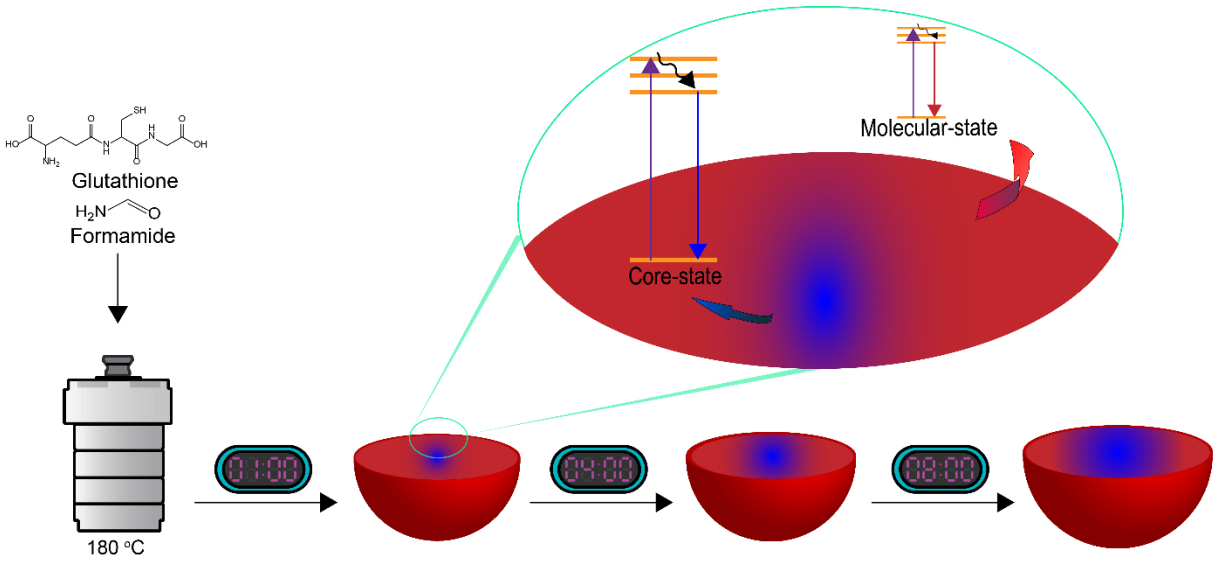

Figure 2.1 Preparation of dual-fluorescent CDs with glutathione and formamide. The CDs were prepared *via* solvothermal assisted reaction at 180 ºC with different reaction times. Such change in reaction parameters results in the CDs exhibiting different fluorescence signatures in both the blue and red regions of the spectrum, which stem from the core- and molecular-states, respectively.

As shown in **Figure 2.1**, all the CDs were synthesized at a temperature of 180 ºC while varying the reaction time from 1 to 8 hours (CD-1, CD-2, CD-4 and CD-8 correspond to a 1-hour, 2-hour, 4-hour and 8-hour reaction time, respectively). Shorter reaction times did not result in any appreciable CD yield and thus the minimum time was maintained at 1 hour. The colloidal dispersion of each sample showcased a different color, with increasing reaction times, ranging from a green to a brown-green hue (**Figure S2.1**). The size and the morphology of the dots were investigated using transmission electron microscopy (TEM). The TEM micrographs (**Figure 2.2**a-d) indicate that the CDs are quasi-spherical with sizes ranging from 12-15 nm. We note an appreciable overlap in the reported sizes according to the particle size statistics, which evidence sizes of 11.9 ± 3.5, 11.3 ± 2.7, 13.3 ± 3.9 and 15.3 ± 4.0 nm for CD-1, CD-2, CD-4 and CD-8, respectively. The XRD diffraction patterns for carbon dots usually present a broad amorphous halo spanning from 10 to 80° due the lack of crystallinity in these materials, as observed for CD-1 (**Figure 2.2**e).[113, 117] However, with the increasing reaction time an increasingly crystalline profile

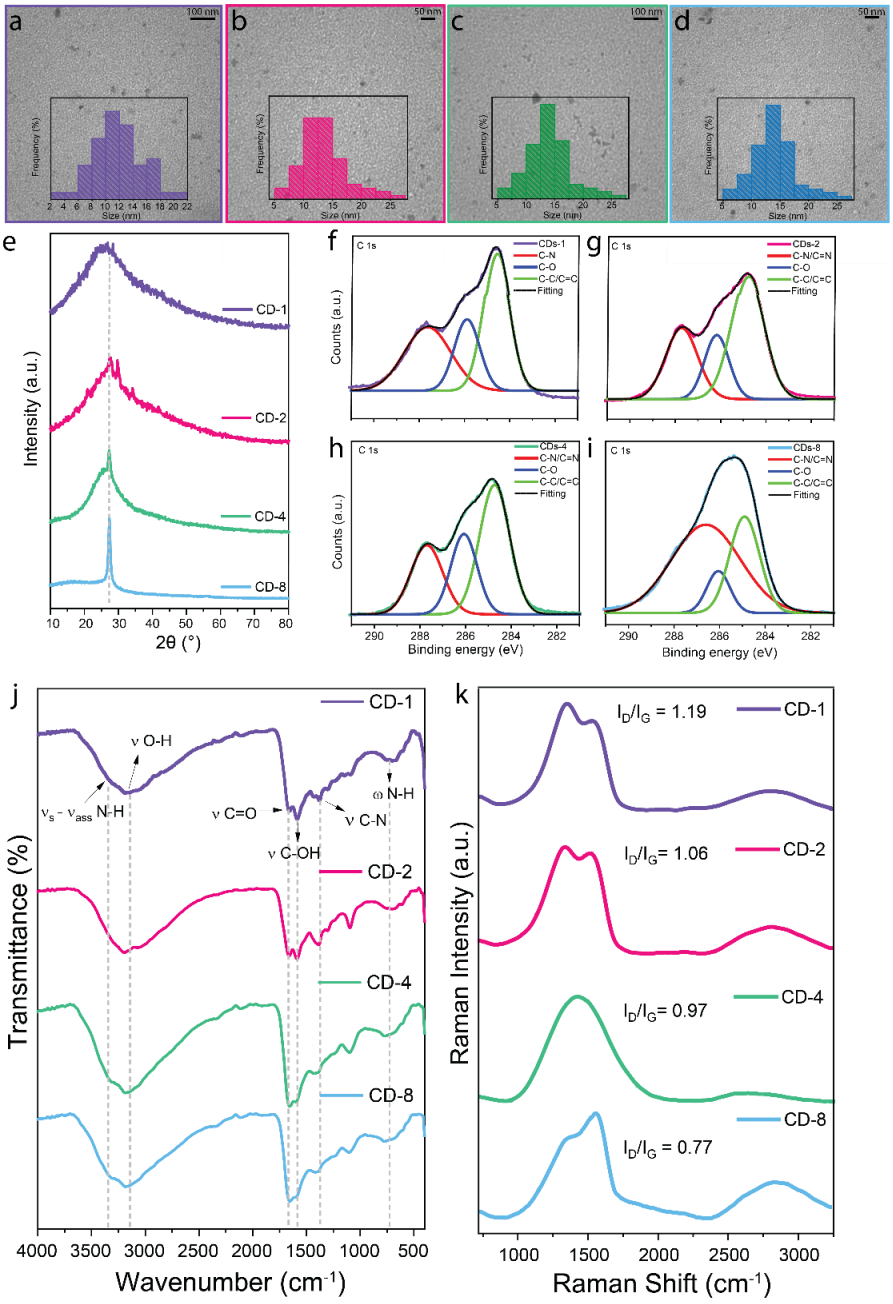

Figure 2.2 TEM images of (a) CD-1, (b) CD-2, (c) CD-4 and (d) CD-8 with the particle size distributions found in the insets; (e) XRD patterns of CDs to evaluate their degree of crystallinity; HR-XPS of the C 1s spectrum for (f) CD-1, (g) CD-2, (h) CD-4 and (i) CD-8 illustrating the presence of C-N, C-O/C=O and C-C/C=C bonds (HR-XPS spectra for O1s, N1s and S2p are found in the Supporting Information); (j) FTIR spectra of the CDs showcasing the similarities in their surface functional groups; (k) Raman spectra of the CDs illustrating the increase in D/G bands ratio with increasing reaction times suggesting the growth of the aromatic core

is confirmed by the appearance of a crystalline reflection centered at 27.3º 2θ ascribed to the (100) diffraction plane of graphitic structures. These findings indicate that longer reaction times lead to

an increasing in the polymerization level of the CDs, with the formation of more organized structures.

Further investigation into the composition and nature of the chemical bonds of the CDs were performed using XPS analysis. The survey scan (**Figure S2.2**) confirms the presence of four peaks centered at 531 eV, 400 eV, 285 eV and 164 eV ascribed to the binding energies of O1s, N1s, C1s and S2p respectively. The deconvolution of the high-resolution XPS spectra (HR-XPS) of C1s for the four CD samples (**Figure 2.2**f-i) reveal binding energies ascribed to C-N (287.5 eV), C-O/C=O (285.9 eV) and C-C/C=C (284.6 eV) functional groups. The samples synthesized from 1 to 4h present similar photoelectron spectra, however a slight increase in the C-O/C=O peak is observed with an increasing reaction time suggesting amide bond formation. The sample synthesized at 8h, however, presents a major increase in the C-N and C=N peaks. This is attributed to the increase in the carbonization process occurring with longer reaction times. Initially, precursors form highly fluorescent molecules and as the reaction progresses, the starting material and the fluorophores further carbonize to form the carbogenic core.[118] The HR-XPS for O1s (**Figure S2.3**) showed the presence of C=O (532.2 eV) and C-O/C-OH (531.0 eV) functional groups for all CDs. An increase in the C-O/C=O peaks is observed from 1 to 4h. However, at 8h, most of the oxygen is present under the form of C=O. The HR-XPS for N1s (**Figure S2.4**) indicated the presence of pyrrolic (399.6 eV) and pyridinic (398.17 eV) moieties. With the increasing reaction time, an increase in the peak of the pyridinic nitrogen is observed, indicating the formation of a larger aromatic domain. Lastly, the HR-XPS for S2p showed the presence of S=O (167.9 eV), thiols (164.5 eV), and thiophenes (163.3 and 167.1 eV). With the increasing reaction time, the S=O species are further oxidized, giving rise to SO_x species.

We further investigated the surface chemistry of the dots, with increasing reaction times, *via* FTIR (**Figure 2.2**j). In conformity to the XPS results, a broad band ranging from 3500-3000 cm^{-1} was observed and is associated with the symmetric and asymmetric stretching modes of the N-H and -OH groups. The stretching modes of the C=O (1671 cm^{-1}) from the amide groups, C-OH (1596 cm^{-1}) and C-N (1384 cm^{-1}) moieties are also present. As observed in the XPS analysis, an increase in the intensity of the bands associated with the C-N bonds is observed with the increasing reaction time. The FTIR spectra for all four samples present similar profiles, and no major changes were observed with the increasing reaction time. This suggests that the major changes occur in the core

of the CDs and that the surface remains relatively intact. The effect of carbonization of the CDs with increasing reaction time was also monitored through Raman spectroscopy analysis. The spectra characteristic to the D and G bands (1344 and 1525 cm^{-1}) are shown in **Figure 2.2**k for all the dots studied. The D band refers to the defects (and structural disorder) while the G counterpart refers to the graphitic order.[108] The core of the CDs comprises sp^2 clusters, which is largely responsible for the signal of the G band.[108, 119, 120] It is noted that the I_D/I_G (intensity band ratio) decreases with increasing reaction time (from 1.19 for CD-1 down to 0.77 for CD-8) induced by the growth of the aromatic domain and the graphitization of the carbon-core of the CDs.[121]

2.3.2. Steady-State Optical Properties Characterization

As shown in **Figure 2.3**a, the UV-Vis absorption spectra of the samples display three analogous prominent bands at 320 nm, 400 nm and 580-700 nm. The first band is assigned to the transition of the C=C bonds of the carbon-core, while the second and third bands are ascribed to the $\pi \rightarrow \pi^*$ and $n \rightarrow \pi^*$ transitions of the aromatic sp^2 domains for the C=O and C=S/C=N, respectively.[70, 113, 116] The overall absorbance decreases with increasing reaction times; it is noted that the absorbance band intensities at 580-700 nm decrease at a faster rate than those in the lower regions of the spectrum. The multiple absorption bands emanate from different emissive states; the first state being the carbon-core state comprising primarily an sp^2 carbon network, while the second corresponds to the molecular states, which are dictated by fluorescent molecules that are bound to the surface of the CDs.[119] As shown by XRD and XPS, an increase in reaction time further causes carbonization and aromatization. This in turn leads to the formation of larger sp^2 networks (resulting in a larger carbon core; discussed in the XRD and XPS data) to the detriment of molecular fluorophores.[86, 105, 122] As such, a decrease in absorption at longer wavelengths is observed.

The steady-state fluorescence spectra showcase signatures in both the blue and red regions of the spectrum for all the samples, which further implies the possibility of two fluorescence centers. The blue fluorescence component is noted to be excitation dependent, while the red fluorescence is excitation independent (λ_{ex} = 680 nm); these are attributed to the carbon-core and molecular states,

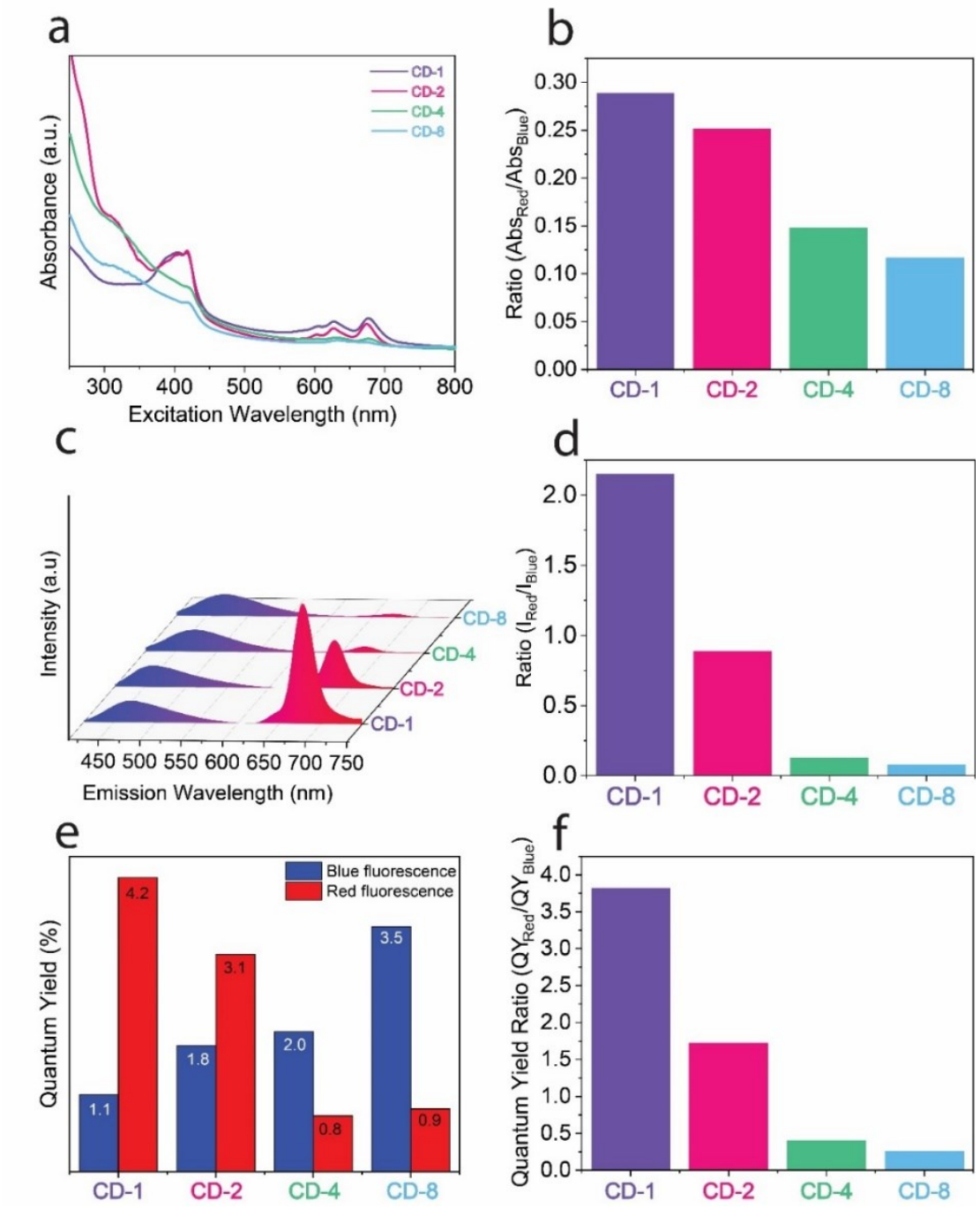

Figure 2.3 UV-Vis absorbance and fluorescence spectra, and quantum yield of 50 μg mL^{-1} CD dispersion; (a) UV-Vis absorption spectra of the CDs show three absorption bands centered at 320 nm, 420 nm and 580-700 nm; (c) Following excitation at 420 nm, two fluorescence bands are observed at 350-550 nm (blue fluorescence) and 650-750 nm (red fluorescence); (e) Quantum yield measurements of the blue and red fluorescence at an excitation wavelength of 420 nm. (b) The absorbance, (d) the fluorescence and (f) the quantum yield show a similar trend in which the signal of the red region of the spectra decreases relative to that in the blue.

respectively.[60] As shown in the photoluminescence excitation (PLE) spectra for both the blue and red fluorescence components for CD-1 (**Figure S2.5**a), a broad range of wavelengths can be used to excite these states. In addition, depending on the wavelength used to excite the dot, different states are probed resulting in differences in the overall fluorescence contributions by the two states (**Figure S2.5**b for CD-1). Essentially, both the carbon-core and the molecular states are excited simultaneously with short wavelength excitation. The shorter the excitation wavelength, the stronger the blue component relative to its red counterpart. On the contrary, with longer excitation wavelengths, the red fluorescence dominates. This suggests that the surface states are primarily excited by longer wavelengths due to their lower bandgap.

As shown in **Figure 2.3**c, with varying reaction times, both fluorescence peaks show no changes in spectral shape. It is noted that there is a change in intensity of the blue and red fluorescence components, which is indicative of the variations in accessible emissive centers. The relative fluorescence intensity of red-to-blue is at its maximum for CD-1 and decreases with increasing reaction times (**Figure 2.3**d). A similar trend is observed in the fluorescence quantum yield (QY, **Figure 2.3**e-f) with QYs of 5.3 %, 4.9 %, 2.8 % and 4.4 % for CD-1, CD-2, CD-4 and CD-8, respectively. Upon closer inspection of the QYs, the blue fluorescence gradually increases from 1.1 up to 3.5 %; inversely, its red counterpart decreases from 4.2 to 0.9 %. This observation is attributed to the carbonization of the molecules linked to the CDs, which are responsible for the molecular states (red fluorescence) at the expense of the growth of the sp^2 network in the core of the CD, which in turn is responsible for the core states (blue fluorescence). Therefore, an increase of quantum yield at CD-8 is observed and expected because of its much larger core.

The existence of both states was verified *via* photobleaching experiments. The photostability profile for CDs can be associated with the presence of different emissive centers.[86] Following extended periods of UV exposure (λ_{ex}=365 nm), the red component of CD-1 decreases at a much higher rate than the blue component (**Figure S2.6**). Such behavior is expected as the blue fluorescence mainly stems from the direct electron-hole recombination in the carbon core states of the CDs. This agrees with previous reports showing that the carbon core-states typically emit at a shorter wavelength, possess better photobleaching resistance, and have a much lower fluorescence QY relative to molecular states of CDs.[52, 123] In addition, two lifetimes were identified: 4.6 ns and 0.6 ns, suggesting multiple fluorescence centers. Using a long-pass filter, which separates both

fluorescence signatures, it is postulated that the longer fluorescence lifetime stems from the relaxation of the electrons from the core, while the fast lifetime corresponds to the electron-hole recombination in the molecular states.[124]

2.3.3. Electrochemical and Transient Absorption Spectroscopy Studies

To extensively study the dynamic processes of this unique dual-fluorescent CD-system, electrochemical and ultrafast transient absorption spectroscopy studies were carried out. These investigations were limited to CD-1, as it provided the highest signal intensity for both red and blue fluorescence signatures. First, cyclic voltammetry measurements were used to estimate the HOMO/LUMO energies of CD-1 **Figure 2.4**a-b); all potentials reported were assigned against NHE. A non-reversible peak with an onset value of E_{ox} = +1.1 V was observed when the potential was swept through the oxidative side (**Figure 2.4**a). Likewise, another non-reversible wave was noted when the potential was swept through the reductive side with an onset value of E_{red} = -0.9 V. Interestingly, when comparing these values to the absorbance spectroscopy results, the HOMO-LUMO gap calculated from cyclic voltammetry (2.0 eV) is in agreement with the UV-Vis data for the red component of the CDs dispersed in water (λ_{max} = 680 nm). To calculate the HOMO and LUMO of the blue component, blue fluorescent carbon dots were synthesized in a similar fashion for 20 hours, completely removing the red fluorescence due to the excess carbonization.[113] The HOMO and LUMO were calculated to be -1.75 V and 1.2 V (**Figure 2.4**b), respectively, which amounts to a band gap of 2.95 eV in accordance with the UV-Vis data for the blue fluorescence. As shown in **Figure 2.4**c, this data suggests the possibility that the fluorescence stems from: (i) a direct electron-hole radiative recombination in each state (core and molecular) with (ii) the possibility of an energy transfer from the carbon core-state down to the molecular-state followed by a radiative recombination.

CD-1 were cast onto a transparent conductive substrate (FTO) to evaluate the photocurrent density at different excitation wavelengths through chronoamperometry in a three-electrode system with no applied bias. Three light sources were used including red (620-640 nm; λ_{max} = 630 nm), blue (455-475 nm; λ_{max} = 465 nm), and white LEDs (see white LED emission spectrum in **Figure S2.7**); where the first two targets the red fluorescent component, while the LEDs target both the blue and red together. Chopped-light illumination experiments were sequentially conducted with each light

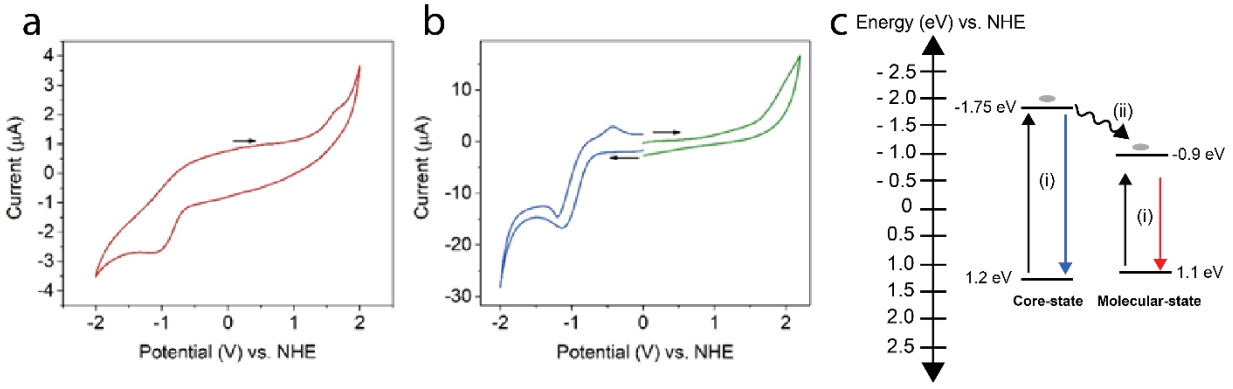

Figure 2.4 Cyclic voltammograms for the calculation of the HOMO and LUMO positions for (a) CD-1 and (b) bCDs. The redox potentials for CD-1 were calculated from both the oxidative and reductive non-reversible peaks. These values were calculated from separate scans for bCDs. The oxidative potential was computed from the oxidative onset value (green scan), while the reductive potential was calculated from the non-reversible peak (blue scan). RE: Ag wire; CE: Pt wire; WE: FTO|CD-1 film, 0.1 M TBAPF6 in acetonitrile (Scan rate: 100 mV s−1); (c) Simplified energy diagram representing the fluorescence stemming from the carbon core and molecular states. The HOMO and LUMO of both states are measured (1.2 eV and -1.75 eV for the core-state; 1.1 eV and -0.9 eV for the molecular state). Fluorescence stems from two possible pathways: (i) direct electron-hole radiative recombination and (ii) energy transfer of an excited electron in the core state to the molecular state followed by a radiative recombination.

source cycling from white to red to blue for two cycles in a 0.1 M solution of $TBAPF_6$ with no sacrificial agents (**Figure S2.8**). Upon irradiation, a current increase from the electron injection into the FTO was observed with a charging signature due to the build-up of charges at the solid-liquid interface. The current densities for all the chopped-light experiments were calculated and are shown **Table S2.1**. In addition, the integration of the absorption portion that is targeted by each LED was tabulated (**Table S2.2**) and compared to the current densities to correlate the density of states with the current output upon light irradiation. As expected, irradiation of the electrode with white light yields the highest current density since it can excite both the red and blue components of the dots (**Figure S2.7**). The integration of the targeted absorption region for this excitation is also the highest. Interestingly, the red excitation yields the lowest current density even if the integration for the absorption has a considerably high value. This result possibly suggests that electrons responsible for the red fluorescence might populate the red excited state after a non-radiative electron transfer from the blue excited state (LUMO-LUMO transition), which would account for the high emission intensity for the red state compared to the blue when the sample is excited at 420 nm (**Figure 2.3**c and **Figure S2.5**). This electron transfer to the red state (or molecular state) can increase the current density observed in the chronoamperogram which is what

is observed when the CDs are irradiated use blue excitation wavelengths; this current density was almost comparable to that of the white excitation. Moreover, such behavior may point to the possibility that both emission signatures originate from the same ground state located at the core of the CD, which is possible based on the similar calculated LUMOs.

Transient absorption spectroscopy (TAS) analyses were carried out to understand the dynamics of the electronic processes governing the optical properties of the CDs. The CDs were dispersed in Milli-Q water and the samples were excited at 620, 425 and 310 nm. Studies following excitation at 620 nm (**Figure 2.5**a-c) investigate and isolate the electronic transitions for the red activity (RA; responsible for the fluorescence at 680 nm). Conversely, excitation at 310 nm (**Figure 2.5**d-f) provides information on the blue activity (BA; responsible for the fluorescence centered around 475 nm). It is noted that CD-8 showed a very weak signal preventing its analysis while the signal obtained from CD-4 was very weak in intensity owing to its low absorbance. The TA spectra are compared to the steady state absorbance (**Figure 2.5**g-i), fluorescence (**Figure 2.3**c) and PLE spectra (**Figure S2.5**), which enables the assignment of peaks to the following spectral features: (i) a negative ground state bleaching (GSB) due to a depopulation of the ground state following the pump absorption, which aligns with the peaks of the inverted absorption spectra; (ii) a negative stimulated emission (SE), where the shape would match the inverted fluorescence signal; (iii) a positive excited state absorption (ESA) due to transitions to higher energy levels. The spectra for CD-1, CD-2 and CD-4 share similarities in terms of their features with few changes in their overall signal. When studying the TAS spectra at 620 nm for the CDs (**Figure 2.5**a-c), the spectra at the shortest observable time delays resemble closely to the inverted absorbance spectra with negative features (GSB) aligning with PLE at 680 nm. This confirms that these absorption bands share the same ground state, originating from the same chromophore, and are the transitions to the first and second electronic excited states, leading to the red fluorescence at 680 nm.

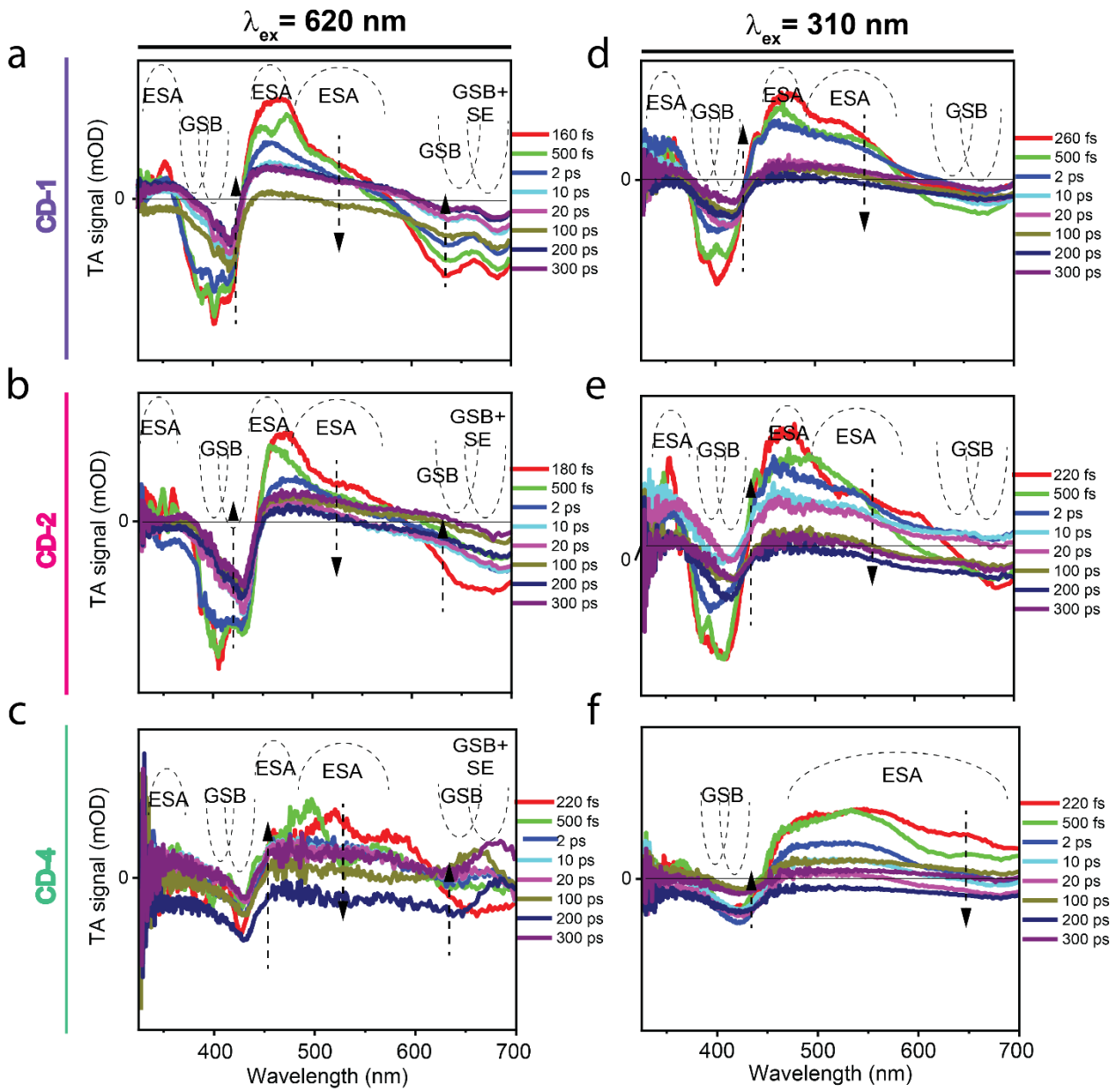

Figure 2.5 Transient absorption (TA) spectra at selected delays of the CD-1, CD-2 and CD-4 (a-c) at λ_{ex} = 620 nm and (d-f) λ_{ex} = 310 nm. The grey lines are guidelines to identify the different contributions to the TA signals: excited state absorption (ESA), ground state bleaching (GSB) and stimulated emission (SE). It's noted that the ESA contributions are always positive, while GSB and SE provide negative signals. The inverted absorbance spectra of the respective CDs are plotted in black (dashed); the inverted PLE for the PL at 475 nm and 680 nm are plotted in blue and in red, respectively.

Within 10 ps, a prominent change in line-shape occurs, with a decay of a band centred at 390 nm, as well as a change in the GSB ratios at 640 and 690 nm (with the former decreasing faster than

the latter) and the excited state absorption (ESA) at 450 nm disappears. The remaining signal is long-lived with ground state recovery in the ns timescale. This behavior is present in each sample (**Figure 2.5**a-c), which points towards the presence of two RA relaxation processes, each occurring at different timescales: (i) The first mechanism takes place in the order of a few ps and can be described by the decay of GSB at 390 nm and 640 nm, accompanied by the decay of the ESA at 450 nm and (ii) the second mechanism, responsible for the red steady-state emission, is slower (the decay occurs in the ns range) and is assigned to the remaining ground state recovery signal, characterized by a GSB at 410 nm with a distinctive triangular shape and the SE at 680 nm. These results imply the presence of structural heterogeneity in the dots with multiple RA relaxation processes, involving different radiative and non-radiative channels.

TAS experiments at 425 nm (**Figure S2.9**) are consistent with the findings presented upon excitation at 620 nm. The overall signal and its evolution illustrates the slow decaying RA with a small contribution from the fast decaying RA, as would be expected from the excitation of the absorbance band presenting the higher quantum yield. A small SE rise at 680 nm for CD-1 and CD-2 can be observed at a short time scale of 140 to 460 fs (**Figure S2.9**a-b). This is indicative of an ultrafast internal conversion from a higher excited state populating the lower excited states responsible for the red fluorescence (typical time scales for internal conversion are found around 100 fs).[125]

Time-resolved spectra following 310 nm excitation highlight transitions relating to the blue optical activity (**Figure 2.5**d-f). We do note that the red component is still partially excited, based on the PLE in **Figure S2.5**, preventing completely isolated studies of the blue counterpart. The main dynamics of the spectra at this excitation wavelength shares similarities with the features observed using 620 nm excitation with some key differences: (i) The spectra at the shortest observable time delays are similar to the inverted absorbance spectra in the region between 350 nm to 600 nm; (ii) a damping of the 450 nm ESA peak can be observed compared to that obtained at 620 nm excitation. This is assigned to the blue fluorescence, which is dominated by ESA; (iii) the GSB band at 620-640 nm exhibits a very weak signal, and GSB at 680 nm is much smaller relative to the GSB at 400 nm when compared to the experiment at 620 nm (**Figure 2.5**a-c). Interestingly, a small rise of the signal up to 500 fs is observed, which suggests that there is still excitation of the red fluorescence (similar analyses at 425 nm). It cannot be conclusively discriminated here if, upon

310 nm excitation, the red activity is directly or indirectly populated from the energy states responsible for the blue activity. This is due to a lack of evident signs of an energy transfer, apart from a small SE rise at 680 nm in the first 100s fs, which in turn could stem from the excitation of the red activity at higher energies. In the dynamics, we observe two mechanisms relating to RA: (i) a fast recovery at ps range, with the decay of GSB bands at 400 nm and 640 nm, accompanied by the decay of the ESA at 450 nm and (ii) a ground state recovery in the ns timescale. Interestingly, a major difference in the initial spectra is observed for the CD-4 sample (illustrated in **Figure 2.5**f), where the presence of a broad ESA between 450 nm to 700 nm points to the excitation of electronic states in the molecular conduction band, consistent with the increase of the core crystalline structure. This evidence combined with the differences in the GSB could suggest the excitation of a transition with a different ground state with respect to the RA, with different initial and final excited states.

2.3.4. Conclusion

To date, the fluorescence mechanism of CDs remains a topic of discussion. As such, there remains an urgent need to generate novel and additional insights through various experimental studies to further our knowledge relating to this phenomenon. In this work, we synthesized a series of CDs using glutathione and formamide, *via* a solvothermal reaction at varying reaction times. It is observed that these dots showcase a unique dual-fluorescence behavior where they fluoresce in both the blue and red regions of the spectrum. The underlying mechanism of this dual-fluorescence phenomenon was investigated through extensive studies using steady-state and time-resolved fluorescence techniques. Our experimental results suggest that two fluorescence states are present: carbon-core and molecular states. The former stems from sp^2 carbon network, while the latter originates from fluorophore-like moieties. The dual-fluorescence signature of these CDs is attributed to the two states. Interestingly, it's demonstrated that further carbonizing the dot (i.e. increasing the reaction time) promotes a notable growth of the carbon-core sp^2 network through the consumption of the molecular fluorophores. Our results promote better understanding of dual fluorescent carbon dots and our iterative approach using synthesis and characterization offers novel insights in design of carbon dots and tailoring their physico-optical properties.

2.3.5. Experimental Section

Chemicals and reagents - Formamide (≥99.5%) and reduced L-glutathione (≥98.0%) were purchased from Thermo Scientific. All reagents were used without further modification or purification.

Synthesis of Carbon Dots (CDs) - The CDs were synthesized *via* a hydrothermal-mediated reaction with glutathione and formamide. For each CD sample prepared at different times, a 20 mL solution of 0.1M glutathione in formamide was prepared. The mixture was sonicated for 10 min until the it changed from a cloudy to a clear homogeneous solution. The solution was transferred to a Teflon lined container and placed inside a hydrothermal reactor. The reactor was heated at 180°C at varying reaction times (1, 2, 4, 8 hours). Once cooled, the dispersion was purified to remove excess unreacted materials and fluorophores *via* dialysis using a cellulose ester dialysis membrane (molecular weight cut-off = 3.5 – 5.0 kDa). The dialysis lasted for 5 days with water being replaced twice a day. Following this step, the sample was concentrated down *via* rotovapping and the remaining impurities were washed twice with acetone and ethanol (1:10, sample:solvent volume ratio; 10 min centrifugation at 10 000 x g). The precipitate was collected after each wash. The final product was then dried in the oven at 70°C overnight.

Transmission Electron Microscopy - CDs were dispersed in water at a concentration of 5.0 mg/mL. Grids were prepared by pipetting 2 μL of the CD dispersion on a 300 Mesh Cu (Cu-300HD) coated with holey/thin carbon films (Grid-Tech) followed by evaporation of the solvent. The TEM images were collected using a LVEM5 benchtop electron microscope operating at 5 kV. Images were processed and the carbon dot sizes were determined using Fiji imaging software.

UV-Vis Absorbance - UV-visible absorption spectra were acquired from 200-800 nm on a Cary 5 Series UV-Vis-NIR Spectrophotometer (Agilent Technologies) using a 1 cm quartz cuvette. A 5.0 nm bandwidth and wavelength changeover at 450 nm were used for analysis. Data was processed using Cary Eclipse software.

Quantum Yield Measurements - Quantum yield values were acquired on an FLS920 Fluorescence Spectrometer (Edinburgh Instruments) with an integrating sphere using a 1 cm quartz

cuvette. The excitation and the emission slits were set to a width of 5 nm and The excitation wavelength was set to 405 nm; the spectra from 300-800 nm were collected. Scans were done in triplicates with a dwell time of 0.25 sec. Data was processed using F900 Software.

Fluorescence Spectroscopy - Fluorescence spectra were acquired using a Cary Eclipse fluorescence spectrophotometer (Agilent Technologies). Spectra were acquired in a 1-cm quartz cuvette at λ_{ex} = 405 nm. The excitation and emission slits were set to a width of 5 nm with a PMT voltage at 600 V. All data were processed using Cary Eclipse software.

Fourier-Transform Infrared Spectroscopy - Fourier-Transform Infrared Spectroscopy (FT-IR) spectra were collected using a Thermo Scientific Nicolet iS5 equipped with an iD5 ATR accessory. Spectra were collected using 30 scans with a resolution of 0.4 cm^{-1}, a gain of 1, an optical velocity 0.4747 and an aperture setting of 100. Data was processed using Omnic 9 software.

X-ray Photoelectron Spectroscopy (XPS) - A Thermo Scientific K-Alpha X-Ray Photoelectron Spectrometer was used to obtain the XPS spectra of the dCDs. Each analysis was carried out in triplicate with 10 runs for each scan and the averages were plotted for both the survey and high-resolution scans.

Electrochemical Analysis - Electrochemical measurements were performed using a WaveDriver 200 Integrated Bipotentiostat/Galvanostat workstation. A three-electrode system was used to analyze the photoelectrochemical response of the different CDs with an FTO substrate as a working electrode (WE), a platinum wire as a counter electrode (CE), and a Ag wire as a reference electrode in a 0.1 M tetrabutylammonium hexafluorophosphate ($TBAPF_6$) electrolyte solution. All potentials were measured against the reference electrode. The films of CDs on the FTO were illuminated by four white LEDs at a 5 cm distance from the film. The electrochemical properties of the CDs were determined using a three-electrode system by drop casting the CDs on a 1 mm button platinum WE, a platinum wire as a CE, and a Ag wire pseudo-reference electrode in a 0.1 M $TBAPF_6$ solution. All potentials were calibrated against ferrocene as an internal standard.

Time Resolved Femtosecond Transient Absorption Setup - TA experiments were carried out upon excitation at 620 nm, 425 nm and 310 nm. The 620 nm, linearly polarized, pump beam was generated from a non-collinear parametric amplifier (TopasWhite, by Light Conversion), pumped with 800 nm pulses from a 5 kHz Ti:Sapphire fs regenerative amplifier (Coherent Legend). The laser source provided 130 fs full width half maximum (FWHM) pulses focused into a ~60 μm diameter spot ($1/e^2$). The energy per pulse was set to 60 nJ. 425 nm and 310 nm linearly polarized pump beams were generated by frequency doubling in a b-BBO 850 nm and 620 nm beams, respectively, from a non-collinear parametric amplifier (TopasWhite, by Light Conversion), pumped with 800 nm pulses from a 5 kHz Ti:Sapphire fs regenerative amplifier (Coherent Legend). These beams consisted of 90 fs (FWHM) pulses and were focused into ~60 μm diameter spot ($1/e^2$) with energy per pulse of 90 nJ. The probe was a white-light continuum generated by focusing a small fraction of the 800 nm Ti:sapphire laser output to a 5 mm thick CaF_2 plate. The probe spot at the sample position was ~40 μm diameter ($1/e^2$). Pump and probe beams were spatially overlapped at the sample position and the pump delay *t* with respect to the probe was controlled by a motorized delay stage. The pump and probe polarization was set to parallel. The probe beam was dispersed after the sample with a prism and detected by a 512 pixel CCD camera (Hamamatsu S11105 Series) capable of measuring single-shots. A reference baseline for the pump/reference ratio was recorded for each measurement by introducing a mechanical chopper in the pump beamline at half the repetition rate to block every other pump pulse. A photo-diode after the chopper monitored the shot-to-shot pulse intensity in order to sort "pumped" and "unpumped" measurements and to compensate for fluctuations and drifts of the pump pulse intensity. To avoid photo-degradation, the sample solutions were flowed with a micro gear pump through an UV-grade quartz flow cell with an internal path length of 200 μm. Special care was taken to measure in linear regime in terms of pump and probe intensity and sample concentration. Typical signals were obtained by averaging 500 pumped and 500 unpumped spectra for each time delay and scanning over the pump-probe delay 5-10 times. Steady-state UV-visible absorption spectra measured before and after TA measurements showed no changes, indicating the remarkable photo-stability of the investigated complexes.

2.4. Supplementary Information

Figure S2.1 Colloidal dispersions of CD-1, CD-2, CD-4 and CD-8 (left to right) representing 1, 2, 4 and 8-hour reaction times, respectively. The colour of the carbon dot dispersion changes from green to brown suggesting an increase in carbonization with increasing synthesis time.

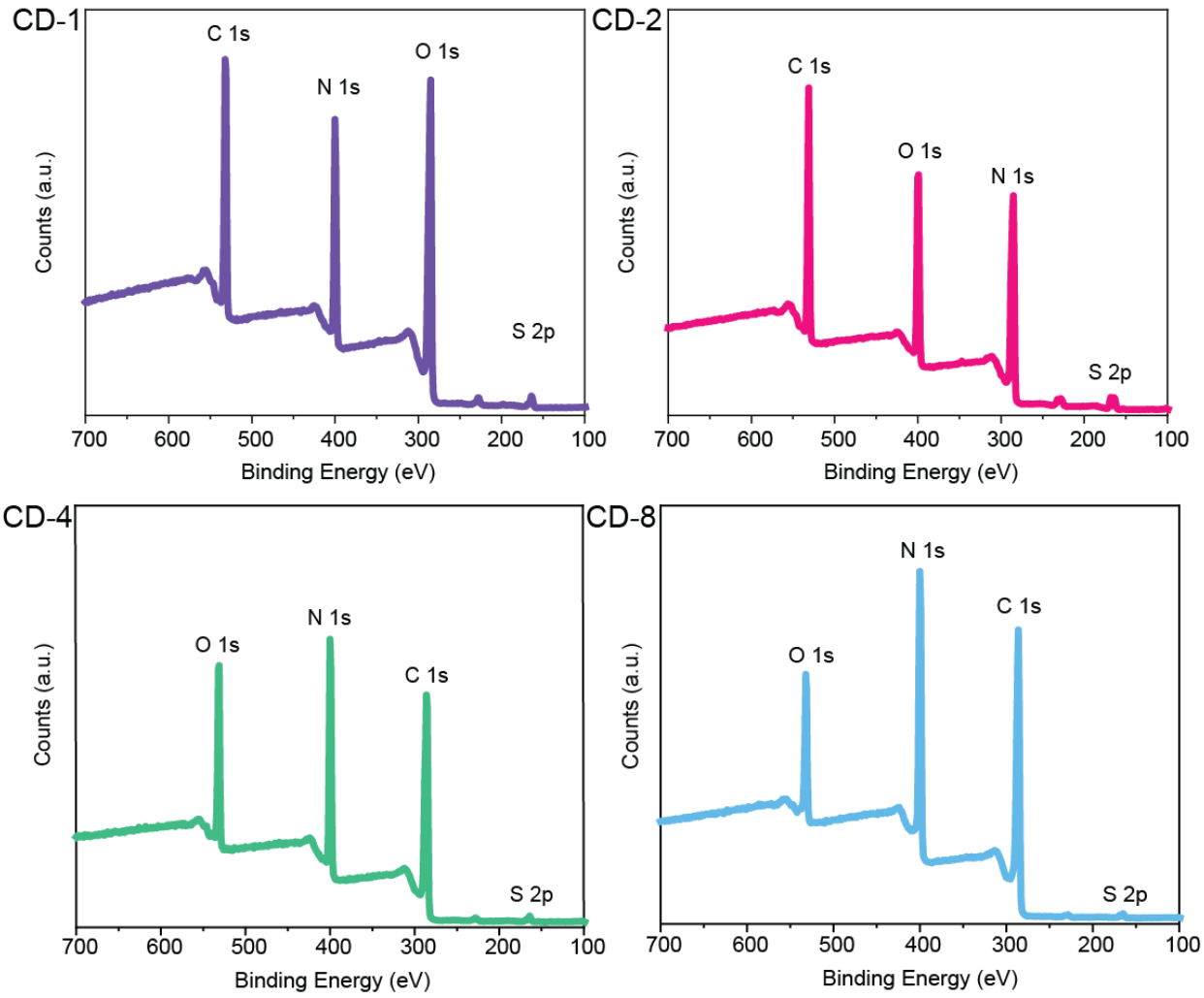

Figure S2.2 XPS survey spectra for the CDs. The spectra reveals the presence of O, N, C and S with peaks centered at 531 eV, 400 eV, 285 eV and 164 eV, which are assigned to O1s, N1s, C1s and S2p.

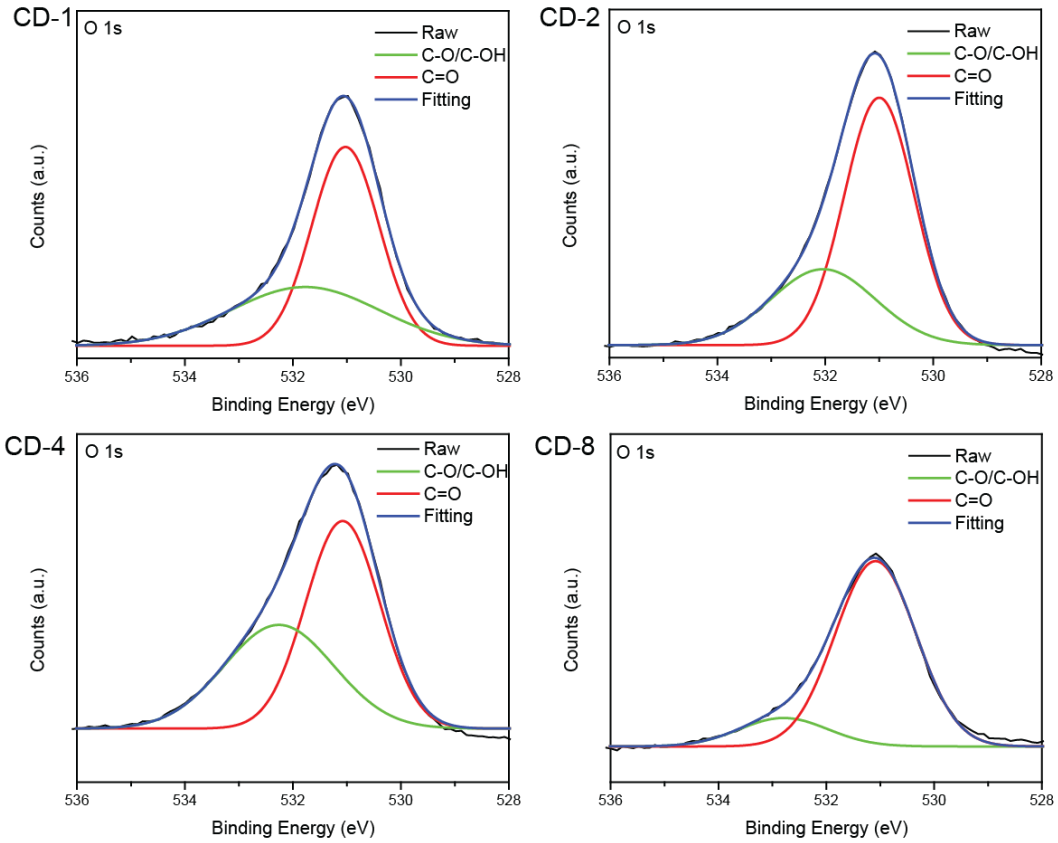

Figure S2.3 HR-XPS for O1s for all CDs. The presence of C=O (532.2 eV) and C-O/C-OH (531.0 eV) functional groups are showcased. An increase in the C-O/C-OH relative to C=O is observed up to 4 hours of reaction time (CD-4), followed by a decrease at 8 hours (CD-8)s.

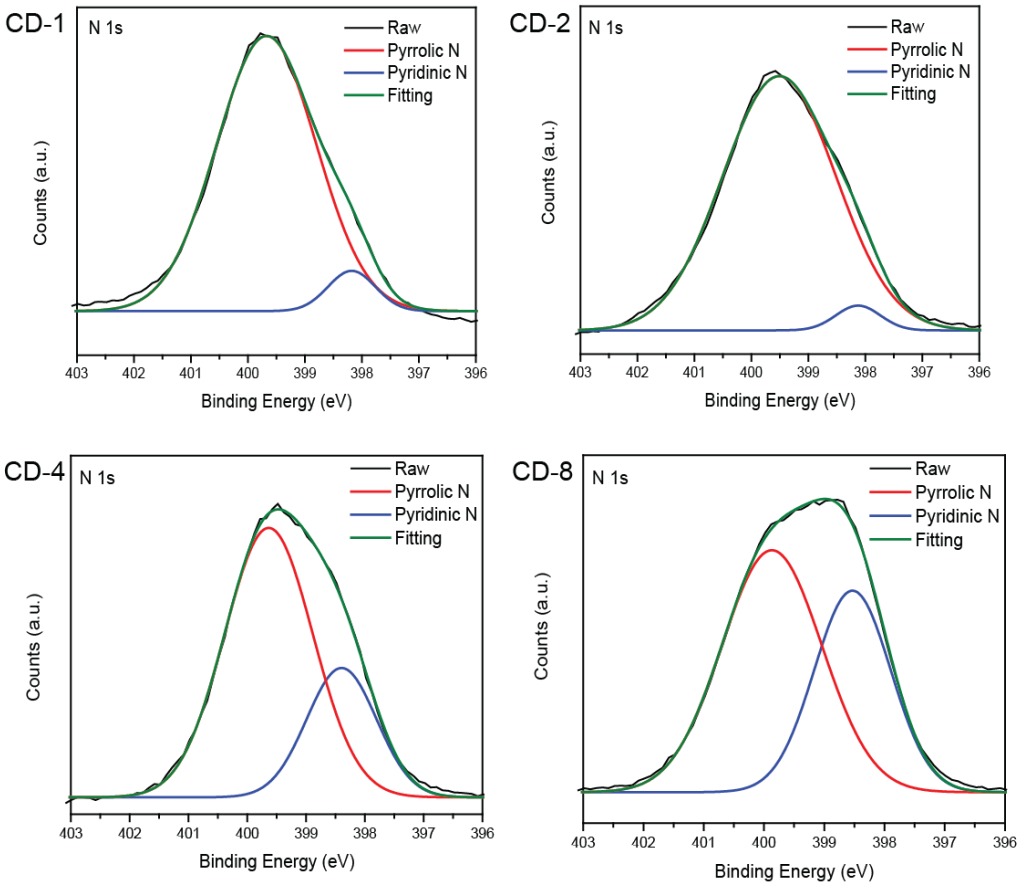

Figure S2.4 HR-XPS for N1s for all CDs. The spectra show the presence of pyrrolic (399.6 eV) and pyridinic (398.17 eV) moieties. It's noted that with increasing reaction time results in an increase of pyridinic nitrogen.

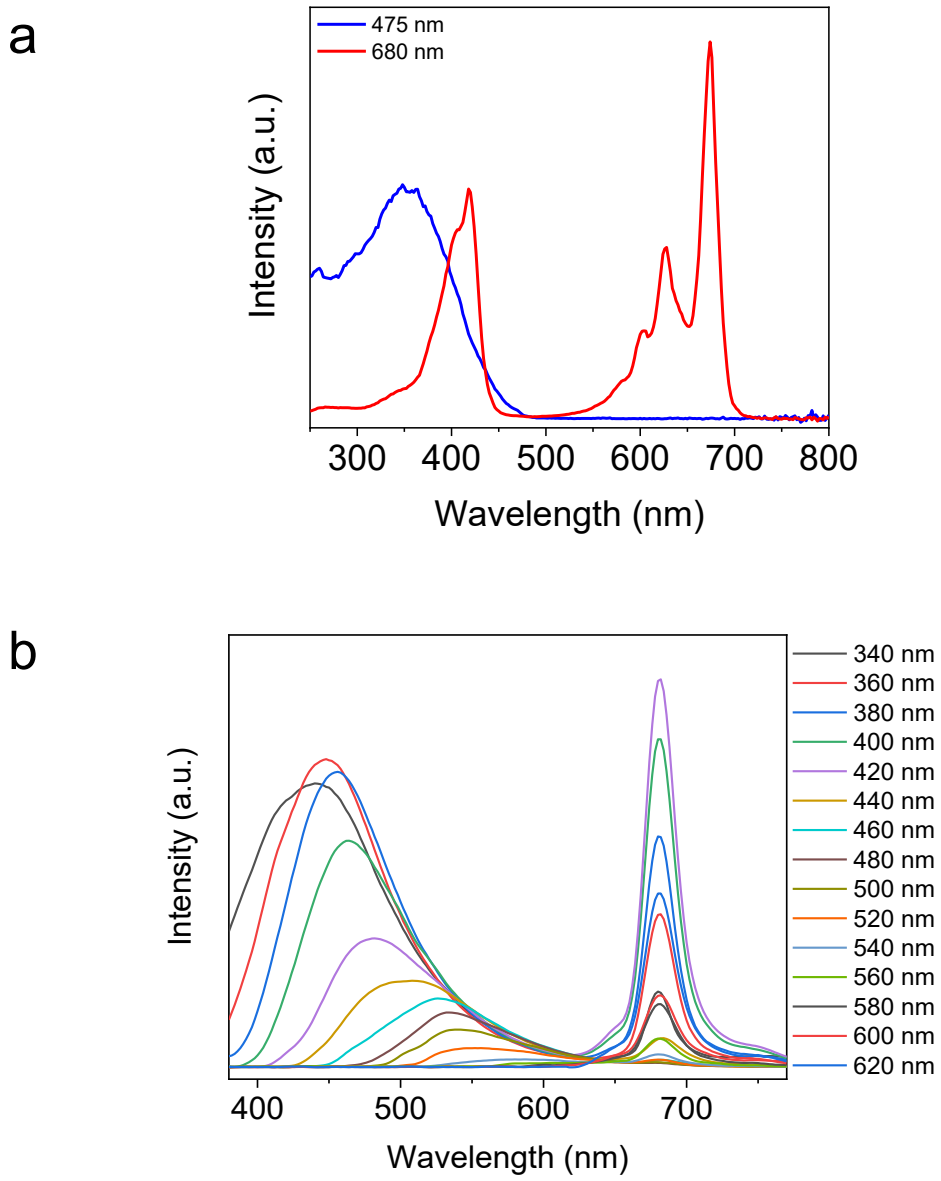

Figure S2.5 (a) PLE spectra of CD-1. The spectrum in blue illustrates the absorbance profile of the blue fluorescence component whereas the red spectrum shows the absorbance profile of the red component; (b) Fluorescence spectra of CD-1 at various excitation wavelengths highlighting the excitation dependence and independence of the blue and red fluorescence, respectively. It also showcases the changes in intensity of the red and blue fluorescence with an increase in excitation wavelength.

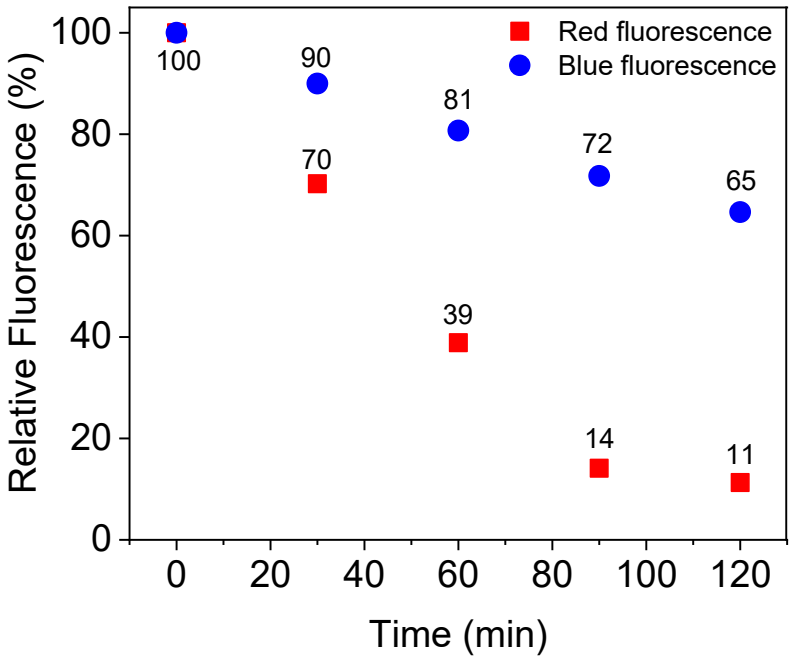

Figure S2.6 Photobleaching experiment with CD-1. Following an extended exposure to UV light, the fluorescence intensity of the red component of the CDs decreases at a much higher rate than the blue counterpart. Such behavior is expected as the blue fluorescence stems from the direct electron-hole recombination in the carbon core states of the dots, which are more photostable than the molecular states ascribed to the origins of the red fluorescence.

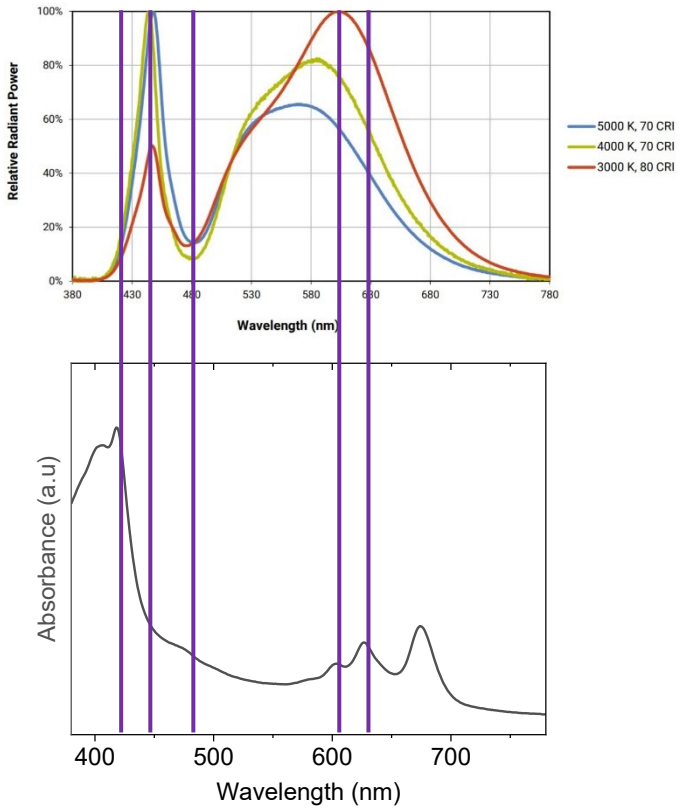

Figure S2.7 The emission profile for the white LEDs is matched to the absorbance spectra of CD-1. The blue component of the LEDs targets the blue absorption of the CDs, while the red component aligns with the red absorption.

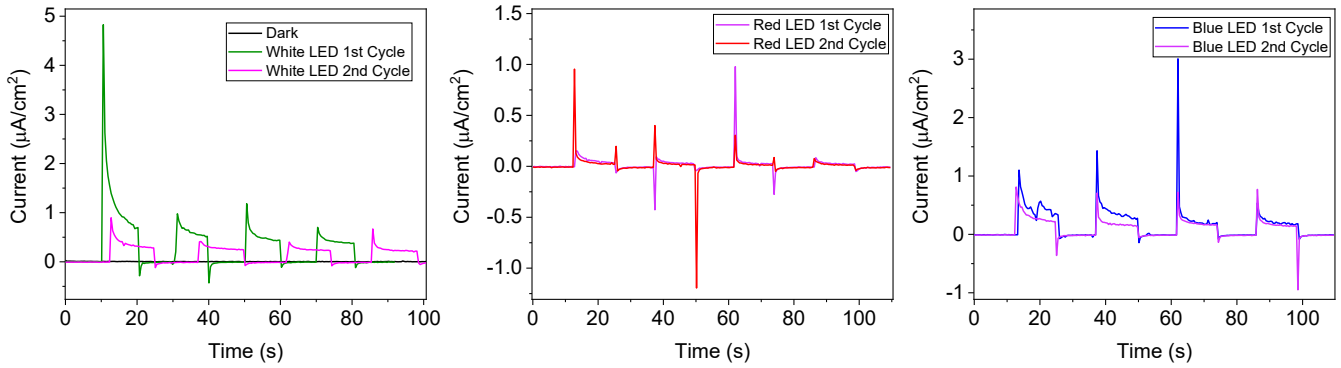

Figure S2.8 Chopped-light chronoamperometry experiments for the CD-1 dots casted on an FTO film under different LED illumination ((a) white light, (b) red light and (c) blue light). Irradiation with white LEDs yields the highest photocurrent densities since both the red and blue components are excited simultaneously. The blue illumination produces significant current densities since the electron-rich core of the CDs is being excited. Conversely, the red illumination generates extremely low photocurrents since it targets the surface groups containing more trap states.

Table S2.1 Current densities for each light-on/light-off interval. The first and second cycles of irradiations were normalized to the first and second white LED cycles, respectively.

INTERVAL	WHITE 1ST CYCLE	RED 1ST CYCLE	BLUE 1ST CYCLE	WHITE 2ND CYCLE	RED 2ND CYCLE	BLUE 2ND CYCLE
1	100.0	6.9	42.8	100	15.9	82.3
2	62.0	5.5	33.0	83.0	13.1	51.2
3	49.5	5.0	20.4	76.5	12.4	55.1
4	41.7	4.8	19.4	71.7	12.0	48.9

Table S2.2 Integration for the absorption regions targeted by each LED. The white LEDs target portions in the red and blue regions of the spectrum as shown in Figure S2.8.

LED	Integration
White (565-700 nm) – (465-485 nm)	25.8
Red (600-620 nm)	14.9
Blue (465-485 nm)	7.7

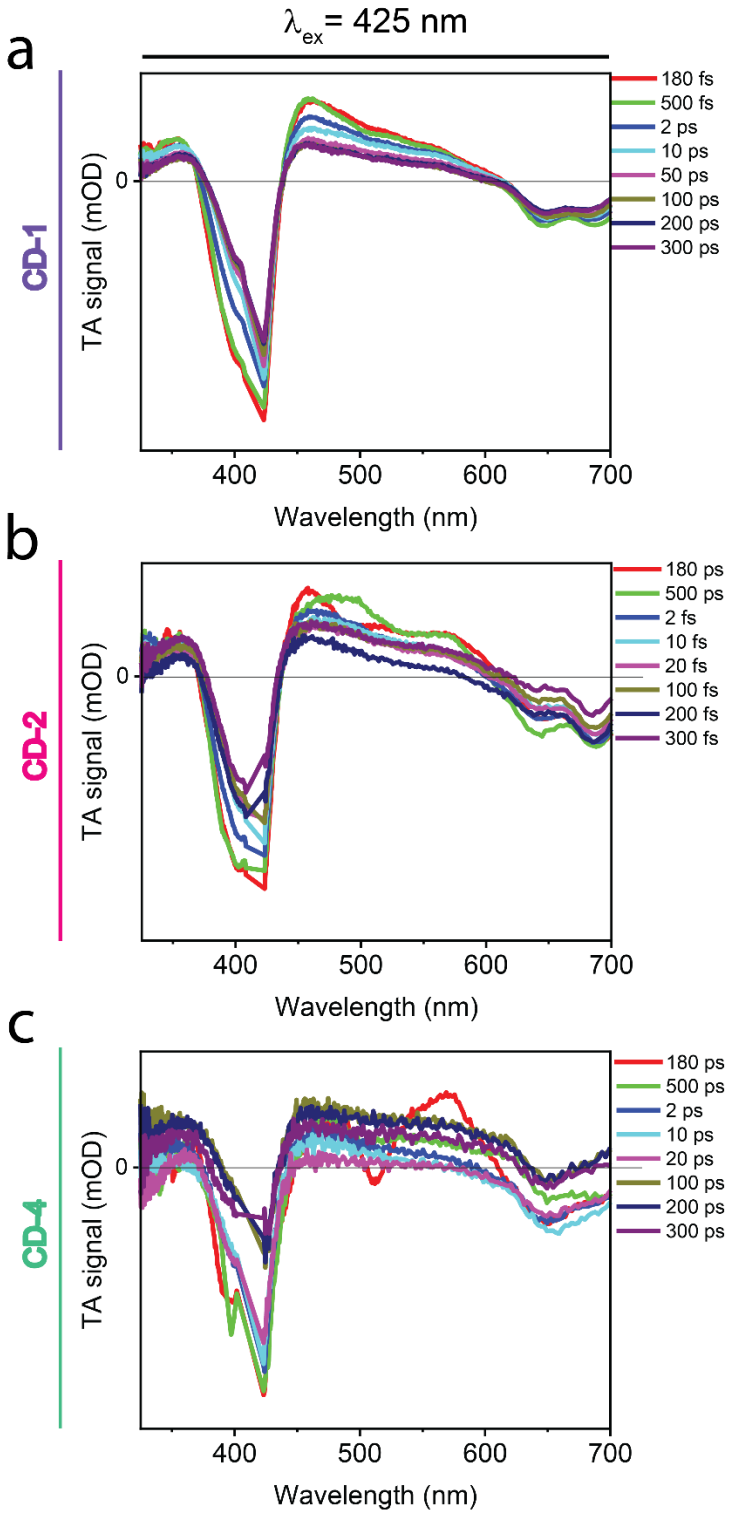

Figure S2.9 Transient absorption spectra at selected delay times for (a) CD-1, (b) CD-2 and CD-4 following excitation at 425 nm. A GSB signal at 410 nm with a sharp peak is observed. It is noted that this wavelength mainly triggers the emissive red component, while the fast decaying non-emissive red component provides little contribution in the transient.

Chapter 3. Intracellular Ratiometric Temperature Sensing Using Fluorescent Carbon Dots

3.1. Abstract

Highly sensitive non-invasive temperature sensing is critical for studying fundamental biological processes and applications in medical diagnostics. Nanoscale-based thermometers are promising non-invasive probes for precise temperature sensing with subcellular resolution. However, many of these systems have limitations as they rely on fluorescence intensity changes, deconvolution of peaks, or the use of hybrid systems to measure thermal events. To address this, we developed a fluorescence-based ratiometric temperature sensing approach using carbon dots prepared *via* microwave synthesis. These dots possess dual fluorescence signatures in the blue and red regions of the spectrum. We observed a linear response as a function of temperature in the range of 5 – 60 °C with a thermal resolution of 0.048 K^{-1} and thermal sensitivity of 1.97% C^{-1}. Temperature-dependent fluorescence was also observed in HeLa cancer cells over a range of 32-42 °C by monitoring changes in the red-to-blue fluorescence signatures. We demonstrate that the ratiometric approach is superior to intensity-based thermal sensing because it is independent of intracellular concentration. These findings suggest that dual-emitting carbon dots can be an effective tool for *in vitro* and possibly *in vivo* fluorescence nanothermometry

3.2. Introduction

Temperature plays a vital role in many biological processes. Obtaining precise temperature readings in living matter with high accuracy and specificity are crucial for fundamental cell studies, as well as for the development of novel diagnostic tools in nanomedicine.[126-130] More recently, advancements in the field of nanotechnology have led to the development of nanothermometers, *i.e.* novel temperature sensors with high spatial resolution at the nanoscale. Such nanothermometers have been developed using different platforms ranging from fluorescent proteins to upconverting nanoparticles and quantum dots.[129-136] Although still in the early stages of development, these luminescent nanomaterials have significant promise in temperature sensing and thermal mapping to grasp a better understanding of biological processes.[128-130, 137] The majority of reports concerning luminescent nanomaterials have focused on *in vitro* studies aimed at detecting the local temperature in a biological system at high resolution.[130, 133, 138-140] This may

potentially translate *in vivo* and could be useful as a diagnostic tool to detect inflammation and disease (*e.g.* cancer).[141, 142] Moreover, they could be used in synergy with other nanomaterials such as those studied for the development of novel hyperthermia treatments.[128, 130] In this case, combining thermal sensing with localized heating of the diseased area would minimize damage associated with overheating of the surrounding healthy tissue.[142-144]

Thermal sensing using nanomaterials can be accomplished by exploiting their optical properties. Fluorescence nanothermometry can be categorized into several classes depending on the specific parameter from which the thermal measurement is extracted including signal intensity, band-shape, fluorescence lifetimes, band-shift, excitation wavelength polarization and spectral shift, among others[129]. To date, the most common fluorescent temperature-sensing probes extract temperature information by changes in signal intensity, variation in the fluorescence lifetimes, as well as band-shape.[128, 130, 131, 136, 137, 145, 146] In the first case, fluorescence varies with changing temperature and may be observed as an absolute increase (or decrease) in signal. Lifetime nanothermometry is independent of signal intensity and allows for the extraction of thermal information through variation in the lifetime of the fluorescence event. Lastly, band-shape nanothermometry exploits the presence of two or more fluorescence bands. The fluorescence intensity (or area) is monitored for both bands over the temperature range and a comparative relationship is established. This method is advantageous over other methods since it is not concentration-dependent, does not rely on temperature-dependent decay curves and does not suffer from environmental interference (*e.g.* surrounding media or environment, variability in cell uptake at different temperatures, *etc.*).[140]

Among luminescent nanomaterials, carbon dots have garnered significant attention in recent years due to their versatile optical properties, notably tunable fluorescence and high photostability.[47, 50, 60, 147, 148] In addition, they are dispersible in water, have excellent biocompatibility and low cytotoxicity.[47, 65, 93, 95, 148-150] As such, they can be integrated into bio-imaging and diagnostic applications such as fluorescent nanothermometry. Recently, carbon dot optical probes have been investigated for temperature sensing applications *in vivo* and *in vitro*.[131, 138, 145, 146, 151-153] *Yang et al.* [146] reported the synthesis of low cytotoxic biocompatible carbon dots with temperature-dependent fluorescence intensity from 20 to 80 ˚C and a thermal sensitivity of 0.85% $˚C^{-1}$. They extended their work to show temperature-dependent fluorescence in an *in vivo* mouse model. In

another study,[138] temperature-sensitive fluorescence lifetime carbon dot nanothermometers showed a sensitivity of 1.79% and promising results for temperature sensing in cells. In a different approach,[145] a ratiometric carbon dot temperature sensing probe was developed over the range of 5 to 85 ˚C. This was achieved *via* deconvolution of overlapping fluorescence bands resulting in a thermal sensitivity of 1.48% ˚C^{-1}. *Wang et al*.[154] circumvented the need for deconvolution of peaks through the development of nanohybrids consisting of carbon dots and gold nanoclusters, which yield blue and red emission, respectively, with a thermal sensitivity of 1.8% C^{-1}.

Distinct fluorescent bands emanating from a single probe is ideal for ratiometric temperature sensing to minimize variability and ensure homogeneous physico-optical properties. Few reports have focused on dual-fluorescing carbon dots (dCDs) [145, 155-157] and the majority do not describe the use of these dots for fluorescence thermal sensing. To this end, we report a facile synthesis of biocompatible dCDs for fluorescence nanothermometry in live cells. Their capacity to simultaneously fluoresce in the blue and red regions of the spectrum originates from two different emissive states on the dCDs.[70, 145] Due to their unique optical properties, temperature sensing over the range of 5-60 °C can be accomplished *via* changes in fluorescence intensity or a ratiometric approach that utilizes both fluorescence signatures. The temperature sensitivity of the dCDs was assessed in colloidal dispersions and HeLa cancer cells, extending the thermometric relationship to biological systems.

3.3. Results and Discussion

3.3.1. Physico-Chemical and Optical Characterization

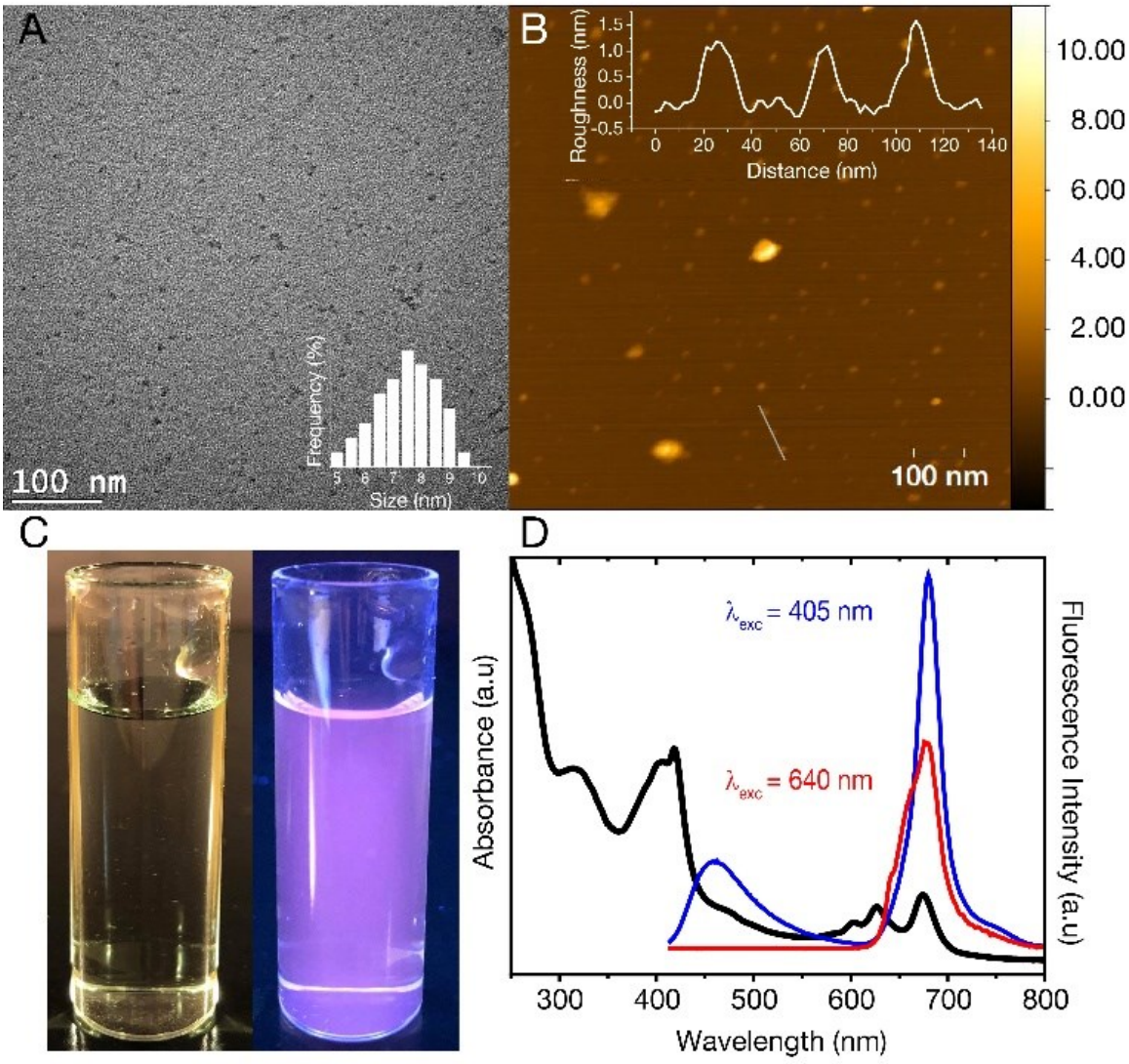

Figure 3.1 (A) TEM image of a 1 mg/mL dCD dispersion in water. The TEM image reveals quasi-spherical dots with a calculated particle size of 7.3 ± 1.2 nm – Inset: particle size distribution shows that the particle size spans 5-9 nm; (B) AFM image of dCDs on a mica substrate. The height profile is 1.4 nm as shown in the inset; (C) dCD dispersion under white light (left) and UV light (λ_{ex} = 365 nm; right). The violet color is from the contribution of both blue and red fluorescence; (D) Room temperature absorbance and fluorescence spectra of a 50 µg/mL dCD dispersion. The UV-Vis absorption spectrum of dCDs (black curve) reveals three absorption bands centered at 295-350 nm, 370-450 nm and 590-690 nm. Following excitation at 405 nm, two fluorescence bands are observed at 370-500 nm and 640-730 nm (blue curve) while excitation at 640 nm reveals red fluorescence from 645-730 nm (red curve).

The dCDs were synthesized in a one-step microwave assisted-reaction using formamide and glutathione. Quasi-spherical dots were obtained following synthesis at 180 °C for a period of 5 minutes. Transmission electron microscopy (TEM) particle characterization (**Figure 3.1**A) show that the dots are monodisperse with an average size of 7.3 ± 1.2 nm. Particle size statistics obtained for a large population of the dots reveals a Gaussian size distribution (**Figure 3.1**A inset) ranging from ~5-9 nm. Atomic force microscopy (AFM) analysis confirms our TEM findings showing that the dCDs are indeed spherical. The dCDs remain well dispersed in water and do not display any significant agglomeration upon drying on the AFM mica substrate with an average height of 1.4 nm (**Figure 3.1**B inset).

We characterized the optical properties of the purified dCDs, which form a colourless dispersion in water at a concentration of 50 μg/mL. Following exposure to UV (λ_{ex} = 365 nm), a violet colour is observed due to the simultaneous contributions of blue and red fluorescence (**Figure 3.1**C). UV-Vis absorbance spectroscopy reveals that the dCDs have three distinct absorption bands at 295-350 nm, 370-450 nm and 590-690 nm (**Figure 3.1**D). The first band is assigned to the transition of C=C bonds while the second and third bands can be ascribed to the $\pi \rightarrow \pi^*$ and $n \rightarrow \pi^*$ transitions of the aromatic sp^2 domains for the C=O, as well as the C=N/C=S bonds, respectively.[56, 70, 158] Thus, the dCDs can be excited at multiple wavelengths in the blue and red regions of the spectrum. Following excitation at 405 nm, the dCDs exhibit two distinct fluorescence bands between 370-500 nm (blue component) and 645-730 nm (red component) as shown in **Figure 3.1**D. Conversely, excitation at 640 nm only results in fluorescence in the region of 645-730 nm. The ability to selectively excite the dCDs at longer wavelengths is attractive for bioimaging applications due to greater tissue penetration and decreased scattering.[68-70, 88, 93, 132, 159, 160] Quantum yield measurements were carried out to evaluate the fluorescence efficiency of the dCDs. Following excitation at 405 nm, a cumulative quantum yield of 6.49% was obtained using an integrating sphere with individual values of 0.38% and 6.11% ascribed to the blue and red components, respectively. This is expected since the red fluorescence dominates its blue counterpart as shown in **Figure 3.1**D. Its unique fluorescence dual-fluorescence property is suggested to be originating from the carbon core and surface molecular emission states. Herein, the blue fluorescence stems from the core of the dCDs, while there red counterpart originates from the fluorophores covalently attached to the carbon core. Colloidal dCDs remain optically stable

over a span of 6 months (**Figure S3.1**A) and their optical properties do not suffer any significant degradation.

To assess the physico-chemical makeup of the dCDs and to understand the origins of their unique fluorescence properties, X-ray photoelectron spectroscopy (XPS) and Fourier Transform Infrared (FT-IR) analyses were carried out. The XPS survey spectrum of the dCDs (**Figure 3.2Figure 3.2**A) shows four binding energies at 532.08, 400.08, 286.08 and 165.08 eV corresponding to carbon (C1s), nitrogen (N1s), oxygen (O1s) and sulfur (S2s), respectively. This observation is in accordance with what is expected given that these four elements make up the chemical composition of glutathione or formamide. High-resolution XPS (HR-XPS) analysis of the C1s binding energies and subsequent deconvolution of the observed peak reveals three components at 288.68 eV, 286.89 eV and 285.58 eV ascribed to the presence of the C-C/C=C, C-O and the C=O/C=N functional groups, respectively (**Figure 3.2**B). Similarly, the HR-XPS N1s spectrum (**Figure 3.2**C) can be

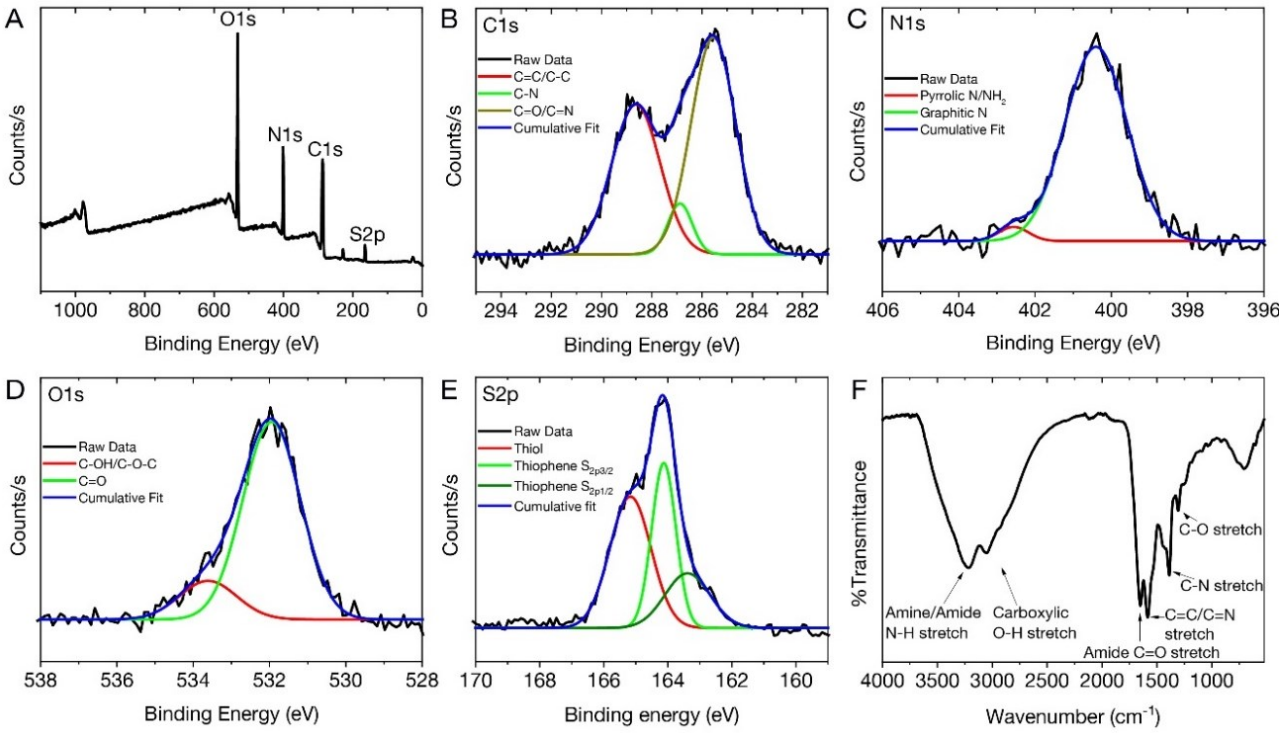

Figure 3.2 (A) XPS survey spectrum of the dCDs reveals 4 binding energies ascribed to C1s, N1s, O1s and S2p. Deconvoluted HR-XPS spectra of the binding energies are ascribed to (B) C1s at a maxima of 286.08 eV; (C) N1s at a maxima of 400.08 eV; (D) O1s at a maxima of 532.08 eV; (E) S2p at a maxima of 165.08 eV; (F) FT-IR spectrum of the dCDs revealing the presence of N-H and O-H surface groups along with amide and carbonyl stretches.

deconvoluted resulting in binding energies at 402.71 and 400.58 eV, which represents NH_2/pyrrolic N, as well as graphitic N, respectively. For O1s (**Figure 3.2**D), the HR-XPS spectrum shows the presence of C-OH/C-OC and C=O functional groups with deconvoluted binding energies observed at 533.26 and 532.02 eV, respectively. Lastly, for S2p (**Figure 3.2**E), three prominent binding energies are noted at 165.51, 164.14 and 163.38 eV; the former is attributed to the thiol functional groups on the dCDs while the latter is assigned to the presence of thiophene groups. The data confirm the presence of C=O, C=N and C=S, which are believed to be found in the conjugated network responsible for the red absorption/emission shown in **Figure 3.2**D.[56, 70] The dCDs are comprised of 53.1% carbon, 26.1% oxygen, 17.4% nitrogen and 3.4% sulfur as determined using HR-XPS spectra.

Our XPS assignments are corroborated by FT-IR analysis (**Figure 3.2**F). The presence of a broad peak from 3000-3500 cm^{-1} is assigned to the N-H and O-H stretching vibrations originating from hydroxyl and amine groups, while stretches at 1645 and 1583 cm^{-1} reveal the presence of C=O of an amide and of C=C/C=N bonds, respectively. The presence of an amide bond is further confirmed *via* observation of stretches at 1386 cm^{-1} and 1307 cm^{-1}, which are attributed to the C-N amide bonds. The thiol stretch is not observed in the FT-IR spectrum, which is expected since this stretching vibration is characteristically weak in intensity.

3.3.2. Temperature-Dependent Fluorescence

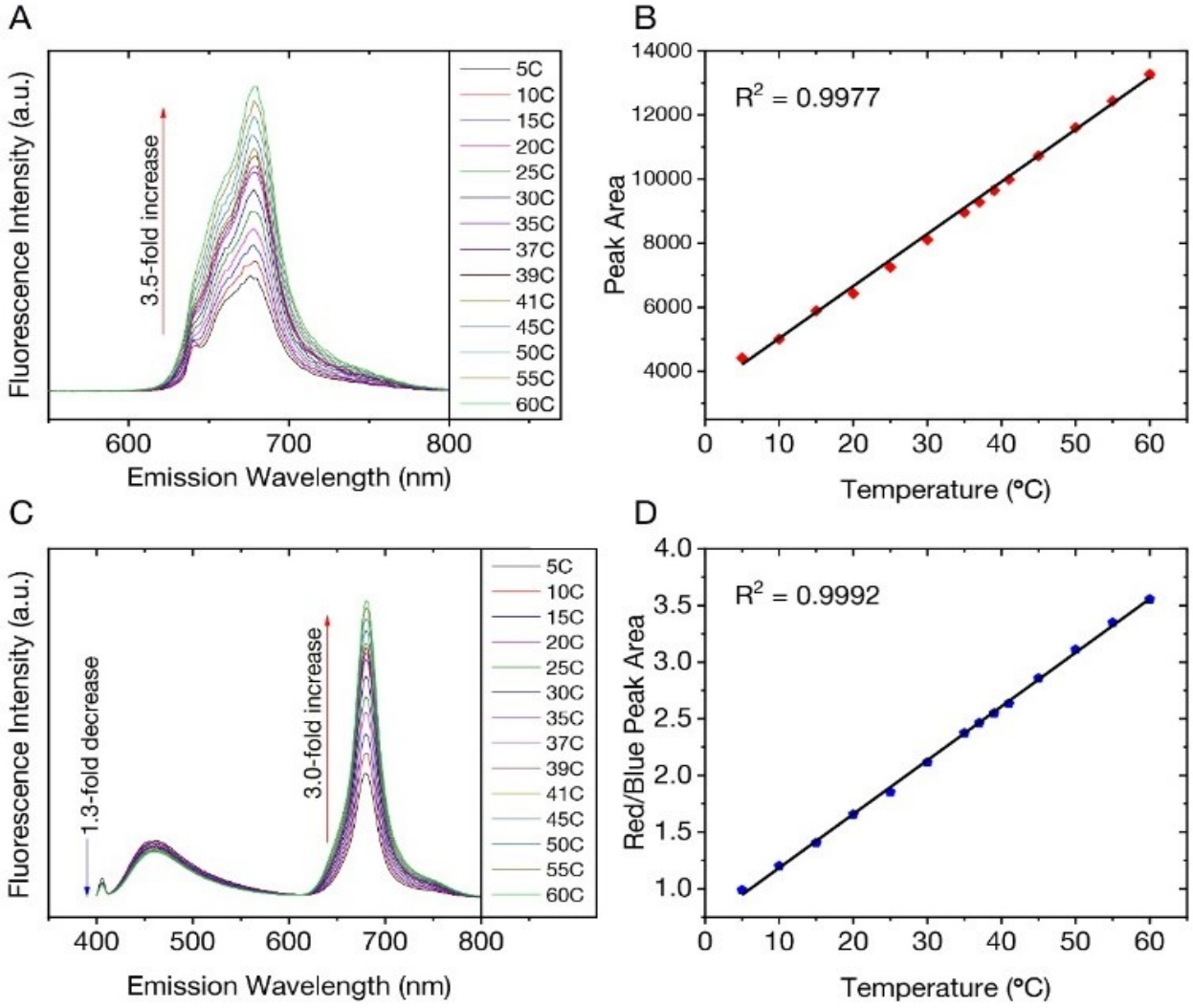

Figure 3.3 (A) Excitation at 640 nm yields a 3.5-fold increase in fluorescence intensity and the corresponding integrated area is plotted in (B) showing a linear response over the range of 5-60 °C; (C) Changes in the fluorescence spectra of the dCDs (λ_{ex} = 405 nm) as a function of temperature over the entire range. A 1.3-fold decrease is noted for the blue fluorescence in contrast to the 3-fold increase for the red counterpart; (D) The ratio of the integrated areas of the red and blue fluorescence components are plotted as a function of temperature showing a linear increase over the entire temperature range.

We found that the fluorescent properties of aqueous colloidal dispersions of dCDs are temperature dependent. Following excitation at 640 nm, the fluorescence intensity and integrated area increase over the range of 5 - 60 °C by a factor of 3.5 (**Figure 3.3**A). As shown in **Figure 3.3**B, a linear response (R^2 = 0.999) is observed over the entire analysis range and the temperature sensitivity

was determined to be as high as 3.71% °C^{-1}. This value is comparable with various other polymer- and quantum dot-based nanothermometers.[161]

The temperature-dependent fluorescence was also studied following excitation at 405 nm. Interestingly, the blue and red fluorescence bands are not equally sensitive to the change in temperature. With increasing temperature, the fluorescence intensity (and corresponding integrated area under the curve) of the blue component shows a very slight decrease in contrast to the red component, which significantly increases (**Figure 3.3**C). These observations are noted over the range of 5 - 60 ˚C where the blue emission decreases by a factor of 1.3 in contrast to the red emission, which increases by a factor of 3.0. Using Equation 3.1, a red-to-blue fluorescence ratio is obtained for every analysis temperature.

Equation 3.1

$$R = \frac{Integrated\ area\ of\ the\ red\ fluorescence\ (\lambda_{ex} = 405\ nm)}{Integrated\ area\ of\ the\ blue\ fluorescence\ (\lambda_{ex} = 405\ nm)}$$

As shown in **Figure 3.3**D, the ratio of red to blue fluorescence increases with temperature and a highly linear response is observed with an R^2 = 0.998. These analyses were repeated in triplicate on 3 unique samples and the linear plot reflects the average of these measurements, which have small deviations at each temperature. The thermal sensitivity of the dCDs, over the entire temperature range, varied from 1.33 - 4.81 % °C^{-1}, which is an improvement over previously reported carbon dot nanothermometry systems[138, 145] and other dual-emitting nanomaterials such as quantum dots and metal organic frameworks-dye composites.[162-164] The thermal resolution of the dCDs was calculated to be 0.048 K^{-1} indicating that it is possible to measure small thermal changes. Our system is unique in comparison to other carbon dot systems since the dual fluorescence originates from the same probe and does not require the addition of a second fluorescent probe. It should be noted that the fluorescence response of the dCDs, following a thermal event, is quick thus making it an ideal candidate for real-time temperature monitoring. As shown in **Figure S3.2**, the fluorescence ratio stabilizes after only 2 min, which is the time required for the entire volume of the cuvette to reach thermal equilibrium.

The reversibility and stability of the temperature-dependent fluorescence of dCDs were evaluated through thermal cycling experiments (**Figure S3.3**). The thermal reversibility of dCDs was

assessed by measuring recovery through multiple heating and cooling cycles from 5 to 60 °C. The results show that the initial fluorescence intensity does not significantly change following multiple heating and cooling cycles indicating their ability to recover following a thermal event.

3.3.3. Cell Uptake and Cytotoxicity of dCDs

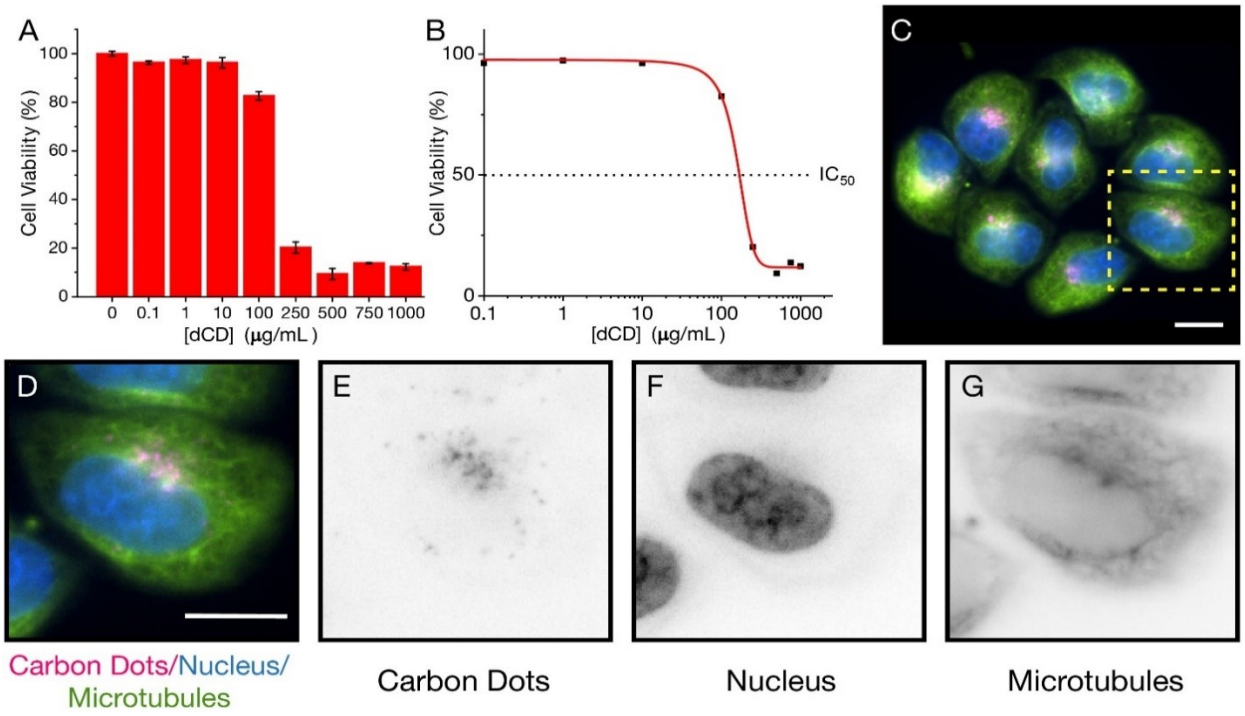

Figure 3.4 The viability and localization of dCDs in HeLa cells 48 h after treatment is shown. (A) The bar graph shows the proportion of live HeLa cells treated with different concentrations of dCDs as indicated on the x-axis; (B) An IC_{50} graph using log-scale shows HeLa cancer cell viability, which was measured to be 147.8 µg/mL (dotted line); (C) Fluorescence microscopy image showing dCD-treated HeLa cancer cells co-stained with Hoescht to label DNA (blue) and Tubulin Tracker™ Green to label microtubules (green). The scale bar corresponds to a length of 10 µm; (D) A magnified image of a single cell (dashed box in C) shows the nucleus (DNA; blue), microtubules (green) and red-emitting dCDs. Inverted greyscale images show the (E) can dots, (F) nucleus and (G) microtubules.

We extended our study of the temperature-dependent optical properties of dCDs in cultured mammalian cells to validate their use in a model biological system. Prior to evaluating their temperature-sensing capabilities, the cytotoxicity of dCDs was assessed in HeLa cervical cancer cells. As shown in **Figure 3.4**A, viability assays were performed using increasing concentrations of dCDs (from 0 – 1000 µg/mL) for 48 hours. Cells remained viable up to a concentration of 100

μg/mL of the dCDs with an IC_{50} value (*i.e.* concentration at which 50% of the population remains) of 147.8 μg/mL (**Figure 3.4**B). This suggests that the dCDs have low cytotoxicity and are biocompatible.

To determine their fluorescent properties and subcellular location, HeLa cells were treated with 100 μg/mL of dCDs for 24 hours to allow for cellular uptake and then imaged using fluorescence microscopy at 640 nm (**Figure 3.4**C-G). The cells survived and maintained their integrity over 24 hours in support of the dCDs' low cytotoxicity (see **Figure S3.4**). Interestingly, the dCDs accumulated in the endomembrane network in regions that likely correspond to the ER-Golgi. This network is typically found surrounding and adjacent to the nucleus (shown in blue; **Figure 3.4**D-F). Considering that the localization of the dCDs is specific to this perinuclear region (Golgi-ER network), the fluorescence remains unaffected by any variation in pH. In HeLa cells, the pH of the Golgi-ER network is approximately 6.6, while that of the cytoplasm is typically at 7.0 - 7.4.[165] We have studied the dependence of fluorescence on the pH of the medium (**Figure S3.5**) and it was observed that at pH values between 4 and 8, there are no significant changes to the fluorescence ratios for the dCDs. As such, the reported ratios measured in both the cuvette and intracellular models are reliable.

3.3.4. Intracellular Temperature-Dependent Fluorescence

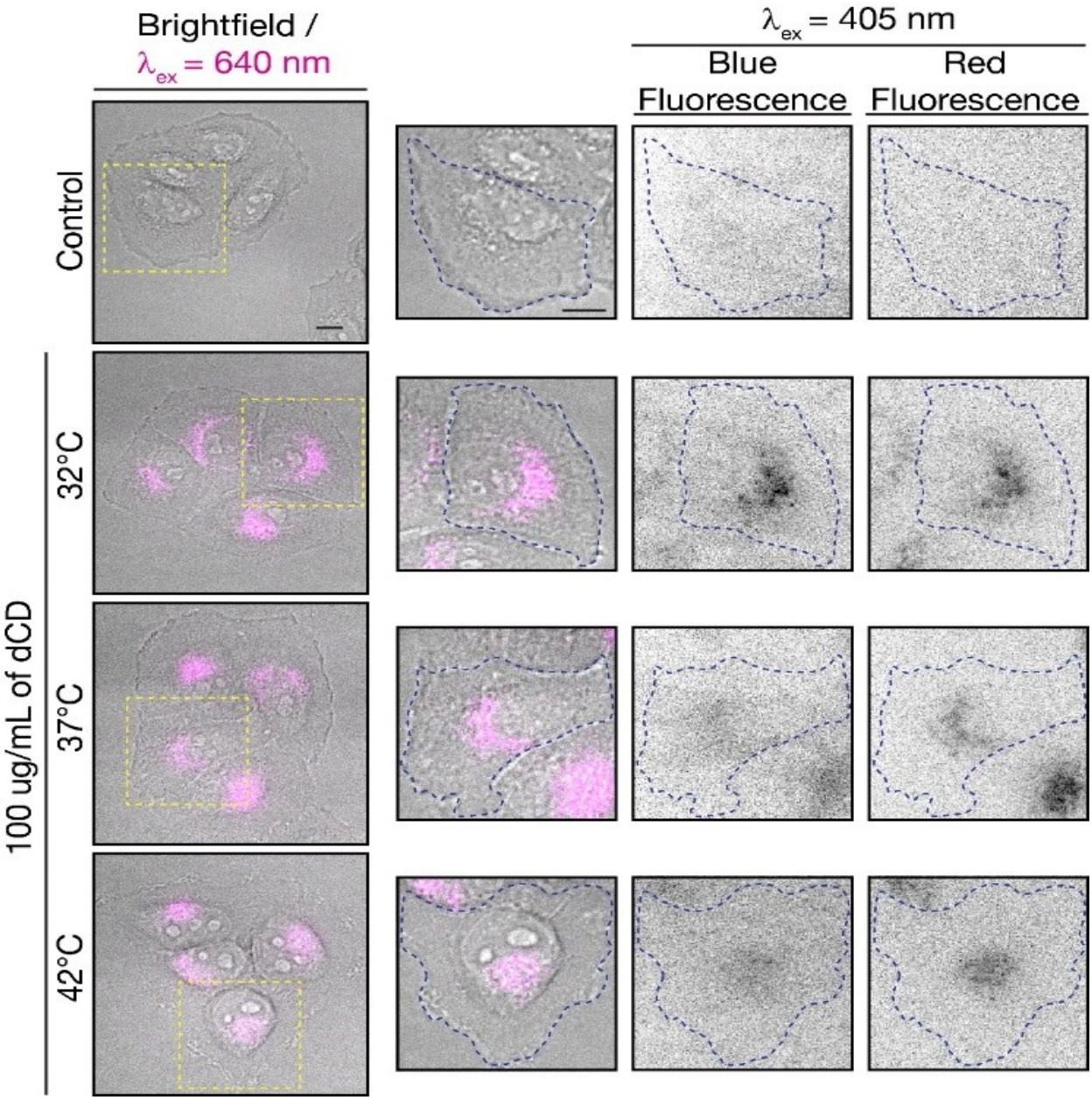

Figure 3.5 Fluorescence microscopy images of dCD-treated HeLa cells. Fluorescence signals from the dCDs (λ_{ex} = 640 nm; left and 405 nm; right) are shown for cells incubated at the different temperatures as indicated. The scale bars represent a length of 10 µm. The red-to-blue fluorescence ratios are 1.8 at 32 °C, 2.0 at 37 °C and 2.3 at 42 °C. The control shows untreated HeLa cells at 42 °C with no fluorescence signal as expected.

To determine if the dCDs could sense temperature changes inside the cells, *in vitro* thermal sensing using both intensity and ratiometric approaches were performed. HeLa cells treated with dCDs were allowed to equilibrate at 32, 37 and 42 °C (see **Figure 3.5** and Fig. S6 for controls at each temperature). Excitation at 640 nm allows us to selectively monitor the red fluorescence of the dCDs in cells. As shown in **Figure S3.7**, the thermal changes did not correlate with a change in intensity (λ_{ex} = 640 nm). This could be due to changes in intracellular concentration or localization of the dCDs at higher temperature. Thus, simply relying on changes in fluorescence intensity does lead to accurate intracellular thermal sensing.

In contrast, we do not have these limitations using the ratiometric approach. The dCDs maintain dual blue and red fluorescence in cells following excitation at 405 nm, as previously observed for the colloidal dispersions (**Figure 3.5**). The red-to-blue ratio increases with increasing temperature, with ratios of 1.8 at 32 °C, 2.0 at 37 °C and 2.3 at 42 °C. Strikingly, these values are comparable to those observed in the cuvette model suggesting that the ratiometric relationship of the red-to-blue fluorescence of the dCDs is maintained in cells, as shown in **Figure S3.8**. This highlights the advantage of ratiometric temperature sensing in the development of fluorescent nanothermometry probes. Regardless of the amount of dCDs taken up by the cells, which can be affected by various factors such as confluency, the relative red-to-blue emission ratio remains unaffected and is not concentration dependent. Lastly, the dCDs have shown fluorescence reversibility with respect to changes in intracellular temperature. Following incubation in HeLa cells, they were subjected to a heating/cooling cycle from 32 $\rightarrow$ 42 $\rightarrow$ 32°C. Rapid temperature changes were induced through the replacement of the cell media at the respective temperatures. Following analysis of an excess of 30 cells at each thermal event, the fluorescence properties remained unaffected with corresponding ratios of 1.5 $\rightarrow$ 2.2 $\rightarrow$ 1.7. This highlights the robustness of the proposed dCD-nanothermometer and these findings further demonstrate the fluorescence reversibility as shown in **Figure S3.3B**.

3.3.5. Conclusion

In this study, we describe the synthesis and physico-chemical properties of biocompatible dual-fluorescing carbon dots *via* the microwave reaction of formamide and glutathione. The water dispersible dCDs possess temperature-sensitive and reversible fluorescence. They show linear

responses to change in temperature from 5 to 60 °C in a cuvette model determined by intensity-based and ratiometric temperature sensing methods. These results translate into an in vitro cell model, where the ratiometric change in fluorescence was also observed in cells incubated at different temperatures. Unlike intensity-based measurements, temperature measurements using the ratiometric approach are not impacted by changes in dCD concentration, which could vary due to altered cellular uptake depending on cell density and/or temperature. With its facile synthesis, unique optical properties and biocompatibility, these dCDs are good candidates for in vivo nanothermometry in biological systems. Furthermore, they could be explored for bioimaging applications in the future.

3.4. Experimental Section

Chemicals and Reagents - Formamide (≥99.5%) and reduced L-glutathione (≥98.0%) were purchased from Thermo Scientific. Phosphate buffer solution (PBS, 1X) and Dulbecco's modified Eagle Medium (DMEM) were purchased from Wisent. HyClone™ Calf Serum and Tubulin Tracker Green™ were purchased from Thermo Scientific. The WST-8 Cell Proliferation Assay Kit was purchased from Cayman Chemical. All reagents were used without further modification or purification.

Synthesis of Dual-Fluorescing CDs (dCDs) - The dCDs were synthesized using a modified microwave-mediated one-step reaction with glutathione and formamide as previously reported.[36] Briefly, a 20 mL solution of 0.1M glutathione in formamide was prepared. The mixture was sonicated for 15 min until it changed from a cloudy to a clear homogeneous solution. The solution was then transferred to a 35 mL microwave reaction vial and heated to 180°C for 5 min. Once cooled, the dispersion was dialyzed using a cellulose ester membrane dialysis membrane (molecular weight cut-off = 3.5 – 5.0 kDa) to remove unreacted materials and fluorophores. The sample was dialyzed for over five days with the water changed twice a day. Following this, the sample was passed through a 0.2 □m nylon filter to remove any aggregates. Subsequently, the samples were washed twice with ethanol and twice with acetone (1:10, sample:solvent volume ratio) to remove any remaining impurities. After each wash, the precipitate was collected by centrifugation at 10 000 x g for 10 min. The resulting material was dried in the oven at 70°C overnight and resuspended in water.

Characterization Techniques - For Transmission Electron Microscopy (TEM), CDs were dispersed in water at a concentration of 5.0 mg/mL. Grids were prepared by pipetting 2 µL of the dCD dispersion onto a 200 mesh Formvar/carbon coated copper grid (3 mm in diameter) followed by evaporation of the solvent. The TEM images were collected using a Jeol JEM-2100F microscope operating at 100 kV. Images were processed and the carbon dot sizes were determined using Fiji imaging software.[47] UV-visible absorption spectra were acquired from 200-800 nm on a Cary 5 Series UV-Vis-NIR Spectrophotometer (Agilent Technologies) using a 1 cm quartz cuvette. A 5.0 nm bandwidth and wavelength changeover at 450 nm were used for analysis. Data was processed using Cary Eclipse software. Quantum yield values were acquired on an FLS920 Fluorescence Spectrometer (Edinburgh Instruments) with an integrating sphere using a 1 cm quartz cuvette. The excitation and the emission slits were set to a width of 5 nm. The excitation wavelength was set to 405 nm and the spectra from 300-800 nm were collected. Scans were done in triplicates with a dwell time of 0.2 sec. Data was processed using F900 Software. Fluorescence spectra were acquired using a Cary Eclipse fluorescence spectrophotometer (Agilent Technologies). Spectra were acquired in a 1-cm quartz cuvette at λ_{ex} = 360-660 nm (5 nm intervals). The excitation and emission slits were set to a width of 5 nm with a PMT voltage at 600 V. All data were processed using Cary Eclipse software. To obtain fluorescence spectra at various temperatures, the Cary Single Cell Peltier Accessory (Agilent Technologies) was used to adjust the temperature from 5˚C to 60˚C. Fourier-Transform Infrared Spectroscopy (FT-IR) spectra were collected using a Thermo Scientific Nicolet iS5 equipped with an iD5 ATR accessory. Spectra were collected using 30 scans with a resolution of 0.4 cm^{-1}, a gain of 1, an optical velocity 0.4747 and an aperture setting of 100. Data was processed using Omnic 9 software. X-ray Photoelectron Spectroscopy (XPS) spectra of the dCDs were acquired using a Thermo Scientific K-Alpha X-Ray Photoelectron Spectrometer. Each analysis was carried out in triplicate with 10 runs for each scan. The averages were plotted for both the survey and high-resolution scans. The stability of the dCDs (50 µg/mL) was evaluated by measuring the fluorescence intensities from the same stock solution of dCDs once a month over a span of 6 months. Fluorescence intensity (λ_{ex} = 640 nm) centered around 680 nm was collected and used for the assessment.

Cell culture and WST-8 assays - HeLa cells were cultured in DMEM containing 10% calf serum and maintained in a humidified incubator set to 37°C with 5% CO_2. To assess cell viability, HeLa cells were plated in 96-well plates at 20% confluency and cultured overnight. The cytotoxicity of

the dCDs was assessed *via* WST-8 cell proliferation assays (Cayman Chemical). The cells were treated with dCDs at varying concentrations (0 to 1000 g/mL) and incubated for 48 hours. Subsequently, the WST-8 reagent was added for 4 hours. The optical density (OD) values were measured using the TECAN 200 PRO plate reader at a wavelength of 490 nm. Cell viability was measured as a ratio of the signal of treated cells vs. control:

$$\% \textbf{ cell viability} = \frac{OD\ (490\ nm)_{sample}}{OD\ (490\ nm)_{blank}} \times 100\%$$

All measurements were repeated in triplicate and the means were plotted with standard deviation.

Cellular Imaging - HeLa cells were imaged after treatment with the dCDs. Cells were plated in NuncTM Lab-Tek II 4-well chambered microslides (Thermo Scientific^{TM}) and left overnight to adhere. The dCDs were added to cells in media at a final concentration of 100 µg/mL for 24 hours. To determine the localization of dCDs, HeLa cells were treated with TubulinTracker Green Reagent (Molecular Probes) at a final concentration of 250 nM as per manufacturer's instructions to stain microtubules and Hoescht 33342 dye (Thermo Scientific^{TM}) at a final concentration of 75 nM to stain the DNA. The cells were then placed in the incubator at 37 °C with 5% CO_2 for 30 minutes after which the media was replaced. Imaging was performed using the Nikon-TIE inverted epifluorescence microscope with Lambda XL LED light sources using the 60x/1.4 oil objective, a Piezo Z stage (ASI), a Photometrics Evolve 512 EMCCD camera and Elements 4.0 acquisition software (Nikon). Images were captured as 0.5 µm Z-stacks and converted into maximum intensity Z-stack projections using FIJI (NIH).

Intracellular Nanothermometry - To measure the nanothermometric properties of the dCDs, HeLa cells were prepared as described above. In each Lab-Tek II chamber, three wells containing Hela cells were treated with 100 µg/mL of dCDs and placed at 32 °C, 37 °C or 42 °C for 2 hours prior to imaging (n_i = 30 cells). The controls were subjected to the same conditions, except without addition of the dCDs. After 2 hours, the wells were placed into an INU-TiZ-F1 chamber (MadCityLabs) with 5% CO_2 and heated at their respective experimental temperature for imaging, which was mounted on the stage on the inverted microscope. Imaging was carried out using the same microscope described above. Excitation at 405 or 640 nm was used to capture emission at 460 nm using a 400-600 nm bandpass (Chroma CT500/200bp) filter, or at 680 nm using a 610 nm

longpass (Chroma AT610lp) filter, respectively. Images were acquired as 0.5 μm Z-stacks using Elements 4.0 software (Nikon) and converted into maximum intensity Z-stack projections using FIJI (NIH). Background intensities were subtracted using the control. *In vitro* intracellular temperature was monitored following a thermal cycling regime to assess the reversibility of the fluorescence properties. Initially, the dCD-treated cells were incubated at 32 °C. Then, the temperature was rapidly cycled by replacing the media with media already equilibrated at 42 °C. Finally, the temperature was cycled down to 32 °C once again by replacing the media. The red-to-blue emission ratios were calculated at each temperature.

3.5. Supplementary Information

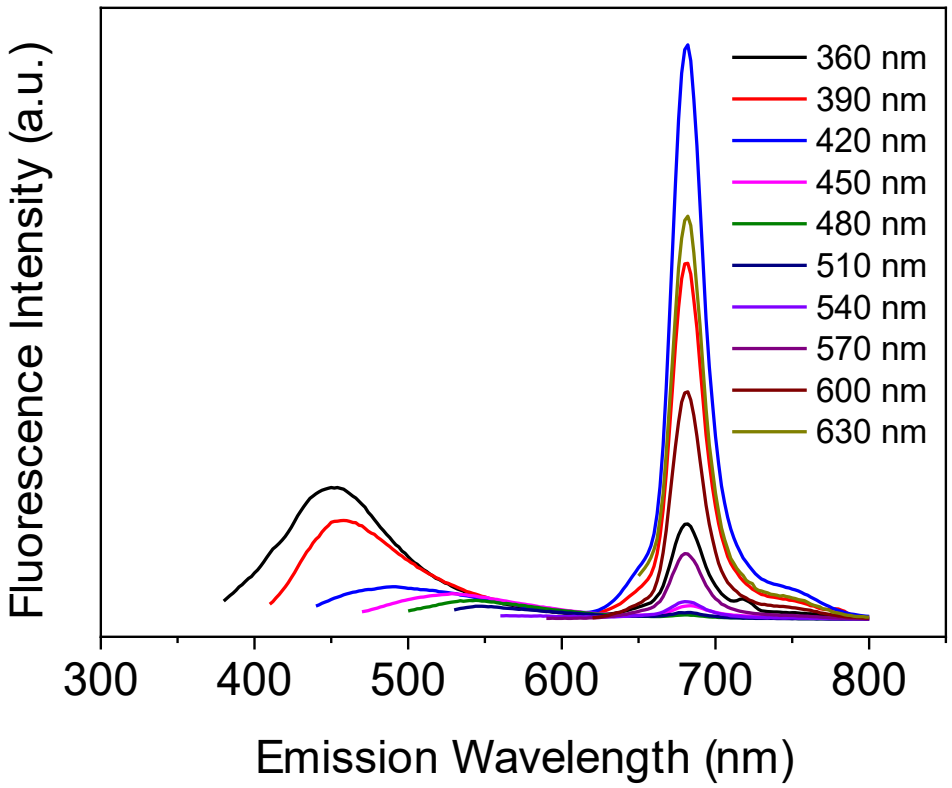

Figure S3.1 Fluorescence spectrum of a 50 μg/mL dCD dispersion highlighting the carbon core and molecule state fluorescence observed for dCDs. The excitation-dependent blue emission stems from the carbon core states and the excitation-independent red emission originates from the surface molecular states.

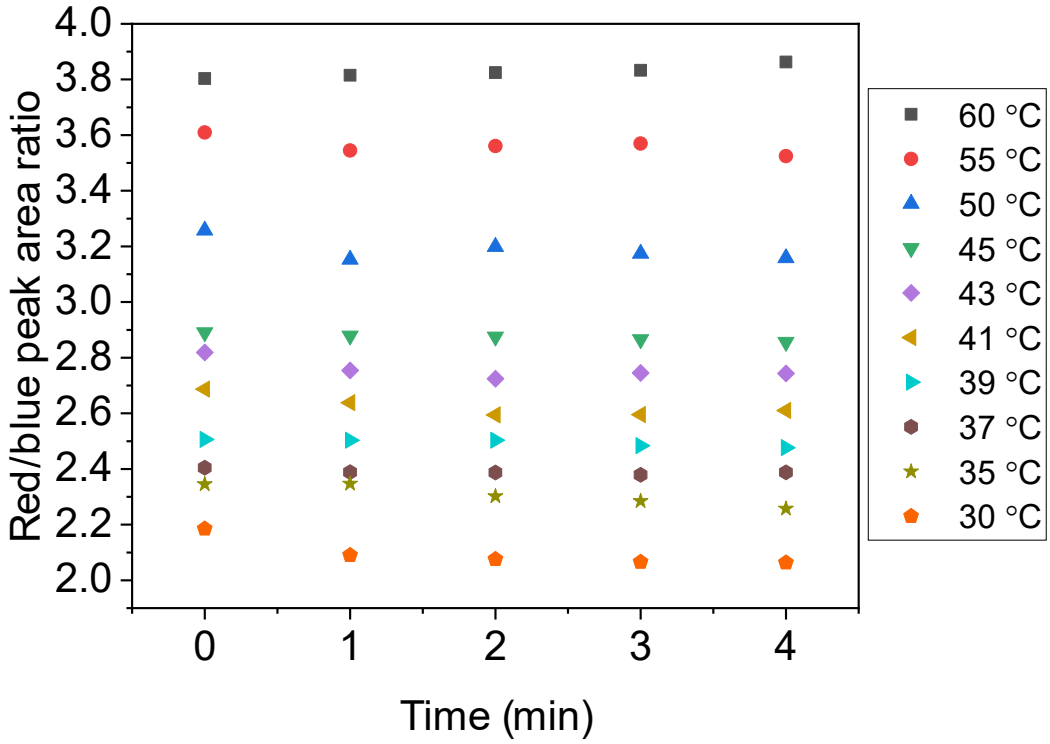

Figure S3.2 Time evolution of the fluorescence response at decreasing temperatures. The fluorescence was measured starting at 60 °C and then quickly cooled to a lower temperature as shown above. Each time point corresponds to the time elapsed once the single cell Peltier reading reached the desired temperature. The cooling time between temperatures was measured to be approximately 10-15 seconds. Plotted data suggests that the dCDs provide stabilized temperature readings after 2 minutes noting that this is the time required for the entire cuvette volume to reach thermal equilibrium.

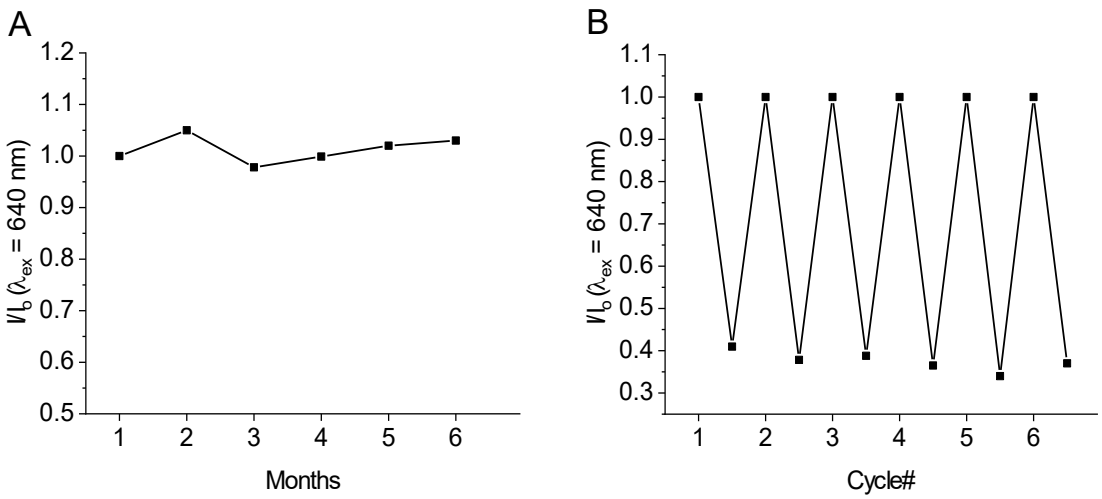

Figure S3.3 (A) The stability of the dCDs was assessed by measuring the fluorescence at 683 nm (λ_{ex} = 640 nm) once a month over a span of 6 months. No significant changes were observed over this time span; (B) The reversibility of the dCDs was evaluated by measuring the intensity at 683 nm (λ_{ex} = 640 nm) between several heating/cooling cycles. The fluorescence was observed to recover following several heating and cooling cycles with no significant changes.

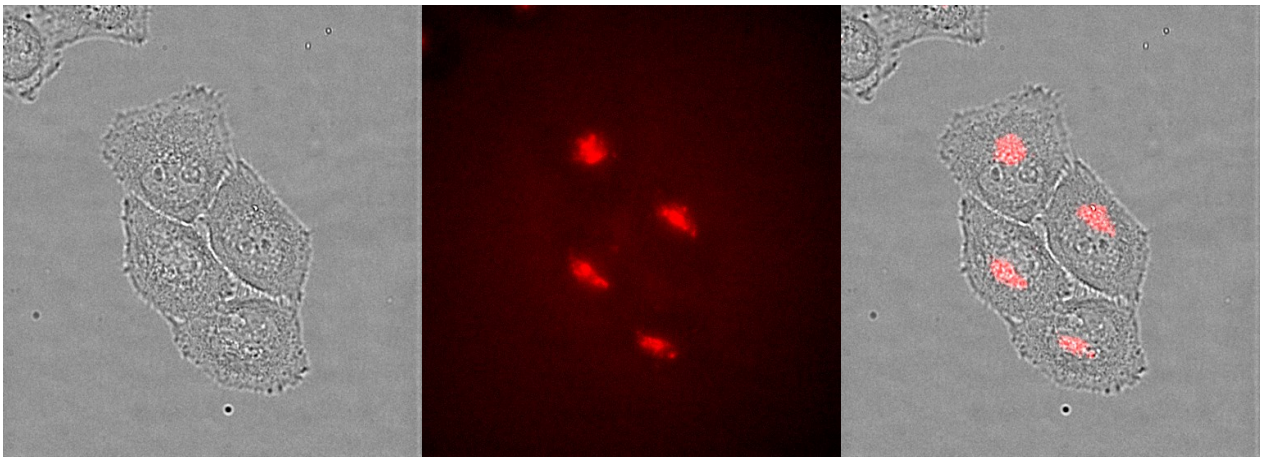

Figure S3.4 Fluorescence microscopy images of HeLa cells treated with 100 μg/mL of dCDs. From left to right: brightfield microscopy image of the treated HeLa cells, the fluorescence image (at λ_{ex} = 640 nm) of the treated HeLa cells showing the red fluorescence of the dCDs and the merged brightfield and fluorescence images. The integrity of the cell structure remained unaffected after 24 hours of dCD treatment.

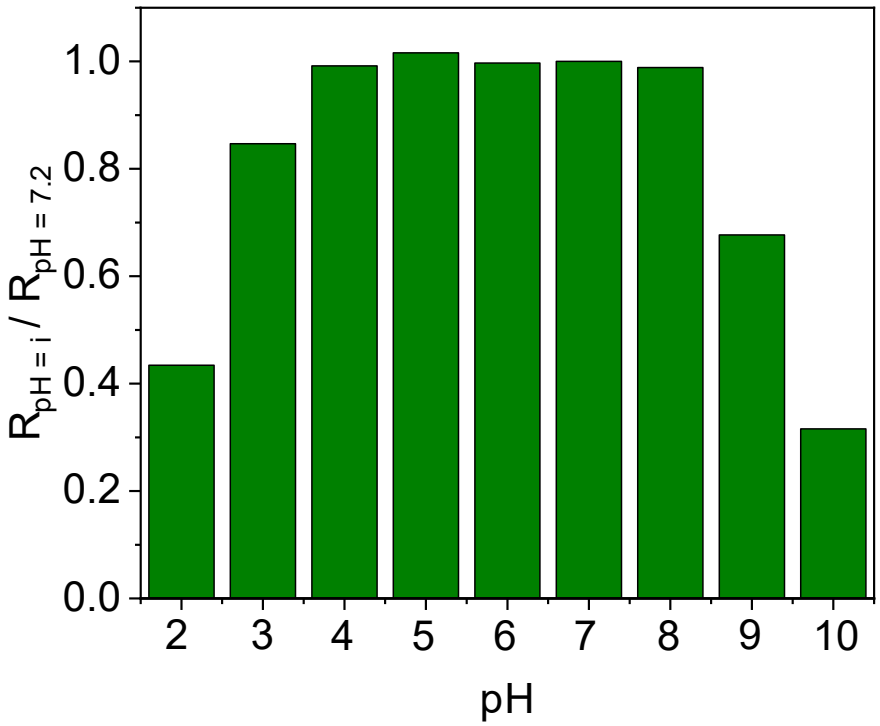

Figure S3.5 Relative red-to-blue fluorescence ratio of dCD colloidal dispersions at different pH levels. It is noted that the ratios do not change significantly between pH 4 - 8.

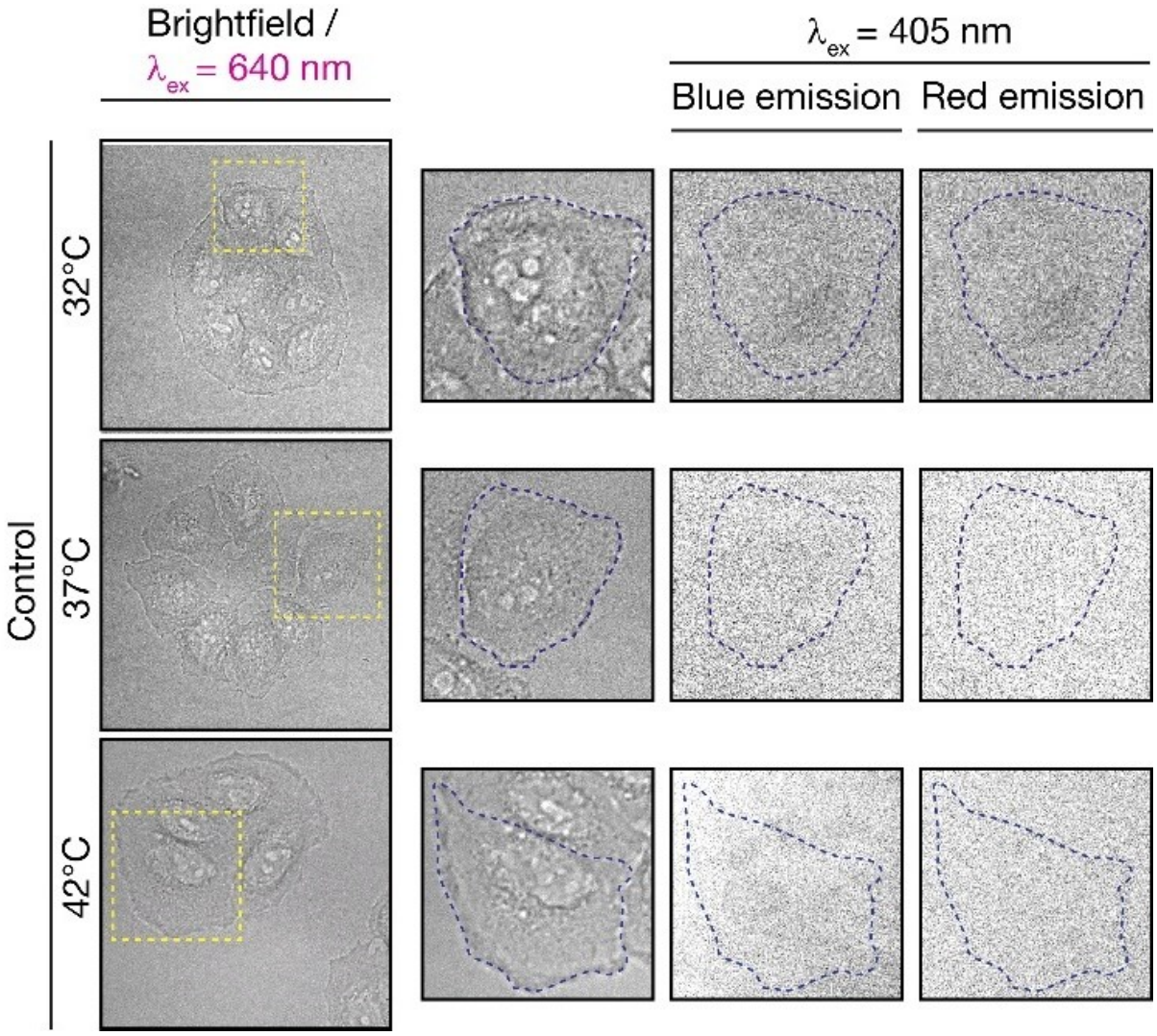

Figure S3.6 Cellular nanothermometry fluorescence microscopy controls, at various temperatures, using untreated HeLa cells (no dCDs). As expected, no fluorescence was observed in the Golgi-ER network.

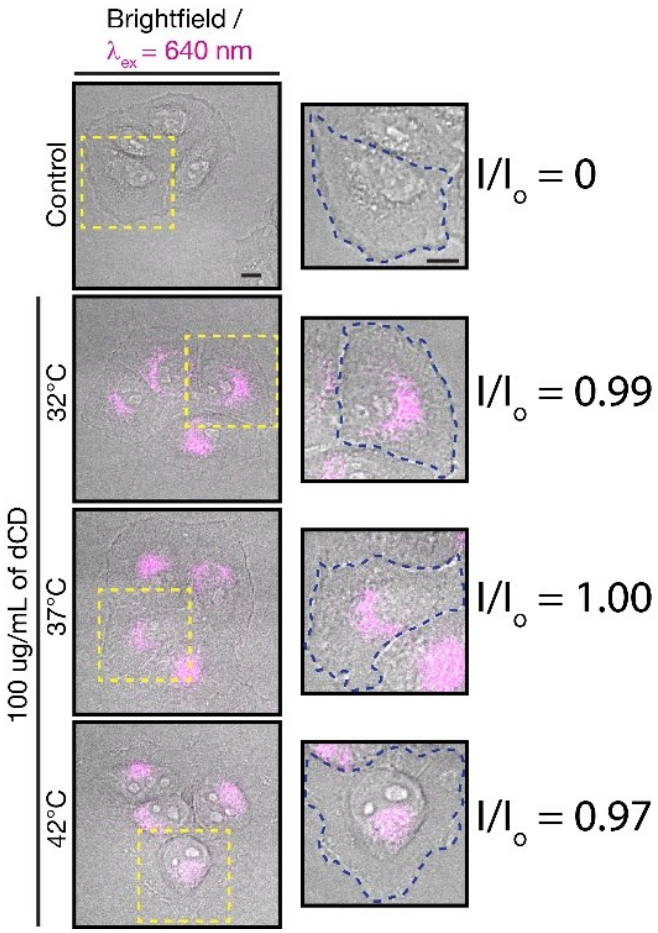

Figure S3.7 Overlay of brightfield and fluorescence images (λ_{ex} = 640 nm) of dCD-treated HeLa cells, at different temperatures. Temperature sensing solely using the red fluorescence signal is not feasible as the incubation temperature is likely affecting the cellular uptake generating a non-linear response.

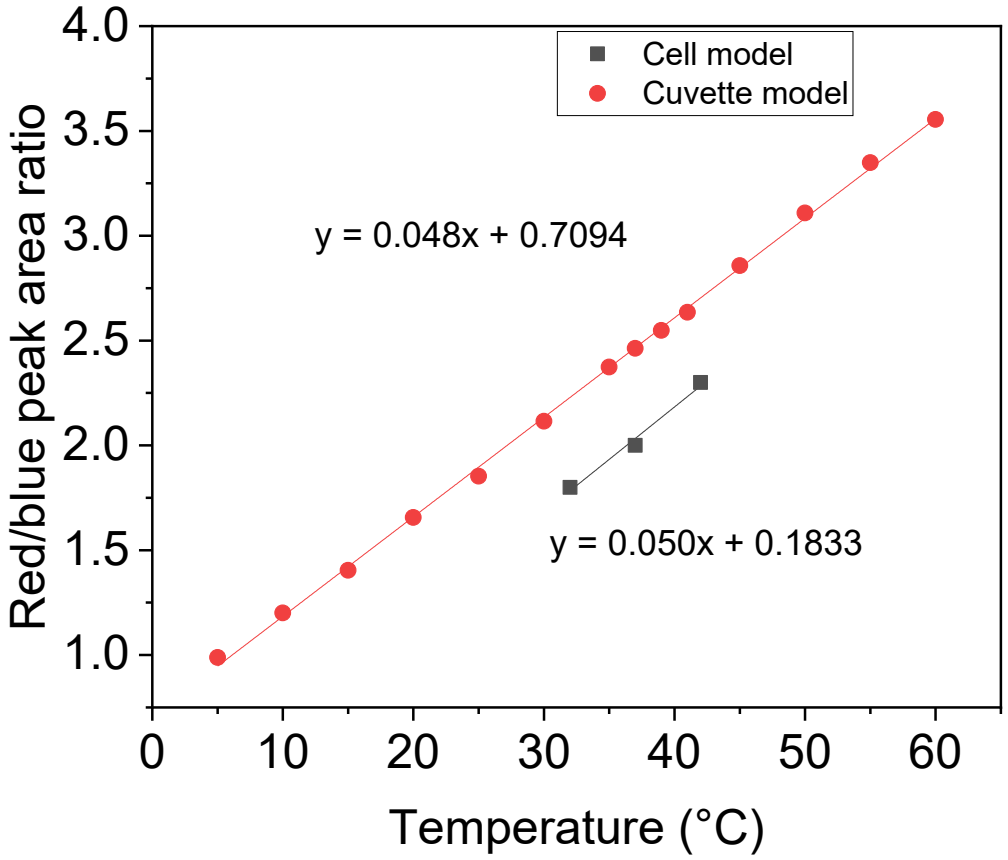

Figure S3.8 Changes in the red/blue fluorescence ratio of dCDs as a function of temperature (λ_{ex} = 405 nm) in both the cuvette model and intracellular models. Both demonstrate a linear ratiometric response relative to the change in temperature. Although their slopes are similar, the ratios are slightly lower in the cell model likely due to differences in the detection sensitivity between the epifluorescence microscope and the fluorimeter.

Chapter 4. Ratiometric pH sensing in Living Cells Using Carbon Dots

4.1. Abstract

The ability to precisely sense physiological pH changes in the cellular environment is exceedingly difficult. Novel technologies are thus required to address this challenge. Fluorescent nanomaterials can be exploited to this effect because their optical properties can exhibit strong pH dependence. Herein, an intracellular pH sensing probe was developed *via* a facile one-step microwave-reaction synthesis for the preparation of carbon dots (CDs) using glutathione and formamide. The CDs possess unique optical properties allowing for concomitant fluorescence in the blue and red regions of the spectrum. We investigated these dots as pH-sensors using the red fluorescence signatures at 650 nm and 680 nm. The two fluorescence bands respond differently following pH changes in their environment and could thus be used for ratiometric measurements. Cytotoxicity studies of the CDs in glioblastoma cells showed no decrease in cell viability up to 100 μg/mL (24h). Fluorescence imaging revealed that the dots localize in lysosomal compartments, with minimal association with mitochondria or cytoskeletal structures. Moreover, they can sense changes in lysosomal pH in response to serum and amino acid starvation, as well as administration of diclofenac and metformin, drugs currently in clinical trials for combination treatments of cancer. These CDs offer a new self-referencing approach for live intracellular pH sensing in 2D and 3D cell models.

4.2. Introduction

In the past decade, nanomaterials have gained significant attention due to their optical, physical and electronic properties, which greatly differ from their bulk counterparts.[166, 167] This has propelled materials design and innovation at the nanoscale, allowing for the improvement of existing devices and technologies, as well as the development of novel ones. Several nanomaterials – including polymer dots, quantum dots and lanthanide-doped upconverting nanoparticles – have been investigated.[31, 60, 168] More recently, carbon dots (CDs), an emerging member of the carbon-allotrope family, have garnered interest following their accidental discovery by the Scrivens group.[33, 47, 48] The interest in these dots is largely due to their tunable physico-chemical and optical properties. These quasi-spherical carbon nanodots are typically 10 nm in size and mainly

comprised of carbon, hydrogen, oxygen and nitrogen.[169] Their preparation can start with any carbon-containing molecule (*e.g.* sugars, amino acids, polymers).[42-44, 48, 97] The choice of precursor and synthesis route (e.g. microwave vs. hydro/solvothermal) allows to tailor their properties for targeted application development,[45, 53, 169] which extends to bioimaging, sensing and drug delivery, among others.[101, 170, 171] Carbon dots possess versatile optical properties, including the ability to concomitantly fluoresce at different regions of the electromagnetic spectrum, high fluorescence quantum yields, low photoblinking and resistance to photobleaching.[50, 101] Moreover, recent reports suggest that these dots possess low chemical/cytotoxicity and good biocompatibility.[9, 47, 172]. The functional groups of the precursor molecules directly impact the optical properties of CDs and play a critical role in how the CD interacts with its environment [173]. The fluorescence of these dots has been shown to depend on their surface and chemical makeup.[53, 60, 174] As such, their surface moieties (*e.g.* carboxyls, amines, thiols) have been exploited for the development of optical-based sensing assays[113, 146, 175-179], including pH-sensing.[180-182]

The pH in organelles, cytosol as well as in the extracellular compartment play an important role in many cellular events.[183] Many pathologies are associated with disrupted pH. There is a need for novel diagnostic tools[184] to accurately and precisely monitor intracellular and extracellular pH. A practical nanomaterial-based intracellular pH-sensing probe requires (i) suitable size, morphology and surface chemical composition, (ii) biocompatibility and minimal cytotoxicity, as well as (iii) sensitivity over a large pH range. To date, the majority of CD-based sensing probes rely on the increase or decrease in fluorescence intensity.[181, 185] Such systems are limited due to their concentration dependence and inability to address interferences from the environment, including inhomogeneous distribution of analytes, fluctuations in the optical probe concentration or variations in the surrounding matrix, among others.[183] It is in this regard that ratiometric approaches to sensing have come to light. A ratiometric approach utilizes the ratio of intensity/area of two fluorescence bands at different regions of the spectrum.[186] With its inherent self-referencing property, this method is concentration-independent and is not susceptible to external interferences. Ratiometric fluorescent pH sensors using carbon dots have been developed *via* the covalent modification of a carbon dot with a pH-sensitive molecule (*e.g.* fluorescein isothiocyanate);[187, 188] however, dual-fluorescence stemming from a single nanoparticle is

preferred to ensure a narrow distribution of physico-optical properties and ease of sensor design.[180]

Herein, we report the synthesis of glutathione and formamide-based CDs that sense intracellular pH in live cells using an optically based ratiometric approach. The dots possess dual fluorescence bands that emanate from distinct optically active centers and which respond differently to a change in their surroundings, independent of concentration. As such, they provide superior sensing capabilities relative to other optical sensors. The pH-sensing capability is most sensitive between pH 3-7 with high reversibility. Here, the dots have been applied to measure lysosomal adaptation to pharmacological agents in human glioblastoma cells and tumoroids.

4.3. Results and Discussion

4.3.1. Physico-Chemical and Optical Characterization

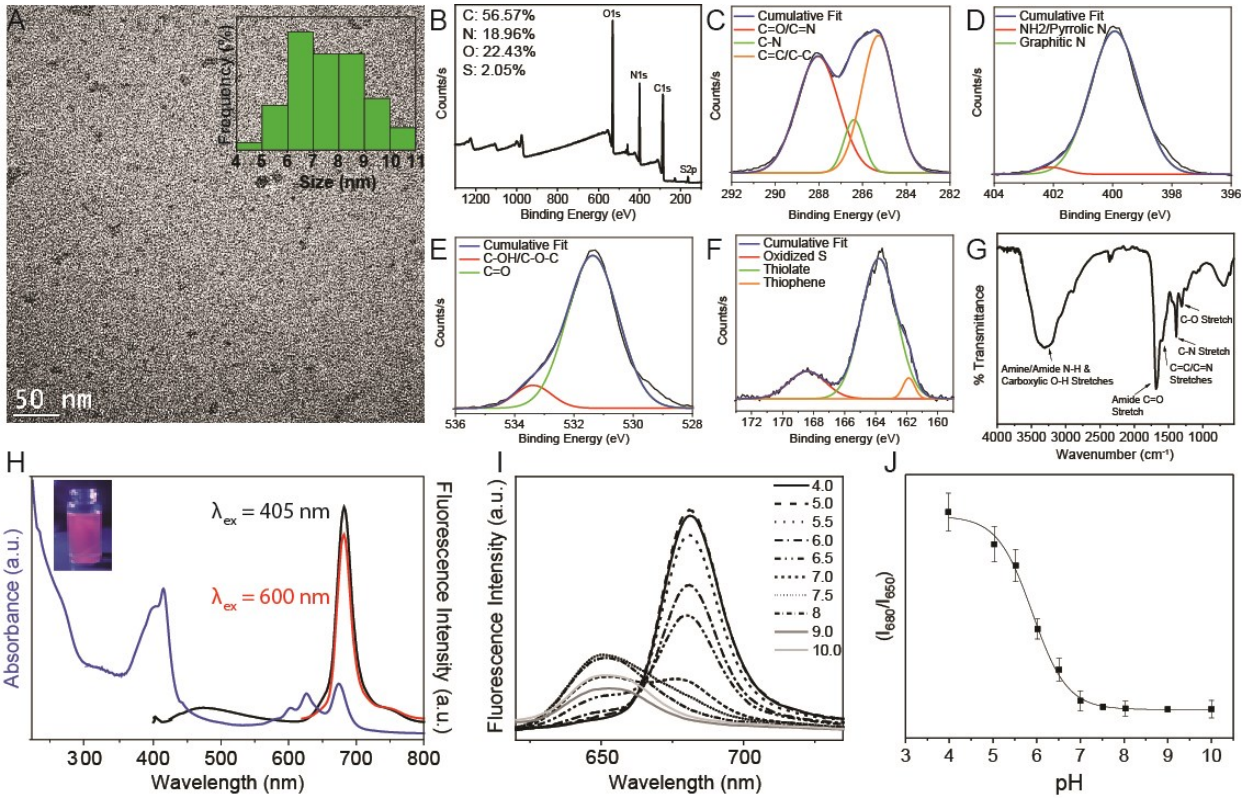

Figure 4.1 (A) TEM image of a 2 mg/mL CD dispersion in water. The images highlight the spherical dots with a calculated particle diameter size of 7.6 ± 1.4 nm – Inset: Gaussian size distribution spanning 4-11 nm; (B) XPS survey spectrum of the CDs, which reveal four binding energies for C1s, O1s, N1s and S2p; (C-F) HR-XPS spectra of the deconvoluted binding energies are assigned to (C) C1s at a maxima at 286.62 eV, (D) O1s at a maxima at 513.39 eV, (E) N1s at a maxima at 400.50 eV and (F) S2p at a maxima at 163.42 eV; (G) FT-IR spectrum of the CDs highlights the presence of O-H and N-H surface groups in addition to amide and carbonyl stretches; (H) The UV-Vis absorption spectrum highlights the three prominent bands at 250 nm, 420 nm and 580-690 nm. At an excitation wavelength at 405 nm, there are two fluorescence bands observed in the blue and red region of the spectrum, while excitation at 600 nm shows only red fluorescence; (I) Upon excitation at 600 nm, a change in fluorescence signatures is observed at 680 nm and 650 nm; (J) The ratio of the intensities at 680 nm and 650 nm shows a sigmoidal response to changes in pH.

Structural characterization by transmission electron microscopy (TEM; **Figure 4.1**A) shows that the dots are quasi-spherical in morphology. Size analysis on a large population of CDs yielded a Gaussian size distribution (**Figure 4.1A** inset) ranging from ~ 4-9 nm and a mean size of 7.4 ± 1.4 nm. It is noted that the TEM images show a weak image contrast due to the lack of crystallinity of

the dots. As shown in **Figure S4.1**, there is an absence of crystalline reflections with an amorphous halo spanning 10-30° 2θ in the XRD pattern.

The surface functional groups and chemical composition of the CDs were studied by X-ray photoelectron spectroscopy (XPS) and Fourier transform infra-red (FT-IR). The XPS survey spectrum of the dots (**Figure 4.1**B) show 4 binding energies at 513.39, 400.50, 286.62 and 163.42 eV corresponding to oxygen (O1s), nitrogen (N1s), carbon (C1s) and sulfur (S2p), respectively. In addition, the elemental composition was determined to be: 56.6% carbon, 19.0% nitrogen, 22.4% oxygen and 2.0% sulfur. This is expected as these are atoms make up both glutathione and formamide. **Figure 4.1**C-F show the high-resolution XPS spectrum of each element. The HR-XPS of C1s can be deconvoluted to 3 peaks: 285.31 eV, 286.40 eV and 288.47 eV corresponding to C=C/C-C, C-N and C=O/C=N, respectively. The HR-XPS for nitrogen reveal three prominent binding energies corresponding to NH_2/Pyrrolic N at 399.94 eV and graphitic N at 402.12 eV. For O1s, two peaks are assigned to C=O at 531.38 eV and C-OH/C-O-C at 533.38 eV. Lastly, for S2p, three major peaks are highlighted which correspond to thiophene S at 168.88 eV, thiolate S at 163.84 eV and oxidized S at 168.41 eV. The FT-IR analyses follow suit with the XPS data for the as-prepared CDs. A broad peak centered at 3303.84 cm^{-1} reveals is assigned to O-H and N-H stretching vibrations stemming from hydroxyl/carboxylic and amine groups. Amide bonds are confirmed with the stretches at 1684.27 cm^{-1}, 1309.66 cm^{-1} and 1305.92 cm^{-1}, which are ascribed to C=O, C-N and C-O, respectively. The peak at 1604.82 cm^{-1} is indicative of C=C/C=N peaks, which agrees with the XPS analyses.

At a concentration of 50 μg/mL, the dots form a colorless dispersion in water and display a red-violet colour when excited under blue light (**Figure 4.1**H inlet; λ_{ex} = 410 nm). As shown in **Figure 4.1**H, the UV-Vis absorbance spectrum of the dispersion features three major bands with the first centered around 250 nm, the second at 420 nm and the last from 580 to 690 nm. The first band is assigned to the $\pi \rightarrow \pi^*$ transition of C=C bonds while the second and third bands can be respectively ascribed to the $\pi \rightarrow \pi^*$ and $n \rightarrow \pi^*$ transitions for the sp^2 domains containing C=O/C=N/C=S bonds, which are in agreement with XPS and FT-IR analyses. With multiple absorbance bands, the CDs can be excited with various wavelength in the blue and red regions of the spectrum. Upon excitation with a short wavelength of light (*i.e.* 405 nm), the CDs possess two fluorescence signatures in the blue and red regions of the spectrum. On the other hand, when

irradiated at a longer wavelength (*i.e.* 600 nm), the CDs emit solely in the red region of the spectrum. Such a phenomenon is postulated to be caused by carbon-core vs. molecular states fluorescence mechanism[60, 70] . Essentially, the blue component stems from the core, whereas the red originates from the surface. Being able to excite the dots at different wavelengths renders them attractive for a variety of applications. In this case, the red-to-red fluorescence is sought after for biological applications. At longer wavelengths (i.e. lower energy light), there is a lower interference brought about by biomolecular autofluorescence with minimal photo-damage and deeper tissue penetration.[189-191]

4.3.2. pH-Dependent Fluorescence

The as-synthesized CDs possess interesting pH-dependent fluorescence properties. The optical properties were studied as a function of pH following dispersion in DMEM buffer and the pH was adjusted using HCl or NaOH. The sensitivity stems principally from the red fluorescence. As shown in **Figure S4.2**, the quantum yield (at λ_{ex} = 405 nm) of the CDs is reported to be as high as 8.7%. With changes in pH, the blue component remains unchanged at a pH range of 3 to 11 (QY = 1.3-1.6%). Conversely, it is noted that the red component does not display significant variations at a pH range of 4 to 8 (QY = 6.9-7.1%). Although the efficiency of the red fluorescence remains unaffected, the appearance of a new band is highlighted in **Figure 4.1**I. When excited at a wavelength of 600 nm, the red fluorescence signature can be deconvoluted into two peaks, namely 650 nm and 680 nm. With an increase in pH, the peak at 650 nm dominates in intensity at the expense of the peak at 680 nm. The opposite effect is observed at lower pH values. **Figure 4.1**J highlights this relationship between the two peaks relative to the change in pH. The CDs displayed high sensitivity to changes in pH between 4 and 7, with a 16-fold difference in 680-to-650 peak ratio over this range. This is especially interesting for the detection of intracellular pH changes in endosomes, early and late lysosomes. The pH response exhibited by the CDs can be fitted in a sigmoidal curve, as shown in Equation 4.1 with an r^2 = 0.997. Therefore, such fluorescence changes this probe could be a potentially good candidate for pH-sensing.

Equation 4.1

$$y = 0.26 + \frac{15.69-0.26}{1+10^{-1.09(5.90-x)}}$$

This fluorescence behavior is thought to result from the chemical nature of the surface moieties found on the CDs, which can impact the electronic properties[41, 180] and are responsible for the 650 nm and 680 nm peaks. It is noted that following excitation at a wavelength of 405 nm **(Figure S4.3**), a similar pH-dependence behavior is observed in the red region of the spectrum, whereas the blue fluorescence shows no sensitivity towards changes in the environment's pH. The pH-dependent fluorescence signatures are associated to protonation/deprotonation of the amino/carboxylic groups[41] and the tautomerism of the amide, as demonstrated by *Pan et al*.[70] The robustness of the system was also studied through pH cycling experiments as shown in **Figure S4.4**. The pH reversibility experiments were carried out over multiple cycles between pH 2 and 10. At each extreme, the ratio of the intensities at 680 nm and 650 nm were measured and the results show the fluorescence is fully recoverable, showcasing the robustness of the system and its ability to withstand dramatic changes to the pH of the environment. In addition, it is noted that the CDs can be used to monitor changes in pH in the presence of metals and counter-ions, which do not induce any significant changes to the fluorescence. As shown in **Figure S4.5** and the literature,[113] the blue component of the CDs remains unaffected by the presence of possible interferences. On the other hand, the red fluorescence shows varying sensitivity towards certain ions, with high sensitivity towards heavy metals and very little sensitivity towards certain counter-ions including Na^+, Cl^-, K^+ and CO_3^{2-}. Moreover, all measurements were carried out in DMEM (Dulbecco's Modified Eagle Media), which is comprised of a myriad of inorganic salts ($CaCl_2$, ferric nitrate, KCl, NaCl, $MgSO_4$, $NaHCO_3$, and NaH_2PO_4) in addition to amino acids and vitamins. No shifts or changes in peak shape were observed in the red region of the spectrum in comparison to the CD dispersion in water (**Figure 4.1**H). This highlights the significant impact of the ratiometric approach over intensity-based measurements. Although the overall intensity in the red region of the spectrum may vary with the presence of certain ions, the ratio of the 680 nm and 650 nm peaks remains unchanged.

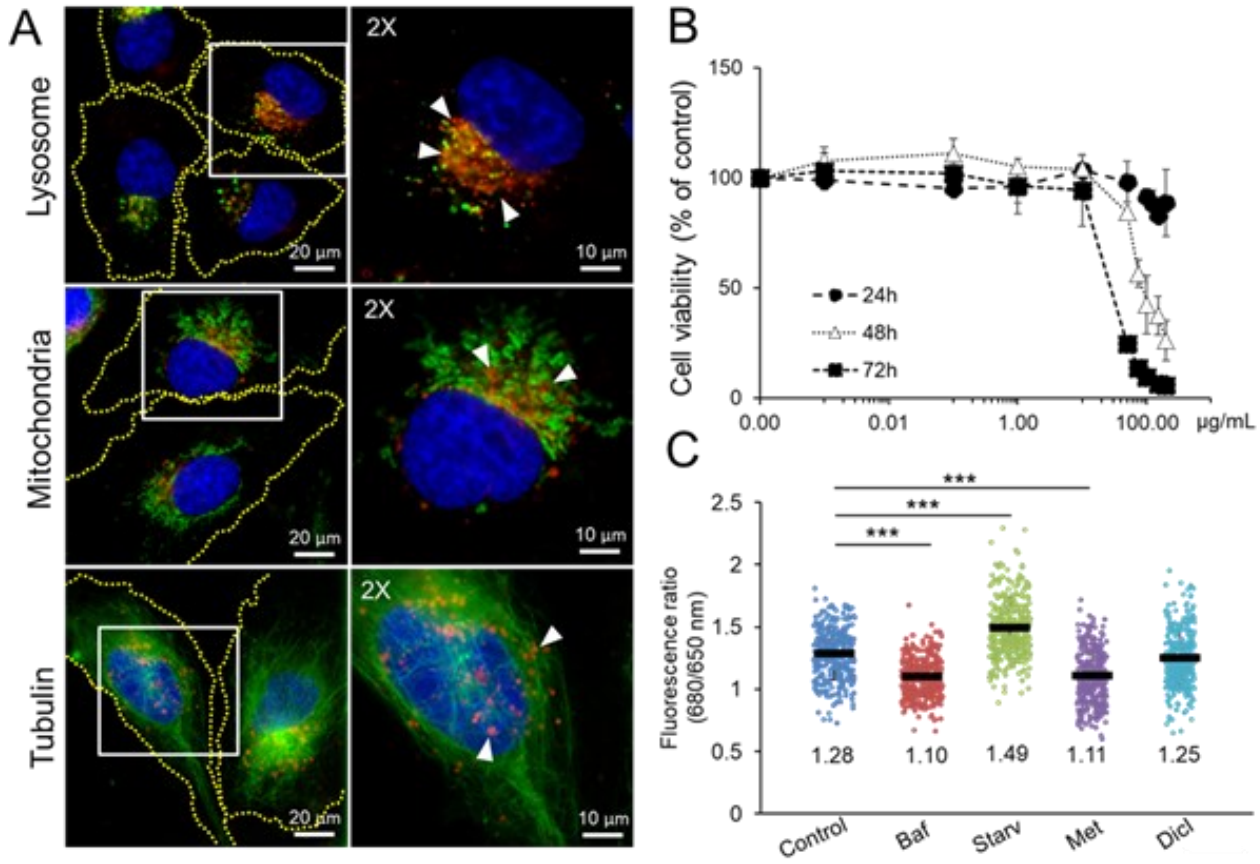

Figure 4.2 (A) Intracellular localization of carbon dots (red) in cells co-labeled for lysosomes, mitochondria or tubulin. Cell outlines are in yellow dotted lines; (B) Concentration- and time-dependent effect of carbon dots on glioblastoma cell viability. Cells were treated with carbon dots (1 ng/mL – 200 µg/mL) for 24h, 48h or 72h. Shown are average cell viabilities as (% of untreated control) ±SD from two independent experiments. At least 4700 cells were analyzed per experiment; (C) Carbon dots report changes in glioblastoma lysosomal pH in response to vacuolar ATPase inhibitor bafilomycin A1 (Baf, 50 nM, 30 minutes), serum and amino acid deprivation (Starv, 30 minutes), metformin (Met, 50 µM, 30 minutes) or diclofenac (Dicl, 50 µM, 30 minutes). Cells loaded with carbon dots for 24h (100 µg/mL) were treated with selected agents and imaged live using a confocal fluorescence microscope (ex: 638 nm). Shown are the ratio of fluorescence emission at 680 nm and 650 nm for individual cells. The average of each treatment group is indicated by a black horizontal bar ±SD. 330 cells were analyzed per group. (***$p<0.001$)

To investigate the use of CDs as pH sensors in living cells, we first determined the time- and concentration-dependent cytotoxicity of CDs in human glioblastoma cells (**Figure 4.2**A and B). We showed that concentrations up to 100 µg/mL did not significantly decrease cell viability within 24h (**Figure 4.2**B). CDs were mainly observed inside lysosomal compartments, with minimal co-

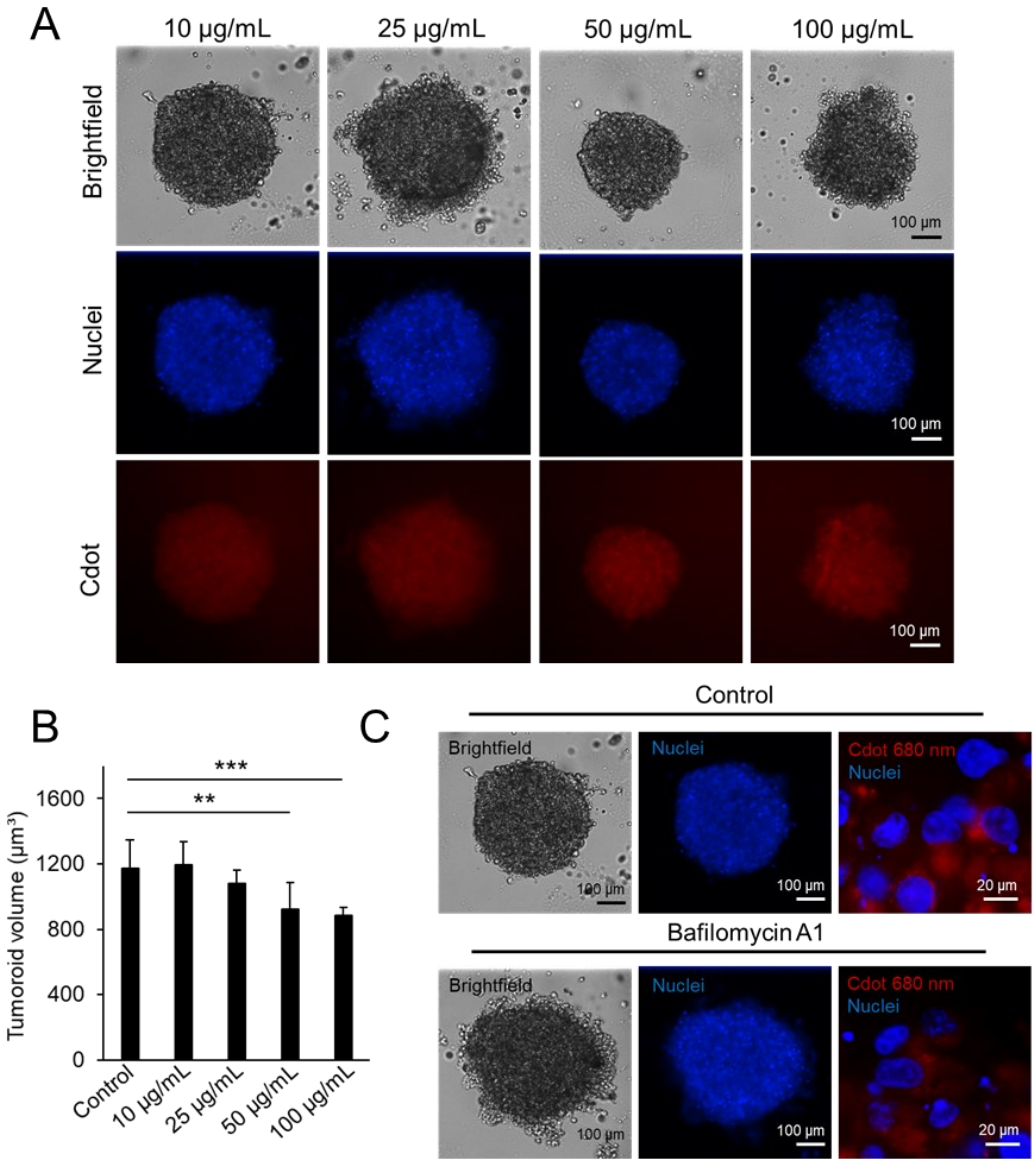

Figure 4.3 (A) Human glioblastoma tumoroid formation in the presence of increasing concentrations of carbon dots. Tumoroids were prepared using the liquid overlay method in agarose-coated wells in the presence or absence of carbon dots (10, 25, 50 100 µg/mL). Tumoroids were left to form over 4 days, after which nuclei were labeled with Hoechst 33342 and tumoroids were imaged using a brightfield and fluorescence microscope; (B) Size of human glioblastoma tumoroids formed from cells loaded with carbon dots (10, 25, 50, 100 µg/mL). Tumoroids were prepared as in A). The volume of each tumoroid was determined based on its surface area. Shown are average tumoroid volume (µm³) ±SD from at least two independent experiments. **p<0.01; ***p<0.001; (C) Carbon dots report changes in lysosomal pH in glioblastoma tumoroids. Tumoroids loaded with carbon dots (red, 10 µg/mL) were treated with bafilomycin A1 (50 nM, 30 minutes). Cells were imaged live using a fluorescence microscope and emission at 680 nm was recorded. Nuclei (blue) were labeled with Hoechst 33342.

localization with mitochondria or cytoskeletal structures (**Figure 4.2**A). Considering that different pharmacological agents – including anticancer drugs – bear carboxylic or amino moieties, we

investigated if and how much they change lysosomal pH. Anticancer weak acids are usually more advantageous than bases because they are not protonated in lysosomes or in the acidic tumor environment.[192] In the current study, we investigated the effect of metformin and diclofenac, which have very different pKa values (**Figure S4.6**A), on the lysosomal pH of human glioblastoma cells. Both drugs are FDA-approved and are currently in clinical trials for combination treatments in cancer. We used confocal microscopy to obtain ratiometric measurements from CDs in the lysosomes of living cells (**Figure 4.2**C). The vacuolar ATPase inhibitor bafilomycin A1 (Baf) was used as positive control to increase lysosomal pH.[193] The most marked changes in lysosomal pH were seen with serum and amino acid deprivation (Starv), which served as positive control for lysosomal acidification (**Figure 4.2**C and **Figure S4.6**C). Growth factors and amino acids are necessary to activate and recruit mTORC1 to lysosomes.[194] Their absence triggers autophagosome formation, increased vacuolar ATPase assembly and lysosomal acidification.[194, 195] Metformin (Met) has been commonly used as an effective antidiabetic agent, but several studies showed that it also exerts anticancer activity by inhibiting mitochondrial complex I, modulating lipogenesis and inhibiting P-glycoprotein.[196, 197] The increase in lysosomal pH observed with metformin (**Figure 4.2**C) was expected given its high pKa, yet the effect was modest due to the drug's low lipophilicity and slow, transporter-dependent uptake.[198] Diclofenac (Dicl) is a well-established anti-inflammatory agent with pKa = 4.15. It does not become protonated in lysosomes nor does it significantly affect lysosomal pH (**Figure 4.2**C).[199] Metformin and diclofenac did not affect glioblastoma viability at the concentration and time used (**Figure S4.6**B). To expand the use of CDs to 3D tumor models *in vitro*, we tested the uptake and fluorescence of carbon dots in glioblastoma tumoroids. CDs did not significantly interfere with tumoroid formation at concentrations <25 μg/mL (**Figure 4.3**A and B). Fluorescence was well distributed in the tumoroids and CDs responded to changes in lysosomal pH induced by bafilomycin A1 (**Figure 4.3**C).

4.4. Conclusion

In summary, we describe the synthesis and the characterization of fluorescent cell-compatible CDs. The as-synthesized CDs exhibit a unique dual-fluorescence character in the blue and red regions of the spectrum with a pH-dependent fluorescence behavior. This was exploited to develop a ratiometric pH sensor with high sensitivity at a pH range of 3 to 7. The biocompatible dots were

used to reveal changes in lysosomal pH, in living glioblastoma cells, induced by pharmacological agents and cellular stressors. The unique optical properties of the CDs described in this study offer suitable new nanotools to explore natural and pharmacological inducers of pH changes in living cells. CDs can report and measure these changes not only in simple cell cultures, but also in complex cell models such as tumoroids. More importantly, the proposed pH indicator benefits from a ratiometric fluorescence response that offers good reliability and reproducibility with less variability relative to conventional sensors that rely on intensity-based measurements.

4.5. Experimental Section

Chemicals and Reagents – Formamide (≥99.5%) and reduced L-glutathione (≥98.0%) were purchased from Thermo Scientific. All reagents were used without further modification or purification.

Synthesis of the Carbon Dots (CDs) – The CDs were prepared using a modified microwave-mediated one-step reaction with glutathione and formamide as previously reported.[70, 113, 116] The CDs were synthesized using a CEM Discover SP Microwave Reactor. A 20 mL solution of 0.1 M glutathione in formamide was prepared then sonicated for 15 minutes after which the solution turned clear. Subsequently, the solution was transferred to a 35 mL microwave vial and heated to 180°C for 5 minutes in the microwave. After the reaction, to remove unwanted material and impurities, the solution was dialyzed in Milli-Q water using a cellulose ester dialysis membrane (molecular weight cut-off: 3.5–5.0 kDa) with the water changed twice a day for 5 consecutive days. Afterwards, the solution was concentrated down using the rotovap. To further purify the dots, the samples were washed twice with acetone and twice with ethanol (1:10 volume ratio of sample:solvent). After each wash, the precipitate was collected by centrifugation at 10 000 x g for 10 minutes from which the supernatant was discarded. Finally, the pellet collected was put in an oven at 70°C overnight to dry.

Fluorescence Spectroscopy – Fluorescence spectra were acquired using a Cary Eclipse fluorescence spectrophotometer (Agilent Technologies). Spectra were acquired in a 10 mm quartz

cuvette at λ_{ex} = 360-660 nm (10 nm intervals). The excitation and emission slits were set to a width of 5 nm with a PMT voltage at 600 V. All data were processed using Cary Eclipse software. The spectra were background corrected for the solvent (i.e. Milli-Q water and buffers).

UV-Vis Absorbance Spectroscopy – UV-visible absorption spectra were acquired from 200-800 nm on a Cary 5 Series UV-Vis-NIR Spectrophotometer (Agilent Technologies) using a 1 cm quartz cuvette. A 5.0 nm bandwidth and wavelength changeover at 350 nm were used for analysis. Data was processed using Cary Eclipse software. The spectra were background corrected for the solvent (i.e. Milli-Q water or buffers).

Fluorescence Quantum Yield Measurements – Fluorescence quantum yield measurements were acquired on a FLS920 Fluorescence Spectrometer (Edinburgh Instruments) with an integrating sphere and a 1 cm quartz cuvette. The excitation and the emission slits were set to a width of 5 nm. The excitation wavelength was set to 405 nm and the spectra from 300-800 nm were collected. Scans were carried out in triplicates with a dwell time of 0.2 sec. Data was processed using the F900 Software.

Fourier-Transform Infrared Spectroscopy (FT-IR) – FT-IR spectra were collected using a Thermo Scientific Nicolet iS5 equipped with an iD5 ATR accessory. Approximately 20 μg of sample was used for each analysis. The spectra were collected using 32 scans with a resolution of 0.4 cm^{-1}, a gain of 1, an optical velocity 0.4747 and an aperture setting of 100. Data was processed using the Omnic 9 software.

X-ray Photoelectron Spectroscopy (XPS) – XPS spectra of the CDs were acquired using a Thermo Scientific K-Alpha X-Ray Photoelectron Spectrometer. Each analysis was carried out in triplicate with 10 runs for each scan; the high-resolution and survey scans represent the average of the triplicate measurements.

Transmission Electron Spectroscopy (TEM) – TEM Grids (3 mm, 200 mesh Formvar/carbon coated copper grid) were prepared by pipetting 2 mL of a 2 mg/mL dispersion of CD onto the surface followed by evaporation of the solvent. The TEM images were collected using a Jeol JEM-

2100F microscope operating at 100 kV. The images were processed and the carbon dot sizes were measured using the Fiji imaging software._ENREF_184

Cell culture – U251N human glioblastoma cells were originally obtained from the American Type Culture Collection. Unless otherwise indicated, cells were maintained in phenol red-containing Dulbecco's Modified Eagle Medium (DMEM; Thermo Fisher Scientific) supplemented with 5% (v/v) fetal bovine serum (FBS; Wisent) and 1% (v/v) penicillin-streptomycin (Thermo Fisher Scientific).

Cell viability – Cells were seeded at 5,000 cells per well in black 96-well plates (Corning) and left to adhere for 24h. Cells were then treated with increasing concentrations of carbon dots for 24h (0.001, 0.1, 1, 10, 50, 100, 125, 150, 200 μg/mL), 48h (0.001, 0.1, 1, 10, 50, 75, 100, 150, 200 μg/mL) or 72h (0.001, 0.1, 1, 10, 50, 75, 100, 150, 200 μg/mL). As control experiments, cells were treated with metformin (50 μM) and diclofenac (50 μM) for 30 minutes. Following treatment, cells were fixed with 4% (w/v) paraformaldehyde (10 minutes, BDH). Nuclei were labeled with Hoechst 33342 (10 μM, 10 minutes, Millipore Sigma). Cells were imaged using a fluorescence microscope (Leica DMI4000B) with a single-band filter (DAPI-1160A, Semrock). Cell numbers were counted.

Carbon Dot Imaging in Monolayer Cells – Cells were seeded into 35 mm cell culture dishes (Sarstedt) at 100,000 cells per plate and cultured for 24h. Cells were loaded with carbon dots (100 μg/mL) for 24h in phenol-free DMEM supplemented with 5% (v/v) FBS and 1% (v/v) penicillin-streptomycin, washed twice with phosphate buffered saline, then treated with bafilomycin A1 (50 nM, Millipore Sigma), serum- and amino acid-free solution (Hank's Balanced Salt Solution, Thermo Fisher Scientific), metformin (50 μM, Millipore Sigma) or diclofenac (50 μM, Millipore Sigma) for 30 minutes. Hoechst 33342 (1 μM) was added 30 minutes before imaging. Cells were imaged using a Leica SP8 confocal microscope with a 25X/0.95 immersion objective (Leica, 11506323). Nuclei were imaged using a two-photon laser at 720 nm. Carbon dots were excited using a 638 nm laser. Emission filters were set to 645-665 nm and 675-713 nm, for the 650 and 680 emission peaks, respectively. Sampling thickness was 1.039 μm and high sensitivity detectors were used.

Carbon Dot Imaging in Tumoroids – Cells were seeded at 5,000 cells per well into clear 96-well plates (Sarstedt) coated with 2% agarose (dissolved in DMEM). Carbon dots (10, 25, 50, 100 μg/mL) were added to cells and tumoroids were left to form over 4 days. Before treatment, nuclei were labeled with Hoechst 33342 (10 μM, 3h). Tumoroids were treated with bafilomycin A1 (50 nM) for 30 minutes, after which they were washed in phosphate buffered saline and imaged live using a brightfield and fluorescence microscope with single-band filters (Cy5-4040A for carbon dots and DAPI-1160A for Hoechst 33342, Semrock).

Organelle Labeling and Imaging – Cells were seeded on glass coverslips placed inside 12-well plates (Sarstedt). 5,000 cells were seeded per coverslip and left to adhere for 24h. Cells were loaded with carbon dots (100 μg/mL) for 24h in phenol-free DMEM supplemented with 5% (v/v) FBS and 1% (v/v) penicillin-streptomycin. Hoechst 33342 (1 μM) was added 30 minutes before imaging. For lysosomes, LysoTracker Green (50 nM, Thermo Fisher Scientific) was added 20 minutes before imaging. For tubulin, Tubulin Tracker Green (1X, Thermo Fisher Scientific) with Pluronic F-127 (0.005% v/v) was added 30 minutes before imaging. For mitochondria, MitoTracker Green (50 nM, Thermo Fisher Scientific) was added 20 minutes before imaging. At the end of treatment, cells were briefly washed in phosphate buffered saline and imaged live using a fluorescence microscope (Leica DMI4000B) with a GFP-3035B single-band filter (Semrock). Nuclei were imaged using a DAPI-1160A single-band filter. Cellular fluorescence was analyzed in the Fiji imaging software.

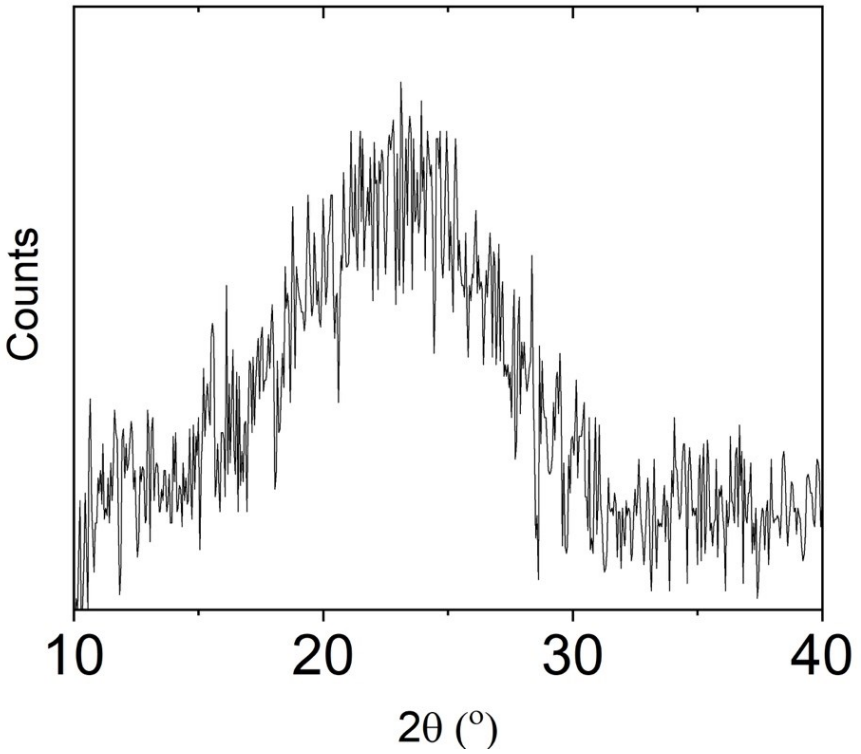

Figure S4.1 XRD profile of the CDs reveals an amorphous halo spanning 10 to 30 °2θ.

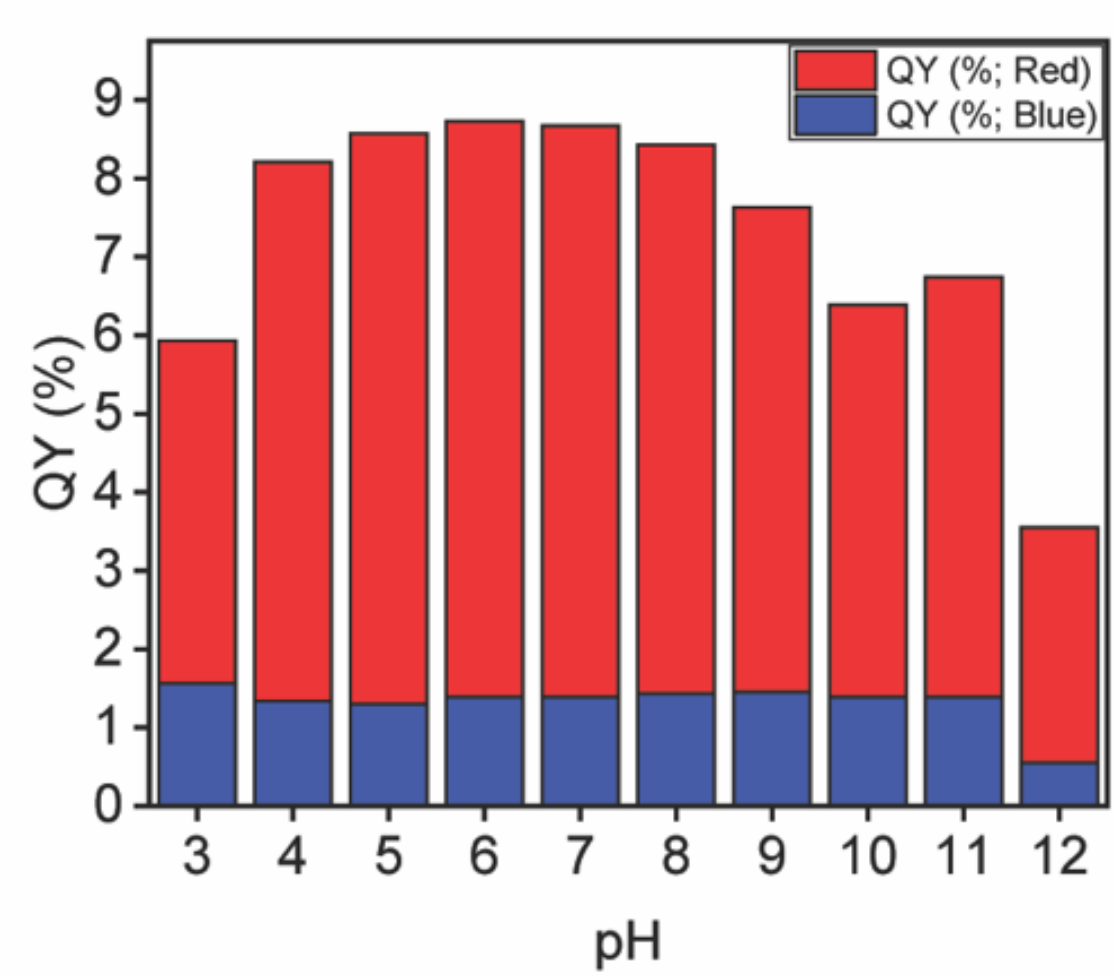

Figure S4.2 Quantum yields (λ_{ex} = 405 nm) of the CDs at different pH. It is noted the quantum yield of the blue component remains unaffected by the change in pH; the red component remains stable at a pH range of 4-8

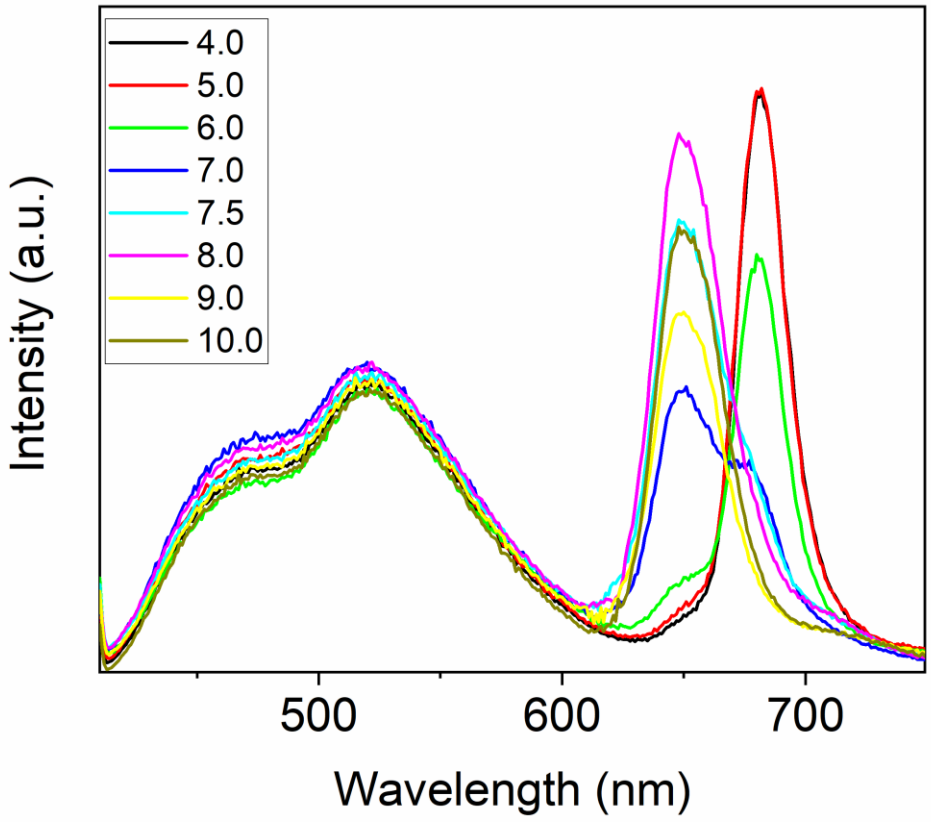

Figure S4.3 Fluorescence spectra of CDs following excitation at 405 nm. A change in the fluorescence signature is observed at 680 nm and 650 nm while the blue fluorescence shows no significant sensitivity towards changes in pH. It's noted that a shoulder peak at 520 nm stems from the fetal bovine serum in the DMEM buffer.

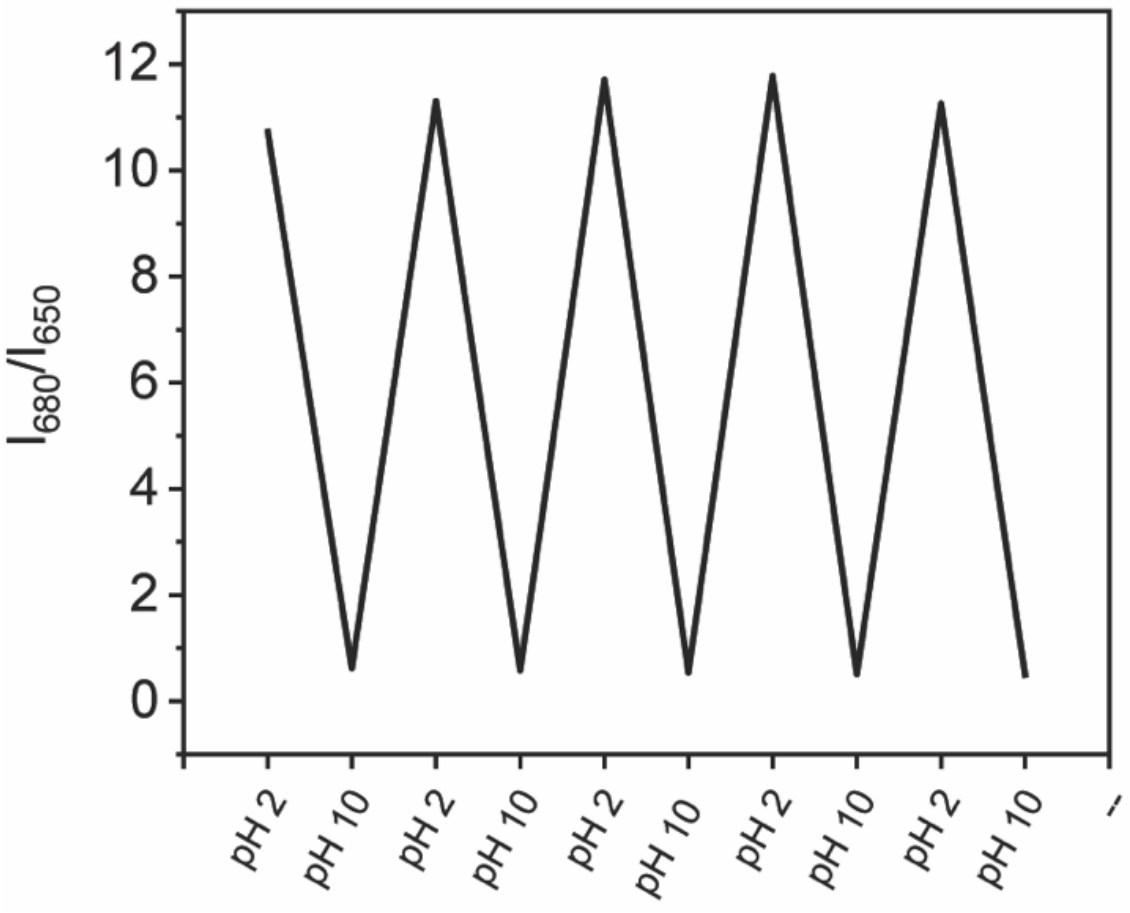

Figure S4.4 Reversibility experiment of CDs *via* pH cycling at pH 2 and pH 10. The CDs were dispersed in DMEM buffer and the pH was adjusted using HCl and NaOH

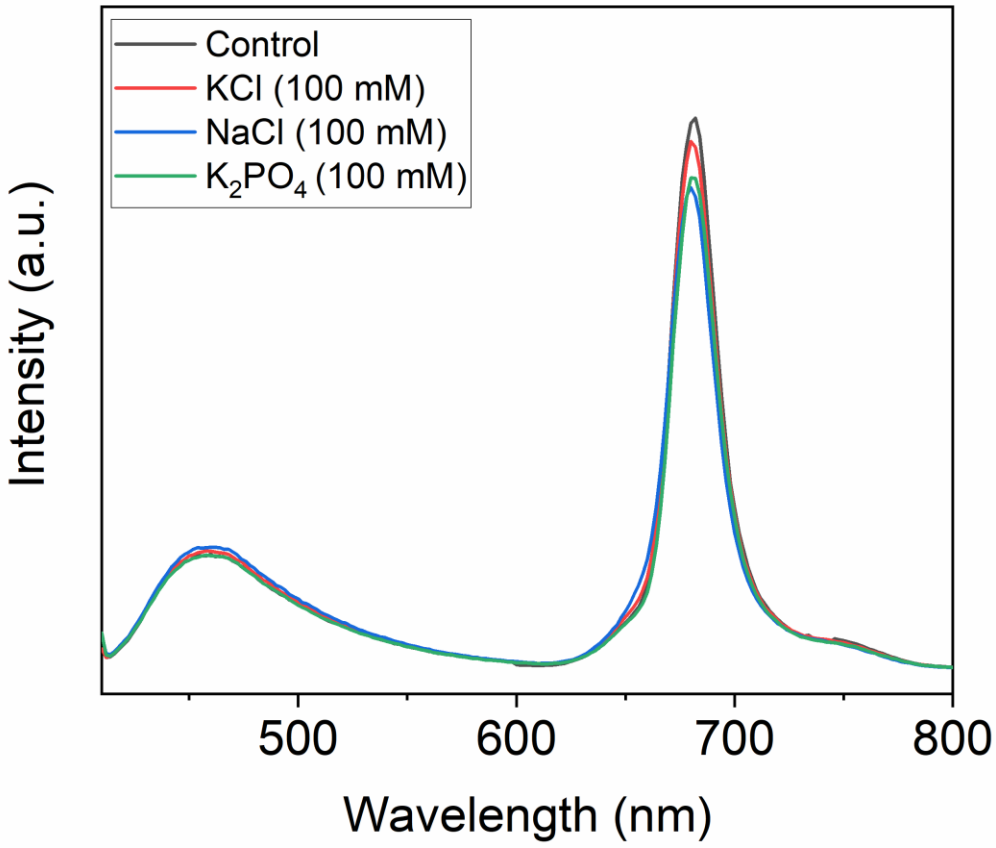

Figure S4.5 Fluorescence spectra of CDs following excitation at 405 nm in the presence of salts. The optical properties are measured as a function of the counter ion at high concentrations (100 mM). The shape of the fluorescence spectra remains unchanged and the blue component remains unaffected, while the overall intensity in the red fluorescence decreases by as much as 14%.

A

Name	pKa
Metformin	12.4
Diclofenac	4.15

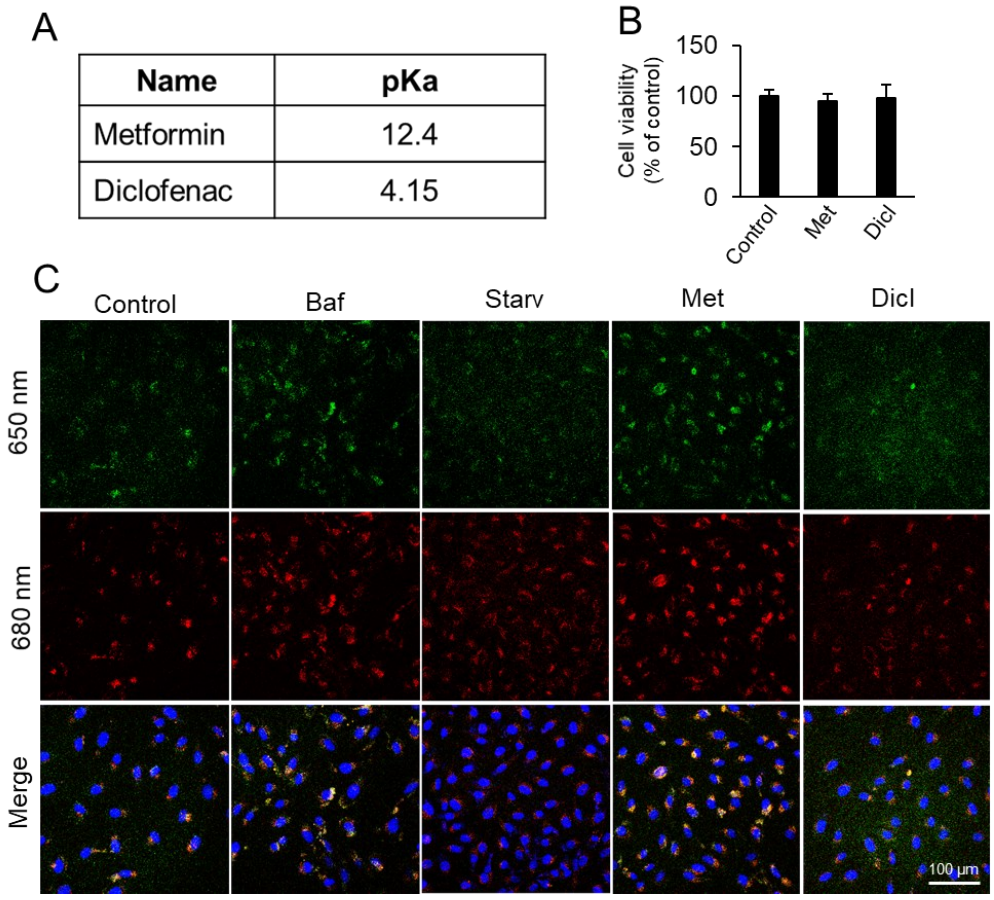

Figure S4.6 (A) pKa values of selected pharmacological agents; (B) Glioblastoma cell viability in response to metformin (Met, 50 µM) or diclofenac (Dicl, 50 µM) after 30 minutes. Shown are average cell viabilities as (% of untreated control) ±SD from two independent experiments. At least 13,000 cells were analyzed per experiment; (C) Representative fluorescence micrographs of carbon dots fluorescence at 650 nm and 680 nm in human glioblastoma cells. Cells loaded with carbon dots for 24h (100 µg/mL) were treated with bafilomycin A1 (Baf, 50 nM, 30 minutes), serum and amino acid deprivation (Starv, 30 minutes), metformin (Met, 50 µM, 30 minutes) or diclofenac (Dicl, 50 µM, 30 minutes) and imaged live using a confocal fluorescence microscope (ex: 638 nm). Nuclei were labeled with Hoechst 33342 (blue).

Chapter 5. Conclusions

With the focus on developing more accurate and efficient diagnostic techniques, this project aimed to further our knowledge in the development of imaging and sensing probes using carbon dots. With numerous interesting properties that are key for biological applications, coupled with their facile synthesis, CDs have drawn the attention of the scientific community for the development of bioimaging probes.

The CDs prepared in this work offer a unique multi-emissive behavior with a broad absorbance profile that is indicative of a system possessing multiple fluorescence centers. This intriguing optical property propelled us to shed light on the underlying fluorescence mechanism. The CDs were prepared using a solvothermal-mediated reaction using formamide and glutathione with varying reaction times. It was noted that longer times resulted in a weaker red fluorescence relative to the blue counterpart. It was postulated that the carbon core- and molecular-state fluorescence mechanism is at play. Each CD sample, synthesized at different reaction times, possessed relatively the same size. However, physical characterization techniques such as XPS and Raman spectroscopy evidenced that the sp^2-network of the dots was increasing as they further carbonized during synthesis. Therefore, the carbon core of the dots was responsible for the blue emission, while the red fluorescence originated from the molecular-states that were being consumed upon carbonization. To further elucidate the mechanism, electrochemical and ultrafast spectroscopic studies were carried out to study the dynamics of the photoexcited system. Both techniques emphasized the presence of two fluorescence centers and suggested that fluorescence can be triggered directly (i.e. excitation and emission in each state) and possibly through an energy transfer from the carbon core-state down to the molecular state.

Due to their prominent fluorescence bands in the blue and red region of the spectrum, we explored the possibility of utilizing the dots as a ratiometric diagnostic sensing tool to monitor real time changes in temperature. Unlike intensity-based measurements, ratiometric approaches offer more reliable measurements since they are concentration-independent and account for variability in the environment or instrumentation artefacts. As noted in Chapter 3, the red fluorescence is significantly more sensitive to the increase in temperature with very little change in the blue fluorescence, which in turn acts as reference. We postulate that this is related to an energy transfer of the two states (molecular and core) studied in Chapter 2. Due to our understanding of the

fundamentals relating to the fluorescence of the CDs, we were able to tailor its emission to maximize the red emission. Its sensing capabilities were first tested in a cuvette model; the red-to-blue ratio (λ_{ex} = 405 nm) offered a linear trend relative to changes in temperature. Following this, cell studies were performed on HeLa cell lines. The dots were biocompatible and were easily up-taken by the cells where they localized in the Golgi-ER network. Strikingly, when treating the cells with the dots, we were able to monitor the changes in temperature through changes in fluorescence intensity in the epifluorescence microscope. What is truly remarkable is that the linearity and accuracy of our temperature sensing work in the cell model parallels that of the cuvette.

Subsequently, the potential of using the dots to monitor another physiological parameter, pH, was explored. Although the red-to-blue ratio remained unchanged, it was noted that the shape of the red fluorescence would dramatically change upon variation of the pH of the medium. At higher pH values, we observed an increase in intensity at 650 nm and a decrease at 680 nm. Conversely, at lower pH values, the opposite was true. This fluorescence behavior was thought to result from the chemical nature of the surface moieties found on the CDs that can impact the electronic properties, as highlighted in Chapter 4. With these findings, the CDs were used to monitor changes in pH in glioblastoma cells. Unlike with HeLa cells, the dots localized in the lysosomal compartments of the glioblastoma cell. This discovery led us to investigate its use as a sensor to monitor the impact of anti-cancer drugs known to decrease the lysosomal pH of cancer cells. Our findings go hand-in-hand with the literature as we observed an increase in the 680-to-650 nm ratio, suggesting that the weak acid drugs decreased the lysosomal pH of the cells.

Our work has focused on the bottom up design and investigation of a nanomaterial touching on (i) synthesis, (ii) characterization, (iii) mechanistic studies, (iv) imaging and sensor probe design and (v) proof-of-concept demonstration. An iterative and often exhaustive approach allowed us hone our ability to finely tailor the optical properties of these nanoparticles. The work presented in this thesis demonstrates that CDs are suitable alternatives, relative to both conventional and nanoprobes, for fluorescence imaging. Moreover, their fluorescence properties can be exploited to harvest information on physiological parameters at subcellular resolution, which is not possible using conventional technologies. Our findings substantiate that working at the nanoscale provides many opportunities to further improve our current healthcare with superior diagnostic tools and that indeed, *there is plenty of room at the bottom*.

Chapter 6. Future Work

"Research is a learning process and learning never ends" – Dr. Shrabani Saha.

Although many objectives have been fulfilled and several questions were answered during the course of this research, doors have opened for additional lines of investigation. Thus, it is inevitable for one to ponder future work with the goal to further broaden our understanding about CDs and to explore different applications that can exploit their interesting properties.

With respect to cellular uptake, it would be interesting to study the localization (i.e. nucleus, Golgi-ER, cytoplasm, etc.) of the cellular uptake of different CDs in different cell lines (e.g. MCF-7, AC549, *etc*.). As shown in Chapters 3 and 4, the CDs used in this research localized in different regions of a cell depending on the cell line used. The cellular uptake mechanism will contribute to the elucidation of the endocytic pathway in which the CDs enter live cells (pinocytosis vs phagocytosis). We believe that these *in vitro* studies will shed light on the interaction between the CD surface and the cells further highlighting the importance of the surface composition of the dots.

Another idea consists of exploiting the uncommon red fluorescence of the prepared CDs. This can be utilized to develop a bimodal imaging probe for both fluorescence and magnetic resonance imaging. It would address the need of developing a multimodal imaging probe that would allow for harvesting a multitude of information otherwise inaccessible using a single imaging modality. To the best of our knowledge, there are very few reports on bimodal imaging probes using CDs, let alone CDs for deep-red fluorescence and magnetic resonance imaging (current CD-based bimodal probes fluoresce up to 610 nm)[200]. This work has already been initiated in the Naccache group.

To investigate the possibility of developing such bimodal imaging nanotools, gadolinium ions (Gd^{3+}) will be incorporated, which would endow the CDs with magnetic properties. The incorporation of the trivalent lanthanide can be carried out in a two-pronged approach: (i) in a one-step synthesis and (ii) using post-synthetic modifications using chelators (i.e. DTPA) in hopes to enhance the magnetic properties of the system. Knowing the propensity of metallic cations to quench fluorescence and induce aggregation in CDs, the first proposed method may not be ideal. Nevertheless, it is necessary to study the interaction between CDs and the metallic ions to

understand the quenching mechanism at play (i.e. dynamic or static quenching). The second approach is proposed with aims of mitigating the limitations introduced by the addition of these metallic ions. Based on early data generated in our laboratory, functionalizing CDs with chelators minimizes the impact of Gd^{3+}-incorporation on fluorescence and aggregation. However, functionalizing the surface with chelators also hinders the fluorescence property of the dots (albeit not to the same extent as metallic ion quenchers). Therefore, it will be necessary to assess the optimal reaction conditions determined through optical and magnetic characterization. In addition, it would be interesting to study the use of different paramagnetic ions such as manganese. Since these dots will be used in a biological system, it will be important to study the stability of the formed complex through transmetallation and leaching experiments as free metallic ions can hinder biological processes. Once the preparation of the functionalized CDs has been optimized, the performance of its fluorescence and magnetic properties can be tested for *in vitro* and *in vivo* imaging.

References

1. Ding, H.; Yu, S.-B.; Wei, J.-S.; Xiong, H.-M., *ACS Nano* **2016,** *10* (1), 484-491.
2. Zhang, Y.; Yuan, R.; He, M.; Hu, G.; Jiang, J.; Xu, T.; Zhou, L.; Chen, W.; Xiang, W.; Liang, X., *Nanoscale* **2017,** *9* (45), 17849-17858.
3. Sumanth Kumar, D.; Jai Kumar, B.; Mahesh, H. M., Chapter 3 - Quantum Nanostructures (QDs): An Overview. In *Synthesis of Inorganic Nanomaterials*, Mohan Bhagyaraj, S.; Oluwafemi, O. S.; Kalarikkal, N.; Thomas, S., Eds. Woodhead Publishing: 2018; pp 59-88.
4. Wallyn, J.; Anton, N.; Akram, S.; Vandamme, T. F., *Pharm. Res.* **2019,** *36* (6), 78.
5. Power, S. P.; Moloney, F.; Twomey, M.; James, K.; O'Connor, O. J.; Maher, M. M., *World Journal of Radiology* **2016,** *8* (12), 902-915.
6. International Conference on Production, E.; Seiki, G.; International Institution for Production Engineering, R. In *Proceedings of the International Conference on Production Engineering, Tokyo, 1974*.
7. Kruizinga, P.; van der Meulen, P.; Fedjajevs, A.; Mastik, F.; Springeling, G.; de Jong, N.; Bosch, J. G.; Leus, G., *Sci. Adv.* **2017,** *3* (12), e1701423.
8. Luo, P. G.; Sahu, S.; Yang, S.-T.; Sonkar, S. K.; Wang, J.; Wang, H.; LeCroy, G. E.; Cao, L.; Sun, Y.-P., *J. Mater. Chem. B* **2013,** *1* (16), 2116-2127.
9. Bhunia, S. K.; Saha, A.; Maity, A. R.; Ray, S. C.; Jana, N. R., *Sci. Rep.* **2013,** *3*.
10. Grover, V. P. B.; Tognarelli, J. M.; Crossey, M. M. E.; Cox, I. J.; Taylor-Robinson, S. D.; McPhail, M. J. W., *J. Clin. Exp. Hepatol.* **2015,** *5* (3), 246-255.
11. Ghoroghchian, P. P.; Therien, M. J.; Hammer, D. A., *Wiley Interdiscip. Rev. Nanomed. Nanobiotechnol.* **2009,** *1* (2), 156-167.
12. Rao, J.; Dragulescu-Andrasi, A.; Yao, H., *Curr. Opin. Biotechnol.* **2007,** *18* (1), 17-25.
13. Escobedo, J. O.; Rusin, O.; Lim, S.; Strongin, R. M., *Curr. Opin. Chem. Biol.* **2010,** *14* (1), 64-70.
14. Resch-Genger, U.; Grabolle, M.; Cavaliere-Jaricot, S.; Nitschke, R.; Nann, T., *Nat. Methods* **2008,** *5*, 763.
15. Zsigmondy, R. A.; Alexander, J., *Colloids and the Ultramicroscope; A Manual of Colloid Chemistry and Ultramicroscopy*. J. Wiley & Sons; New York, **1909**; p xiii, 245 p.
16. Hulla, J. E.; Sahu, S. C.; Hayes, A. W., *Hum. Exp. Toxicol.* **2015,** *34* (12), 1318-1321.
17. Alsaba, M. T.; Al Dushaishi, M. F.; Abbas, A. K., *J. Pet. Explor. Prod. Technol.* **2020,** *10* (4), 1389-1399.
18. Mahmoudi, M.; Sant, S.; Wang, B.; Laurent, S.; Sen, T., *Adv. Drug Deliv. Rev.* **2011,** *63* (1), 24-46.
19. Wahajuddin; Arora, S., *Int. J. Nanomedicine* **2012,** *7*, 3445-3471.
20. Palanisamy, S.; Wang, Y.-M., *Dalton Trans.* **2019,** *48* (26), 9490-9515.
21. Gupta, H.; Paul, P.; Kumar, N., *Procedia Materials Science* **2014,** *5*, 198-203.
22. Tyagi, A.; Tripathi, K. M.; Singh, N.; Choudhary, S.; Gupta, R. K., *RSC Adv.* **2016,** *6* (76), 72423-72432.
23. Prakash Sharma, V.; Sharma, U.; Chattopadhyay, M.; Shukla, V. N., *Materials Today: Proceedings* **2018,** *5* (2, Part 1), 6376-6380.
24. Pratiwi, F. W.; Kuo, C. W.; Wu, S. H.; Chen, Y. P.; Mou, C. Y.; Chen, P., *The Enzymes* **2018,** *43*, 123-153.
25. Jafari, S.; Derakhshankhah, H.; Alaei, L.; Fattahi, A.; Varnamkhasti, B. S.; Saboury, A. A., *Biomed. Pharmacother.* **2019,** *109*, 1100-1111.

26. Geszke-Moritz, M.; Moritz, M., *Mater. Sci. Eng., C* **2013,** *33* (3), 1008-1021.
27. Reshma, V. G.; Mohanan, P. V., *J. Lumin.* **2019,** *205*, 287-298.
28. Geoffrion, L. D.; Guisbiers, G., *J. Phys. Chem. Solids* **2020,** *140*, 109320.
29. Wu, Q.; Zhi, L.; Qu, Y.; Wang, D., *Nanomedicine: Nanotechnology, Biology and Medicine* **2016,** *12* (5), 1175-1184.
30. Chen, G.; Qiu, H.; Prasad, P. N.; Chen, X., *Chem. Rev.* **2014,** *114* (10), 5161-5214.
31. Dong, H.; Du, S.-R.; Zheng, X.-Y.; Lyu, G.-M.; Sun, L.-D.; Li, L.-D.; Zhang, P.-Z.; Zhang, C.; Yan, C.-H., *Chem. Rev.* **2015,** *115* (19), 10725-10815.
32. Gnach, A.; Lipinski, T.; Bednarkiewicz, A.; Rybka, J.; Capobianco, J. A., *Chem. Soc. Rev.* **2015,** *44* (6), 1561-1584.
33. Xu, X.; Ray, R.; Gu, Y.; Ploehn, H. J.; Gearheart, L.; Raker, K.; Scrivens, W. A., *J. Am. Chem. Soc.* **2004,** *126* (40), 12736-12737.
34. Hola, K.; Zhang, Y.; Wang, Y.; Giannelis, E. P.; Zboril, R.; Rogach, A. L., *Nano Today* **2014,** *9* (5), 590-603.
35. Baker, S. N.; Baker, G. A., *Angew. Chem., Int. Ed.* **2010,** *49* (38), 6726-6744.
36. Sahu, S.; Behera, B.; Maiti, T. K.; Mohapatra, S., *Chem. Commun.* **2012,** *48* (70), 8835-8837.
37. Liu, H.; Ye, T.; Mao, C., *Angew. Chem., Int. Ed.* **2007,** *46* (34), 6473-6475.
38. Wang, L.; Zhou, H. S., *Anal. Chem.* **2014,** *86* (18), 8902-8905.
39. Wang, D.; Wang, X.; Guo, Y.; Liu, W.; Qin, W., *RSC Adv.* **2014,** *4* (93), 51658-51665.
40. Sharma, V.; Tiwari, P.; Mobin, S. M., *J. Mater. Chem. B* **2017,** *5* (45), 8904-8924.
41. Dhenadhayalan, N.; Lin, K.-C.; Suresh, R.; Ramamurthy, P., *J. Phys. Chem. C* **2016,** *120* (2), 1252-1261.
42. Cailotto, S.; Amadio, E.; Facchin, M.; Selva, M.; Pontoglio, E.; Rizzolio, F.; Riello, P.; Toffoli, G.; Benedetti, A.; Perosa, A., *ACS Med. Chem. Lett.* **2018,** *9* (8), 832-837.
43. Peng, H.; Travas-Sejdic, J., *Chem. Mater.* **2009,** *21* (23), 5563-5565.
44. Cheng, H.-J.; Kao, C.-L.; Chen, Y.-F.; Huang, P.-C.; Hsu, C.-Y.; Kuei, C.-H., *Microchim. Acta* **2017,** *184* (9), 3179-3187.
45. Manioudakis, J.; Victoria, F.; Thompson, C. A.; Brown, L.; Movsum, M.; Lucifero, R.; Naccache, R., *J. Mater. Chem. C* **2019,** *7* (4), 853-862.
46. de Medeiros, T. V.; Manioudakis, J.; Noun, F.; Macairan, J.-R.; Victoria, F.; Naccache, R., *J. Mater. Chem. C* **2019,** *7* (24), 7175-7195.
47. Lim, S. Y.; Shen, W.; Gao, Z., *Chem. Soc. Rev.* **2015,** *44* (1), 362-381.
48. Alina, A. K.; Ekaterina, S. P.; Gleb, B. S.; Andrei, V. S.; Irina Yu, G., *Russian Chem. Rev.* **2017,** *86* (11), 1157.
49. Shen, J.; Zhu, Y.; Yang, X.; Zong, J.; Zhang, J.; Li, C., *New J. Chem.* **2012,** *36* (1), 97-101.
50. Sun, Y.-P.; Zhou, B.; Lin, Y.; Wang, W.; Fernando, K. A. S.; Pathak, P.; Meziani, M. J.; Harruff, B. A.; Wang, X.; Wang, H.; Luo, P. G.; Yang, H.; Kose, M. E.; Chen, B.; Veca, L. M.; Xie, S.-Y., *J. Am. Chem. Soc.* **2006,** *128* (24), 7756-7757.
51. Liu, M.; Xu, Y.; Niu, F.; Gooding, J. J.; Liu, J., *Analyst* **2016,** *141* (9), 2657-64.
52. Bao, L.; Zhang, Z.-L.; Tian, Z.-Q.; Zhang, L.; Liu, C.; Lin, Y.; Qi, B.; Pang, D.-W., *Adv. Mater.* **2011,** *23* (48), 5801-5806.
53. Konstantinos, D., *Curr. Org. Chem.* **2016,** *20* (6), 682-695.
54. Dong, Y.; Zhou, N.; Lin, X.; Lin, J.; Chi, Y.; Chen, G., *Chem. Mater.* **2010,** *22* (21), 5895-5899.
55. Dang, H.; Huang, L.-K.; Zhang, Y.; Wang, C.-F.; Chen, S., *Ind. Eng. Chem. Res.* **2016,** *55* (18), 5335-5341.

56. Qu, D.; Zheng, M.; Du, P.; Zhou, Y.; Zhang, L.; Li, D.; Tan, H.; Zhao, Z.; Xie, Z.; Sun, Z., *Nanoscale* **2013,** *5* (24), 12272-12277.
57. Zhai, X.; Zhang, P.; Liu, C.; Bai, T.; Li, W.; Dai, L.; Liu, W., *Chem. Commun.* **2012,** *48* (64), 7955-7957.
58. Xu, M.; He, G.; Li, Z.; He, F.; Gao, F.; Su, Y.; Zhang, L.; Yang, Z.; Zhang, Y., *Nanoscale* **2014,** *6* (17), 10307-10315.
59. Bourlinos, A. B.; Stassinopoulos, A.; Anglos, D.; Zboril, R.; Georgakilas, V.; Giannelis, E. P., *Chem. Mater.* **2008,** *20* (14), 4539-4541.
60. Zhu, S.; Song, Y.; Zhao, X.; Shao, J.; Zhang, J.; Yang, B., *Nano Res.* **2015,** *8* (2), 355-381.
61. Zhu, H.; Wang, X.; Li, Y.; Wang, Z.; Yang, F.; Yang, X., *Chem. Commun.* **2009,** (34), 5118-5120.
62. de Medeiros, T. V.; Naccache, R., Near Infrared-Emitting Carbon Nanomaterials for Biomedical Applications. In *Near Infrared-Emitting Nanoparticles for Biomedical Applications*, Benayas, A.; Hemmer, E.; Hong, G.; Jaque, D., Eds. Springer International Publishing: Cham, 2020; pp 133-161.
63. Fang, Y.; Guo, S.; Li, D.; Zhu, C.; Ren, W.; Dong, S.; Wang, E., *ACS Nano* **2012,** *6* (1), 400-409.
64. Wang, Z.; Long, P.; Feng, Y.; Qin, C.; Feng, W., *RSC Adv.* **2017,** *7* (5), 2810-2816.
65. Pan, L.; Sun, S.; Zhang, A.; Jiang, K.; Zhang, L.; Dong, C.; Huang, Q.; Wu, A.; Lin, H., *Adv. Mater.* **2015,** *27* (47), 7782-7.
66. Hu, S., *Chem. Rec.* **2016,** *16* (1), 219-30.
67. Guo, L.; Ge, J.; Liu, W.; Niu, G.; Jia, Q.; Wang, H.; Wang, P., *Nanoscale* **2016,** *8* (2), 729-34.
68. Huiquan, T.; Kai, Y.; Zhen, M.; Jianmei, W.; Youjiu, Z.; Zhenhui, K.; Zhuang, L., *Small* **2012,** *8* (2), 281-290.
69. Ko, H. Y.; Chang, Y. W.; Paramasivam, G.; Jeong, M. S.; Cho, S.; Kim, S., *Chem. Commun.* **2013,** *49* (87), 10290-10292.
70. Pan, L.; Sun, S.; Zhang, L.; Jiang, K.; Lin, H., *Nanoscale* **2016,** *8* (39), 17350-17356.
71. Holá, K.; Sudolská, M.; Kalytchuk, S.; Nachtigallová, D.; Rogach, A. L.; Otyepka, M.; Zbořil, R., *ACS Nano* **2017**.
72. Wang, H.; Sun, C.; Chen, X.; Zhang, Y.; Colvin, V. L.; Rice, Q.; Seo, J.; Feng, S.; Wang, S.; Yu, W. W., *Nanoscale* **2017,** *9* (5), 1909-1915.
73. Dong, Y.; Pang, H.; Yang, H. B.; Guo, C.; Shao, J.; Chi, Y.; Li, C. M.; Yu, T., *Angew. Chem., Int. Ed.* **2013,** *52* (30), 7800-7804.
74. Chen, D.; Wu, W.; Yuan, Y.; Zhou, Y.; Wan, Z.; Huang, P., *J. Mater. Chem. C* **2016,** *4* (38), 9027-9035.
75. Liu, M. L.; Yang, L.; Li, R. S.; Chen, B. B.; Liu, H.; Huang, C. Z., *Green Chem.* **2017,** *19* (15), 3611-3617.
76. Jiang, K.; Feng, X.; Gao, X.; Wang, Y.; Cai, C.; Li, Z.; Lin, H., *Nanomat. (Basel)* **2019,** *9* (4), 529.
77. Bhattacharya, A.; Chatterjee, S.; Prajapati, R.; Mukherjee, T. K., *Phys. Chem. Chem. Phys.* **2015,** *17* (19), 12833-40.
78. Gan, Z.; Xu, H.; Hao, Y., *Nanoscale* **2016,** *8* (15), 7794-7807.
79. Sk, M. A.; Ananthanarayanan, A.; Huang, L.; Lim, K. H.; Chen, P., *J. Mater. Chem. C* **2014,** *2* (34), 6954-6960.

80. Tian, Z.; Zhang, X.; Li, D.; Zhou, D.; Jing, P.; Shen, D.; Qu, S.; Zboril, R.; Rogach, A. L., *Adv. Opt. Mater.* **2017,** *5* (19), 1700416.
81. Li, H.; He, X.; Kang, Z.; Huang, H.; Liu, Y.; Liu, J.; Lian, S.; Tsang, C. H. A.; Yang, X.; Lee, S.-T., *Angew. Chem., Int. Ed.* **2010,** *49* (26), 4430-4434.
82. Yu, P.; Wen, X.; Toh, Y.-R.; Tang, J., *J. Phys. Chem. C* **2012,** *116* (48), 25552-25557.
83. Miao, X.; Qu, D.; Yang, D.; Nie, B.; Zhao, Y.; Fan, H.; Sun, Z., *Adv. Mater.* **2018,** *30* (1), 1704740 (1-8).
84. Nie, H.; Li, M.; Li, Q.; Liang, S.; Tan, Y.; Sheng, L.; Shi, W.; Zhang, S. X.-A., *Chem. Mater.* **2014,** *26* (10), 3104-3112.
85. Shoujun, Z.; Qingnan, M.; Lei, W.; Junhu, Z.; Yubin, S.; Han, J.; Kai, Z.; Hongchen, S.; Haiyu, W.; Bai, Y., *Angew. Chem., Int. Ed.* **2013,** *52* (14), 3953-3957.
86. Shamsipur, M.; Barati, A.; Taherpour, A. A.; Jamshidi, M., *J. Phys. Chem. Lett.* **2018,** *9* (15), 4189-4198.
87. Krysmann, M. J.; Kelarakis, A.; Dallas, P.; Giannelis, E. P., *J. Am. Chem. Soc.* **2012,** *134* (2), 747-750.
88. Lu, S.; Sui, L.; Liu, J.; Zhu, S.; Chen, A.; Jin, M.; Yang, B., *Adv. Mater.* **2017,** *29* (15), 1603443-n/a.
89. Ding, H.; Cheng, L.-W.; Ma, Y.-Y.; Kong, J.-L.; Xiong, H.-M., *New J. Chem.* **2013,** *37* (8).
90. Konar, S.; Kumar, B. N. P.; Mahto, M. K.; Samanta, D.; Shaik, M. A. S.; Shaw, M.; Mandal, M.; Pathak, A., *Sens. Actuators, B* **2019,** *286*, 77-85.
91. Vasimalai, N.; Vilas-Boas, V.; Gallo, J.; Cerqueira, M. d. F.; Menéndez-Miranda, M.; Costa-Fernández, J. M.; Diéguez, L.; Espiña, B.; Fernández-Argüelles, M. T., *Beilstein J. Nanotechnol.* **2018,** *9*, 530-544.
92. Kumar, A.; Chowdhuri, A. R.; Laha, D.; Mahto, T. K.; Karmakar, P.; Sahu, S. K., *Sens. Actuators, B* **2017,** *242*, 679-686.
93. Ding, H.; Wei, J.-S.; Zhong, N.; Gao, Q.-Y.; Xiong, H.-M., *Langmuir* **2017,** *33* (44), 12635-12642.
94. Chen, J.; Wei, J.-S.; Zhang, P.; Niu, X.-Q.; Zhao, W.; Zhu, Z.-Y.; Ding, H.; Xiong, H.-M., *ACS Appl. Mater. Interfaces* **2017,** *9* (22), 18429-18433.
95. Sun, S.; Zhang, L.; Jiang, K.; Wu, A.; Lin, H., *Chem. Mater.* **2016,** *28* (23), 8659-8668.
96. Mohammed, L. J.; Omer, K. M., *Nanoscale Res. Lett.* **2020,** *15* (1), 182.
97. Jiang, J.; He, Y.; Li, S.; Cui, H., *Chem. Commun.* **2012,** *48* (77), 9634-9636.
98. Wang, Z.; Fu, B.; Zou, S.; Duan, B.; Chang, C.; Yang, B.; Zhou, X.; Zhang, L., *Nano Res.* **2016,** *9* (1), 214-223.
99. Chahal, S.; Yousefi, N.; Tufenkji, N., *ACS Sustainable Chem. Eng.* **2020**.
100. Macairan, J.-R.; Zhang, I.; Clermont-Paquette, A.; Naccache, R.; Maysinger, D., *Part. Part. Syst. Charact.* **2020,** *37* (1), 1900430.
101. Li, H.; Kang, Z.; Liu, Y.; Lee, S.-T., *J. Mater. Chem.* **2012,** *22* (46), 24230-24253.
102. Tuerhong, M.; Xu, Y.; Yin, X.-B., *Chinese J. Anal. Chem.* **2017,** *45* (1), 139-150.
103. Liu, M. L.; Chen, B. B.; Li, C. M.; Huang, C. Z., *Green Chem.* **2019,** *21* (3), 449-471.
104. Hu, S.; Trinchi, A.; Atkin, P.; Cole, I., *Angew. Chem., Int. Ed.* **2015,** *54* (10), 2970-2974.
105. Hu, Y.; Yang, J.; Tian, J.; Yu, J.-S., *J. Mater. Chem. B* **2015,** *3* (27), 5608-5614.
106. Bourlinos, A. B.; Zbořil, R.; Petr, J.; Bakandritsos, A.; Krysmann, M.; Giannelis, E. P., *Chem. Mater.* **2012,** *24* (1), 6-8.
107. Nguyen, H. A.; Srivastava, I.; Pan, D.; Gruebele, M., *ACS Nano* **2020**.

108. Ortega-Liebana, M. C.; Chung, N. X.; Limpens, R.; Gomez, L.; Hueso, J. L.; Santamaria, J.; Gregorkiewicz, T., *Carbon* **2017,** *117*, 437-446.
109. Dekaliuk, M. O.; Viagin, O.; Malyukin, Y. V.; Demchenko, A. P., *Phys. Chem. Chem. Phys.* **2014,** *16* (30), 16075-16084.
110. Sciortino, A.; Cayuela, A.; Soriano, M. L.; Gelardi, F. M.; Cannas, M.; Valcárcel, M.; Messina, F., *Phys. Chem. Chem. Phys.* **2017,** *19* (34), 22670-22677.
111. Song, Y.; Zhu, S.; Xiang, S.; Zhao, X.; Zhang, J.; Zhang, H.; Fu, Y.; Yang, B., *Nanoscale* **2014,** *6* (9), 4676-4682.
112. Shi, L.; Yang, J. H.; Zeng, H. B.; Chen, Y. M.; Yang, S. C.; Wu, C.; Zeng, H.; Yoshihito, O.; Zhang, Q., *Nanoscale* **2016,** *8* (30), 14374-14378.
113. Yarur, F.; Macairan, J.-R.; Naccache, R., *Environ. Sci.: Nano* **2019,** *6* (4), 1121-1130.
114. Sciortino, A.; Marino, E.; Dam, B. v.; Schall, P.; Cannas, M.; Messina, F., *J. Phys. Chem. Lett.* **2016,** *7* (17), 3419-3423.
115. Righetto, M.; Privitera, A.; Fortunati, I.; Mosconi, D.; Zerbetto, M.; Curri, M. L.; Corricelli, M.; Moretto, A.; Agnoli, S.; Franco, L.; Bozio, R.; Ferrante, C., *J. Phys. Chem. Lett.* **2017,** *8* (10), 2236-2242.
116. Macairan, J.-R.; Jaunky, D. B.; Piekny, A.; Naccache, R., *Nanoscale Adv.* **2019,** *1* (1), 105-113.
117. Joseph, J.; Anappara, A. A., *J. Lumin.* **2017,** *192*, 761-766.
118. Song, Y.; Zhu, S.; Zhang, S.; Fu, Y.; Wang, L.; Zhao, X.; Yang, B., *J. Mater. Chem. C* **2015,** *3* (23), 5976-5984.
119. Misra, S. K.; Srivastava, I.; Khamo, J. S.; Krishnamurthy, V. V.; Sar, D.; Schwartz-Duval, A. S.; Soares, J. A. N. T.; Zhang, K.; Pan, D., *Nanoscale* **2018,** *10* (39), 18510-18519.
120. Dervishi, E.; Ji, Z.; Htoon, H.; Sykora, M.; Doorn, S. K., *Nanoscale* **2019,** *11* (35), 16571-16581.
121. Hola, K.; Bourlinos, A. B.; Kozak, O.; Berka, K.; Siskova, K. M.; Havrdova, M.; Tucek, J.; Safarova, K.; Otyepka, M.; Giannelis, E. P.; Zboril, R., *Carbon* **2014,** *70*, 279-286.
122. Hsu, P.-C.; Chang, H.-T., *Chem. Commun.* **2012,** *48* (33), 3984-3986.
123. Wang, W.; Damm, C.; Walter, J.; Nacken, T. J.; Peukert, W., *Phys. Chem. Chem. Phys.* **2016,** *18* (1), 466-475.
124. Nguyen, V.; Si, J.; Yan, L.; Hou, X., *Carbon* **2015,** *95*, 659-663.
125. Lakowicz, J. R., *Principles of Fluorescence Spectroscopy*. Second edition. New York : Kluwer Academic/Plenum, [1999].
126. Suzuki, M.; Tseeb, V.; Oyama, K.; Ishiwata, S., *Biophysical Journal* **2007,** *92* (6), L46-L48.
127. Zohar, O.; Ikeda, M.; Shinagawa, H.; Inoue, H.; Nakamura, H.; Elbaum, D.; Alkon, D. L.; Yoshioka, T., *Biophysical Journal* **1998,** *74* (1), 82-89.
128. Blanca, d. R.; Erving, X.; Ueslen, R.; Daniel, J., *Adv. Opt. Mater.* **2017,** *5* (1), 1600508.
129. Jaque, D.; Vetrone, F., *Nanoscale* **2012,** *4* (15), 4301-26.
130. Ruiz, D.; del Rosal, B.; Acebrón, M.; Palencia, C.; Sun, C.; Cabanillas-González, J.; López-Haro, M.; Hungría, A. B.; Jaque, D.; Juarez, B. H., *Adv. Funct. Mater.* **2017,** *27* (6).
131. Liu, H.; Fan, Y.; Wang, J.; Song, Z.; Shi, H.; Han, R.; Sha, Y.; Jiang, Y., *Sci Rep* **2015,** *5*, 14879.
132. Vetrone, F.; Naccache, R.; Zamarrón, A.; Juarranz de la Fuente, A.; Sanz-Rodríguez, F.; Martinez Maestro, L.; Martín Rodriguez, E.; Jaque, D.; García Solé, J.; Capobianco, J. A., *ACS Nano* **2010,** *4* (6), 3254-3258.

133. Kolesnikov, I. E.; Golyeva, E. V.; Kurochkin, M. A.; Lähderanta, E.; Mikhailov, M. D., *Sens. Actuators, B* **2016,** *235*, 287-293.
134. Brites, C. D. S.; Lima, P. P.; Silva, N. J. O.; Millan, A.; Amaral, V. S.; Palacio, F.; Carlos, L. D., *Nanoscale* **2012,** *4* (16), 4799-4829.
135. Brites, C. D. S.; Lima, P. P.; Silva, N. J. O.; Millan, A.; Amaral, V. S.; Palacio, F.; Carlos, L. D., *New J. Chem.* **2011,** *35* (6), 1177-1183.
136. Balabhadra, S.; Debasu, M. L.; Brites, C. D. S.; Ferreira, R. A. S.; Carlos, L. D., *J. Phys. Chem. C* **2017,** *121* (25), 13962-13968.
137. Okabe, K.; Inada, N.; Gota, C.; Harada, Y.; Funatsu, T.; Uchiyama, S., *Nat Commun* **2012,** *3*, 705.
138. Kalytchuk, S.; Poláková, K.; Wang, Y.; Froning, J. P.; Cepe, K.; Rogach, A. L.; Zbořil, R., *ACS Nano* **2017,** *11* (2), 1432-1442.
139. Carattino, A.; Caldarola, M.; Orrit, M., *Nano Lett.* **2018,** *18* (2), 874-880.
140. Cadiau, A.; Brites, C. D. S.; Costa, P. M. F. J.; Ferreira, R. A. S.; Rocha, J.; Carlos, L. D., *ACS Nano* **2013,** *7* (8), 7213-7218.
141. Ng, E. Y. K., *International Journal of Thermal Sciences* **2009,** *48* (5), 849-859.
142. Abadeer, N. S.; Murphy, C. J., *J. Phys. Chem. C* **2016,** *120* (9), 4691-4716.
143. Thiesen, B.; Jordan, A., *Int. J. Hyperthermia* **2008,** *24* (6), 467-74.
144. Jonathan, F.; Yu-Chie, C., *Curr. Pharm. Design* **2013,** *19* (37), 6622-6634.
145. Nguyen, V.; Yan, L.; Xu, H.; Yue, M., *Appl. Surf. Sci.* **2018,** *427*, 1118-1123.
146. Yang, Y.; Kong, W.; Li, H.; Liu, J.; Yang, M.; Huang, H.; Liu, Y.; Wang, Z.; Wang, Z.; Sham, T.-K.; Zhong, J.; Wang, C.; Liu, Z.; Lee, S.-T.; Kang, Z., *ACS Appl. Mater. Interfaces* **2015,** *7* (49), 27324-27330.
147. Bhaisare, M. L.; Talib, A.; Khan, M. S.; Pandey, S.; Wu, H.-F., *Microchim. Acta* **2015,** *182* (13-14), 2173-2181.
148. Wang, Y.; Hu, A., *J. Mater. Chem. C* **2014,** *2* (34), 6921-6939.
149. Lu, W.; Gong, X.; Yang, Z.; Zhang, Y.; Hu, Q.; Shuang, S.; Dong, C.; Choi, M. M. F., *RSC Adv.* **2015,** *5* (22), 16972-16979.
150. Yang, C.; Zhu, S.; Li, Z.; Li, Z.; Chen, C.; Sun, L.; Tang, W.; Liu, R.; Sun, Y.; Yu, M., *Chem Commun (Camb)* **2016,** *52* (80), 11912-11914.
151. Liu, X.; Tang, X.; Hou, Y.; Wu, Q.; Zhang, G., *RSC Adv.* **2015,** *5* (99), 81713-81722.
152. Jiang, K.; Wu, J.; Wu, Q.; Wang, X.; Wang, C.; Li, Y., *Part. Part. Syst. Charact.* **2017,** *34* (2).
153. Wang, C.; Jiang, K.; Wu, Q.; Wu, J.; Zhang, C., *Chem.: Eur. J.* **2016,** *22* (41), 14475-14479.
154. Wang, C.; Lin, H.; Xu, Z.; Huang, Y.; Humphrey, M. G.; Zhang, C., *ACS Appl. Mater. Interfaces* **2016,** *8* (10), 6621-8.
155. Zhou, W.; Zhuang, J.; Li, W.; Hu, C.; Lei, B.; Liu, Y., *J. Mater. Chem. C* **2017,** *5* (32), 8014-8021.
156. Mohan, R.; Drbohlavova, J.; Hubalek, J., *Chemical Physics Letters* **2018,** *692*, 196-201.
157. Chen, D.; Gao, H.; Chen, X.; Fang, G.; Yuan, S.; Yuan, Y., *ACS Photonics* **2017,** *4* (9), 2352-2358.
158. Tang, L.; Ji, R.; Cao, X.; Lin, J.; Jiang, H.; Li, X.; Teng, K. S.; Luk, C. M.; Zeng, S.; Hao, J.; Lau, S. P., *ACS Nano* **2012,** *6* (6), 5102-5110.
159. König, K., *J. Microsc.* **2000,** *200* (2), 83-104.
160. König, K.; Schneckenburger, H., *J. Fluoresc.* **1994,** *4* (1), 17-40.

161. Jaque, D.; Rosal, B. d.; Rodríguez, E. M.; Maestro, L. M.; Haro-González, P.; Solé, J. G., *Nanomedicine* **2014,** *9* (7), 1047-1062.
162. McLaurin, E. J.; Vlaskin, V. A.; Gamelin, D. R., *J. Am. Chem. Soc.* **2011,** *133* (38), 14978-80.
163. Albers, A. E.; Chan, E. M.; McBride, P. M.; Ajo-Franklin, C. M.; Cohen, B. E.; Helms, B. A., *J. Am. Chem. Soc.* **2012,** *134* (23), 9565-8.
164. Yuanjing, C.; Ruijing, S.; Jiancan, Y.; Min, L.; Ziqi, W.; Chuande, W.; Yu, Y.; Zhiyu, W.; Banglin, C.; Guodong, Q., *Adv. Mater.* **2015,** *27* (8), 1420-1425.
165. Llopis, J.; McCaffery, J. M.; Miyawaki, A.; Farquhar, M. G.; Tsien, R. Y., *Proceedings of the National Academy of Sciences of the United States of America* **1998,** *95* (12), 6803-6808.
166. Roduner, E., *Chem. Soc. Rev.* **2006,** *35* (7), 583-592.
167. Koltsov, D. a. K., I., Application of Nanomaterials to Industry: How are Nanomaterials Used and What Drives Future Applications? In *Metrology and Standardization of Nanotechnology*.
168. Bera, D.; Qian, L.; Tseng, T.-K.; Holloway, P. H., *Mater.* **2010,** *3* (4), 2260-2345.
169. Peng, H.; Li, Y.; Jiang, C.; Luo, C.; Qi, R.; Huang, R.; Duan, C.-G.; Travas-Sejdic, J., *Carbon* **2016,** *100*, 386-394.
170. Xiao, L.; Sun, H., *Nanoscale Horiz.* **2018,** *3* (6), 565-597.
171. Wang, Y.; Zhu, Y.; Yu, S.; Jiang, C., *RSC Adv.* **2017,** *7* (65), 40973-40989.
172. Wang, J.; Zhang, P.; Huang, C.; Liu, G.; Leung, K. C.-F.; Wáng, Y. X. J., *Langmuir* **2015,** *31* (29), 8063-8073.
173. Liu, W.; Li, C.; Ren, Y.; Sun, X.; Pan, W.; Li, Y.; Wang, J.; Wang, W., *J. Mater. Chem. B* **2016,** *4* (35), 5772-5788.
174. Ding, H.; Yu, S. B.; Wei, J. S.; Xiong, H. M., *ACS Nano* **2016,** *10* (1), 484-91.
175. Song, P.; Zhang, L.; Long, H.; Meng, M.; Liu, T.; Yin, Y.; Xi, R., *RSC Adv.* **2017,** *7* (46), 28637-28646.
176. Wang, L.; Li, M.; Li, W.; Han, Y.; Liu, Y.; Li, Z.; Zhang, B.; Pan, D., *ACS Sustainable Chem. Eng.* **2018,** *6* (10), 12668-12674.
177. Gao, X.; Du, C.; Zhuang, Z.; Chen, W., *J. Mater. Chem. C* **2016,** *4* (29), 6927-6945.
178. Wang, H.; Zhang, P.; Tian, Y.; Zhang, Y.; Yang, H.; Chen, S.; Zeng, R.; Long, Y.; Chen, J., *Analytical and Bioanalytical Chemistry* **2018,** *410* (18), 4379-4386.
179. Chen, J.; Li, Y.; Lv, K.; Zhong, W.; Wang, H.; Wu, Z.; Yi, P.; Jiang, J., *Sens. Actuators, B* **2016,** *224*, 298-306.
180. Wang, Y.; Lu, L.; Peng, H.; Xu, J.; Wang, F.; Qi, R.; Xu, Z.; Zhang, W., *Chem. Commun.* **2016,** *52* (59), 9247-9250.
181. Yu, T.; Wang, H.; Guo, C.; Zhai, Y.; Yang, J.; Yuan, J., *R Soc Open Sci* **2018,** *5* (7), 180245.
182. Sharma, V.; Kaur, N.; Tiwari, P.; Mobin, S. M., *J Photochem Photobiol B* **2018,** *182*, 137-145.
183. Shi, W.; Li, X.; Ma, H., *Methods and Applications in Fluorescence* **2014,** *2* (4), 042001.
184. Tian, Y.; Su, F.; Weber, W.; Nandakumar, V.; Shumway, B. R.; Jin, Y.; Zhou, X.; Holl, M. R.; Johnson, R. H.; Meldrum, D. R., *Biomater.* **2010,** *31* (29), 7411-7422.
185. Chandra, A.; Singh, N., *ACS Biomater. Sci. Eng.* **2017,** *3* (12), 3620-3627.
186. Niu, W.; Fan, L.; Nan, M.; Li, Z.; Lu, D.; Wong, M. S.; Shuang, S.; Dong, C., *Anal. Chem.* **2015,** *87* (5), 2788-2793.
187. Du, F.; Ming, Y.; Zeng, F.; Yu, C.; Wu, S., *Nanotechnol.* **2013,** *24* (36), 365101.
188. Liu, W.; Li, C.; Sun, X.; Pan, W.; Wang, J., *Sens. Actuators, B* **2017,** *244*, 441-449.

189. Weissleder, R.; Pittet, M. J., *Nat.* **2008,** *452*, 580.
190. Shao, A.; Xie, Y.; Zhu, S.; Guo, Z.; Zhu, S.; Guo, J.; Shi, P.; James, T. D.; Tian, H.; Zhu, W.-H., *Angew. Chem., Int. Ed.* **2015,** *54* (25), 7275-7280.
191. Li, L.-L.; Li, K.; Liu, Y.-H.; Xu, H.-R.; Yu, X.-Q., *Sci. Rep.* **2016,** *6*, 31217.
192. Zhang, I.; Beus, M.; Stochaj, U.; Le, P. U.; Zorc, B.; Rajić, Z.; Petrecca, K.; Maysinger, D., *Cell Death Discovery* **2018,** *4* (1), 41.
193. Yoshimori, T.; Yamamoto, A.; Moriyama, Y.; Futai, M.; Tashiro, Y., *Journal of Biological Chemistry* **1991,** *266* (26), 17707-17712.
194. Lawrence, R. E.; Zoncu, R., *Nature Cell Biology* **2019,** *21* (2), 133-142.
195. Stransky, L. A.; Forgac, M., *Journal of Biological Chemistry* **2015,** *290* (45), 27360-27369.
196. Kim, H. G.; Hien, T. T.; Han, E. H.; Hwang, Y. P.; Choi, J. H.; Kang, K. W.; Kwon, K.-i.; Kim, B.-H.; Kim, S. K.; Song, G. Y.; Jeong, T. C.; Jeong, H. G., *British Journal of Pharmacology* **2011,** *162* (5), 1096-1108.
197. Pernicova, I.; Korbonits, M., *Nat. Rev. Endocrinol.* **2014,** *10*, 143.
198. Segal, E. D.; Yasmeen, A.; Beauchamp, M.-C.; Rosenblatt, J.; Pollak, M.; Gotlieb, W. H., *Biochem. Biophys. Res. Comm.* **2011,** *414* (4), 694-699.
199. Kazmi, F.; Hensley, T.; Pope, C.; Funk, R. S.; Loewen, G. J.; Buckley, D. B.; Parkinson, A., *Drug Metabolism and Disposition* **2013,** *41* (4), 897-905.
200. Gao, A.; Kang, Y.-F.; Yin, X.-B., *New J. Chem.* **2017,** *41* (9), 3422-3431.